Synthesis and Characterisation of Gold-Based Compounds as Potential DNA Intercalators

Submitted in fulfilment of the requirement for the degree of

Master of Science

By

Desigan Moodley

BSc, (Hons.) (UKZN)

November 2016

UNIVERSITY OF KWAZULU-NATAL

School of Chemistry and Physics,
University of KwaZulu-Natal
Pietermaritzburg

Declaration

I, Desigan Moodley, declare that:

(i) The research reported in this thesis/dissertation, except where otherwise indicated, is my original research.

(ii) This thesis/dissertation has not been submitted for any degree or examination at any other university.

(iii) This thesis/dissertation does not contain other persons' data, pictures, graphs or other information, unless specifically acknowledged as being sourced from other persons.

(iv) This thesis/dissertation does not contain other persons' writing, unless specifically acknowledged as being sourced from other researchers. Where other written sources have been quoted, then:

a) Their words have been re-written but the general information attributed to them has been referenced;

b) Where their exact words have been used, their writing has been placed inside quotation marks, and referenced.

(v) Where I have reproduced a publication of which I am author, co-author or editor, I have indicated in detail which part of the publication was actually written by myself alone and have fully referenced such publications.

(vi) This dissertation/thesis does not contain text, graphics or tables copied and pasted from the internet, unless specifically acknowledged, and the source being detailed in the dissertation/thesis and in the References sections.

Signed: _____ Date: _____

Desigan Moodley

I hereby certify that this statement is correct to the best of my knowledge:

Signed: _____ Date: _____

Dr. Matthew P. Akerman (Supervisor)

Acknowledgments

Firstly, I would like to thank Dr. M. Akerman and Prof. O.Q. Munro for all the support, patience and motivation they have provided during the course of this project. Their advice has been essential towards the success of this project. I would especially like to thank Dr. M. Akerman for the time taken from his busy days to mentor me.

I would like to thank my girlfriend for her constant support, motivation and inspiration not just for this project but in everything I do. I will always be grateful to you.

I wish to thank my family and friends for their support and encouragement.

Lastly, I am thankful to N.R.F for the financial support.

Research Outputs

The results from this project have been presented as an oral present ation and poster presentation at the following conferences or colloquia.

Title: Gold(III) DNA Intercalators: Targeted Chemotherapeutic Agents.

1. SACI Honours chemistry colloquium 2013.
2. UKZN Research Day 2015.
3. Indaba 8 chemistry conference 2015.

List of abbreviations

%Diff.	**percentage difference**
Å	angstrom
°	degrees
A	absorbance
a	lattice constant
aq	aqueous
BC	before Christ
br	broad
Calc.	calculated
COSY	correlation spectroscopy
d	doublet
dd	doublet of doublets
DNA	deoxyribonucleic acid
FTIR	fourier transform infra-red
gDNA	genomic deoxyribonucleic acid
g	gram/ gas
GIAO	Gauge-Including Atomic Orbitals
HOMO	highest occupied molecular orbital
HSQC	heteronuclear single-quantum correlation spectroscopy
IC_{50}	inhibitory concentration 50%
IR	infra-red
J	coupling constant
LUMO	lowest unoccupied molecular orbital
m	multiplet/ medium intensity
MHz	megahertz
m/z	mass to charge ratio
NMR	nuclear magnetic resonance
ppm	parts per million
s	singlet/ strong
t	triplet
TD-DFT	time-dependent density functional theory
UV	ultraviolet
U.S.A	United States of America
vis	visible

List of figures and schemes

Chapter 2

Chapter 5

List of tables

Abstract

Five novel bis(imidazole-imine) gold(III) chelates were synthesized and characterized by NMR (^{1}H, ^{13}C, COSY, HSQC, ^{19}F and ^{31}P), FTIR and UV/visible spectroscopy as well as high resolution mass spectrometry and in some cases X-ray crystallography. The ligands comprised methyl imidazole moieties bridged by a synthetically variable di(azomethine) linkage. Five of the ten synthesised ligands were successfully chelated to gold(III), these ligands contained propyl, 2,2-dimethyl, 2-hydroxy, 2-methoxy-propyl and 2-ethoxy-propyl linkages. The ligands were synthesised by the condensation of two equivalents of 4-methyl-5-imidazolecarbaldehyde and the respective diamines. The chelate synthesis was achieved with direct metalation using $[Bu_4N][AuCl_4]$.

Solid state structures were determined by single crystal X-Ray crystallography for two ligands and three gold(III) chelates. The ligands were found to form stable hydrogen-bonded networks with the water molecule. The water molecules are found in the centre of hydrogen-bonded columns forming hydrogen bonds with the surrounding ligand molecules. The anti-configuration of the ligands is required for formation of the polymers. The hydrogen-bonded columns are co-linear with the *c*-axis. The three-dimensional structure is a result of a cross-linking the columns through additional hydrogen bonds. The gold(III) chelates all had a square planar coordination geometry. This is the regular geometry of d^8 metal ion chelates. Metal ion chelation occurs with concomitant deprotonation of the imidazole NH groups; this is in contrast to previously reported metal chelates of the related ligands. The deprotonation of the imidazole NH yields a dianionic tetradentate *N*-donor ligand. The average Au-N_{imine} bond measures 2.007 Å and the average Au-$N_{imidazole}$ bond measures 1.993 Å. The coordination geometry differed slightly from the ideal square planar geometry with an acute bond angle of 80.73˚ (N_{imine}-Au-$N_{imidazole}$). This bond angle is constrained by the bite angle of the ligands and resulting 5-membered chelation ring. Au···π and π···π interactions were present in the chelates, stabilising various supramolecular structures.

The chelates were designed to exploit the square planar nature of the gold(III) ion to produce metal aromatic metal chelates suitable for DNA intercalation to control the proliferation of tumour cells. Both direct DNA binding titrations and competitive DNA binding studies did not show any significant affinity towards DNA. The likely reason for

this is that the methyl groups on the imidazole rings, which are required to stabilise the metal ion through their inductive effect, prevent the intercalation process. This class of compounds therefore needs further development to achieve the final goal of chemotherapeutic agent.

Density Functional Theory (DFT) was used to simulate various properties of the ligands and gold(III) chelates. The DFT calculated data was compared to the experimental data to determine the efficiency of the chosen basis set and hybrid functional used. DFT was also used to deconvolute the experimental data obtained, with particular emphasis on the electronic spectra. The level of theory used for ligands was B3LYP/6-311G and for the gold(III) chelates PBE1PBE/LanL2DZ. DFT was used to calculate the optimized geometry, NMR and electronic spectra. The vibrational frequencies for both ligands and chelates showed no negative Eigen values which implies that the optimized geometry is indeed the true minimum on the global potential energy surface.

Table of Contents

Chapter 1| Introduction

1.1 Preface

Cancer has been well documented in animals and humans alike throughout history. The earliest evidence of cancer comes from ancient Egypt where bone cancer was discovered in mummified human remains [1]. Cancer has now been dated to 3000 B.C., yet this disease from biblical times still greatly affects the modern population. In fact, it is the second leading cause of death in the United States of America.

Cancer is a group of diseases defined as the uncontrollable and rapid growth of cells in the body. There are many forms of cancer such as bladder, breast and prostate cancers. Statistics obtained from the National Cancer Institute (NCI, U.S.A.) clearly show a decrease in the number of deaths from 1975 until 2010. It can safely be assumed that the decrease in mortality is due to the advancement in anti-cancer drugs and chemotherapy. Statistics for the African continent still show a high mortality rate. This is due to lack of early detection and limited access to treatment [2]. Although statistics based on the U.S.A. population show a decrease in mortality rates, there is still a need to continue research into new anti-cancer agents as there are problems associated with current treatments. These include unpleasant side-effects and drug resistance in secondary tumours [3].

It is hypothesised that by including metal ions in the anti-cancer agents it will potentially alter their mechanism of action and helps overcome the current issues associated with chemotherapy. Cisplatin was the first anti-cancer drug to be used that had a metal centre. Although it shows good efficacy, it has several harmful side-effects and tumours can become resistant to the drug. These drawbacks have prompted the search for alternative metal-based anti-cancer drugs [4].

The medicinal properties of gold were first discovered in the 1890s when it was found that $K[Au(CN)_2]$ could kill the bacteria responsible for tuberculosis. It was later found that gold(I) thiolate complexes could be used in the treatment of rheumatoid arthritis. Gold(III) complexes have until recently not been as intensely studied as those of gold(I) because gold(III) complexes are highly reactive, have a high redox potential and poor stability. These properties meant that gold(III) would be reduced to gold(I) or metallic gold under physiological conditions. Recently, more stable gold(III) complexes have been synthesised using strong sigma-donor ligands to stabilise the gold(III) ion. Gold(III) is isoelectronic with platinum(II) i.e. they have a d^8

configuration which leads to a square-planar geometry and is therefore an ideal scaffold around which ligands with DNA recognition elements can be assembled. These factors have allowed the applications of gold(III) to expand into medicinal chemistry [4][5].

The aim of this project is to synthesise novel bis(imidazole-imine) gold(III) anti-cancer agents that will intercalate DNA thus preventing DNA replication and tumour cell growth. The complexes have been designed to include a planar aromatic region, a hydrogen bonding region and carry a positive charge. They are therefore anticipated to be effective DNA intercalators and chemotherapeutic agents.

1.2 Causes of cancer

Cancer does not have one main cause, but is rather caused by a combination of several factors. These can include diet, pollution, alcohol, viral infections, geophysical factors, occupational factors, tobacco and genetic factors. These external stimuli lead to a change in the arrangement of genes, therefore causing a mutation to occur. Cancer cells arise when critical genes are mutated; these mutations lead to the unregulated proliferation of cells forming tumours [6][7].

There are many forms of cancer and these grow and divide at different rates. The most common form of cancer among men is prostate cancer, the most common form of cancer among women is breast cancer and the most common form of preventable cancer in both sexes is lung cancer [3].

There are many mutations that could lead to cancer, but the most common are defective START checkpoint (*vida infra),* apoptosis malfunction and oncogenes. The cell cycle has three periods: cell growth, DNA synthesis and cell division. The length of each period is controlled by chemical signals. If the signals malfunction the cell can become cancerous. There are four phases in the cell cycle: G1, synthesis, G2 and mitosis. Translation into each phase is regulated by checkpoints. Each checkpoint halts the progression through the cycle until important processes such as DNA replication are complete or damaged cells are repaired. Two proteins are important to the functioning of these checkpoints i.e. cyclin and cyclindependantkinases (CDK). CDK regulates the activity of other proteins and cyclin enables CDK to function. One of the most important checkpoints is the START checkpoint which is found in mid G1. The START checkpoint determines if it is appropriate to move from the G1 phase to the synthesis phase. If the cell is driven past the START checkpoint it is committed to another round of DNA replication. In tumour cells, checkpoints are deregulated due to defects in genes that control the abundance of cyclin and CDK. In normal cells if DNA is damaged the cell pauses before DNA replication to

repair the DNA, but if the START checkpoint is damaged the cell doesn't pause for damaged DNA and the damaged DNA is replicated. These cells are highly prone to becoming cancerous [9].

Damaged cells can be terminated through apoptosis; controlled cell death. If the apoptosis pathway is inhibited abnormal cells can replicate, potentially leading to tumours. Proteolytic enzymes called caspases play an import role in apoptosis. These enzymes attack proteins and cleave them which results in cells losing their integrity, their chromatin becomes fragmented and blebs of cytoplasm form at their surfaces and the cell shrinks. The cell is then engulfed by phagocytes. If the apoptosis mechanism is damaged or inactive, a cell that would be terminated because of a compromise in genetic integrity will continue to live and replicate and this can lead to a tumour [9].

Researchers have identified two classes of genes which when mutated can contribute to the development of cancer. The first class is called oncogenes; these genes have been altered such that they are constantly active promoting uncontrolled cell division. The second class is tumour suppressor genes, when these falter cell division can no longer be suppressed leading to a tumour [6].

1.3 Treatment of cancer

There are a range of treatment options available for cancer patients, but the three major forms of treatment are radiation, surgery and chemotherapy.

Radiation therapy is a treatment that uses high energy particles such as X-rays to destroy cancer cells. There are three methods for radiation therapy: external, internal and systematic radiation. External radiation uses equipment that focuses high energy particles from outside of the patient's body into the tumour. Internal radiation uses a radiation source that is placed near the tumour. Since the radiation source is close to the tumour fewer cells are damaged when compared to external radiation methods. The radiation source can be placed in a body cavity, near the tumour. Systematic radiation uses radioactive drugs to treat the tumour. These drugs bind to antibodies that attach to the cancer cells and then radiate the tumour cells [10].

Surgery as a cancer treatment is referred to as curative surgery and refers to the surgical removal of a tumour. There are several curative surgery types, for example preventive surgery which is the removal of benign tissue that is likely to become cancerous and staging surgery to determine how much cancer is present and how much has spread [11].

Chemotherapy involves using a drug to treat a disease; recently it has been associated with the drug treatment of cancer. In chemotherapy, drugs are given to a patient in an effort to slow or

stop tumour cell growth. The first anti-cancer drug was discovered surreptitiously. Mustard gas was first used as a chemical weapon in World War I and was further studied in World War II. In World War II when a group of people were accidentally exposed to this chemical weapon, it was discovered that their white blood cell count was very low. It was theorized that if it could affect the production of white blood cells it could have a similar effect on cancer cells. In the early 1940's several patients diagnosed with advanced lymphomas, which is cancer of the white blood cells, were treated by intravenous administration of a solution of 1,1-thiobis(2-chloroethane) (commonly referred to as mustard gas). The treatment proved effective in terms of reducing tumour cell growth, but the success was only partial due to the high toxicity of the compound [8].

Other treatments such as surgery and radiation act only on localised parts of the body targeted, for example the lung, whereas chemotherapy can be used to as a local (treat a targeted area) or systematic treatment (travels through the body treating cancer cells wherever they are found). One of the major advantages of chemotherapy is that it can be used as a treatment for remote areas such as the brain where other treatment methods may not be possible. Chemotherapy can also be administrated with other treatments, for example: neoadjuvant chemotherapy, where chemotherapy is administrated before surgery [13].

Chemotherapeutic drugs administered fall into two main categories: cytotoxic and cytostatic [14].

1.3.1 Cytotoxic chemotherapeutic agents

Cytotoxic drugs work by interfering with DNA replication [14]. Under the cytotoxic category there are three main groups:

Antimetabolites: Molecules that appear to be nucleotides and are therefore integrated into the DNA molecule. Once part of the molecule it prevents DNA replication resulting in non-functional DNA [12]. Shown below in Figure 1.3.1 is Xeloda, an example of a cytotoxic chemotherapeutic agent.

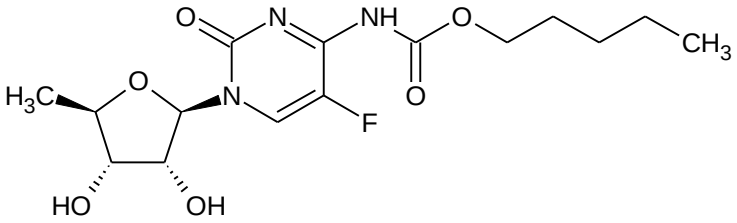

Figure 1.3.1: Capecitabine (Xeloda), an antimetabolite chemotherapeutic agent.

Alkylating agents: Compounds that attach to DNA molecules and distort the shape of the DNA molecule preventing replication. The downside to this group is that it also binds to other molecules in the cell [12]. Shown below in Figure 1.3.2 is Cyclophosphamide, an example of an alkylating agent.

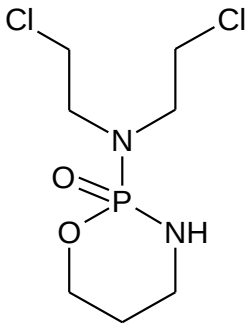

Figure 1.3.2: Cyclophosphamide, an example of an alkylating agent.

DNA binders: This group of drugs attach to DNA, break the DNA, detach and move to the next DNA molecule. Once the drug has bonded to the DNA molecule it blocks transcription or prevents enzymes such as topoisomerase from working. They usually work by inhibiting an enzyme [13]. An example of this class of chemotherapeutics is 9-aminoacridine which is shown in Figure 1.3.3.

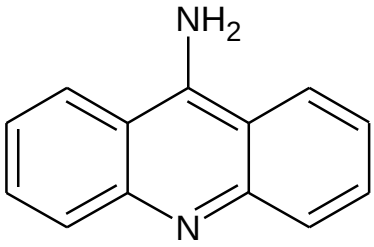

Figure 1.3.3: Schematic structure of 9-aminoacridine, an example of a DNA binder.

These drugs are not cell specific, but target any rapidly dividing cell such as bone marrow and hair follicles. This is the reason for the side-effects of this treatment.

1.3.2 Cytostatic chemotherapeutic agents

Cytostatic drugs target altered biochemical pathways which enable the cancer cells to reproduce at a fast rate. Cytostatic drugs are designed to deactivate the altered enzymes and not to kill the cell, but instead just to prevent cell reproduction [14]. Shown below in Figure 1.3.4 is topotecan which is an example of commercially available cytostatic drug.

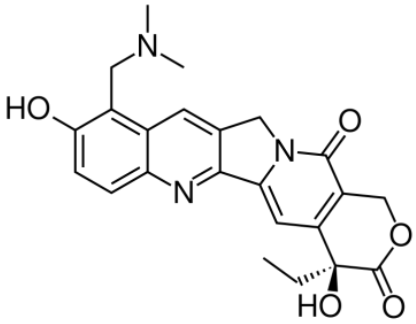

Figure 1.3.4: Structure of topotecan an example of a cytostatic drug.

1.4 DNA Intercalating agents

The novel gold(III) chelates proposed in this work are planar with an extended aromatic region. They are therefore anticipated to act as DNA intercalators [12][13].

DNA is a tightly wound molecule which has a negatively charged phosphate backbone. It requires a cationic species for stability. This is provided by histone proteins, but it can also be stabilised by metal salts and other small organic molecules [15].

Lerman first proposed this DNA binding mode to explain the strong affinity of certain heterocyclic dyes for DNA. When DNA is intercalated by a small molecule, it is stiffened, stabilised, lengthened and partially unwound. Different intercalators cause the DNA to unwind to different degrees. Since the structure of the intercalated DNA has been altered, it leads to functional change such as inhibition of replication [16].

Drug/DNA interactions can be classified into two major groups: intercalators and groove binders. Intercalation involves the insertion of a planar molecule between DNA base pairs, which results in a decrease in DNA helical twist and increasing the length of the DNA strand. Figure 1.4.1 illustrates the three modes of binding for inorganic compounds with DNA [17].

(a) (b) (c)

Figure 1.4.1: The three modes of binding for inorganic compounds with DNA. (a) Groove binding. (b) Intercalation. (c) Insertion [17].

1.4.1 Organic DNA Intercalators

Organic DNA intercalators are typically polyaromatic compounds. These compounds are able to intercalate DNA and inhibit nucleic acid synthesis *in vivo*. Organic anti-cancer drugs can interact with DNA in a number of ways such as minor groove binding, major groove binding, intercalation between base pairs and threading intercalation. Molecules without any bulky functional groups can intercalate without binding to the minor or major groove. Intercalators that bind almost entirely with their aromatic region inserted between the guanine-phosphate-guanine bases are refered to as classic intercalators [18]. An example of a classic intercalator is proflavine as shown in Figure 1.4.2.

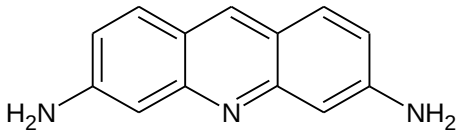

Figure 1.4.2: Structure of Proflavine, a classic intercalator. The fused aromatic ring structure is ubiquitous in DNA intercalators.

1.4.2 Inorganic DNA Intercalators

DNA intercalators are characterized by the presence of an extended electron-deficient planar aromatic ring system. When DNA intercalators bind they extend and unwind the negatively charged phosphate backbone. The DNA/drug conjugate is stabilised by π-π stacking interactions with the planar aromatic region [19].

A metallo-intercalator is a metal complex with one or more intercalating ligands. These intercalators orientate themselves parallel to base pairs and unwind the DNA strands. The aromatic region of the complex intercalates the DNA strand while the metal centre protrudes out of the DNA helix. The intercalated ligand anchors the metal centre with respect to the DNA strand. These complexes are rigid and have well-defined symmetry. Selective recognition of a DNA sequence by a metallo-intercalator can be achieved by matching the functionality of the ligands positioned in the major groove with that of the target base pairs [17].

Intercalation by the ligands of metal chelates was first illustrated using photophysical methods, but by using more extensive techniques like NMR and high resolution crystal structure, the

complex binding modes are now well understood. It is found that the intercalating molecule enters the DNA double strand *via* the major groove and then acts as a new base pair. During this process no existing base pair is ejected. This intercalation results in the widening of the major groove and binding site but overall distortion is minimal [15].

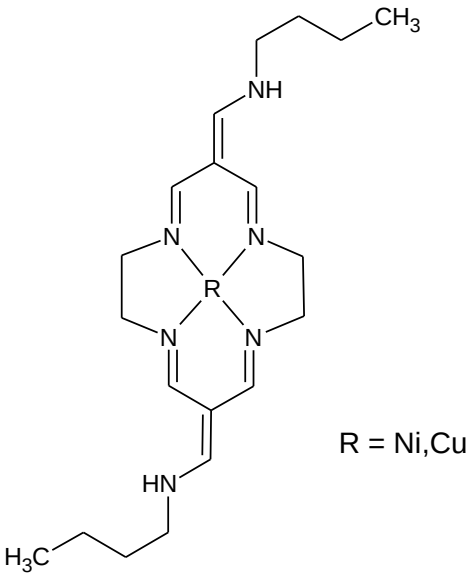

Figure 1.4.3: Structure of tetraaza[14]macrocyclic complexes, an example of a metallo-intercalator [34].

1.5 Cisplatin

Cisplatin (structure shown in Figure 1.5.1) is one of the most widely used chemotherapeutic agents. Cisplatin was synthesised in 1945, but its anti-cancer properties were only discovered in the mid 1960's. Since then cisplatin has been extensively used in the fight against cancer. It is most effective in the treatment of testicular and ovarian cancer, though it is widely used for treating other forms of cancer such as bladder, cervical, head and neck cancers [22]. Although effective, cisplatin does have disadvantages. The first disadvantage is severe side-effects, for example nausea, vomiting, ototoxicity, neurotoxicity, and nephrotoxicity. These major side effects limit the dosage that can be prescribed to patients. A second disadvantage is cisplatin has limited aqueous solubility therefore the drug has to be given intravenously as a suspension. Finally, the drug is only effective against a few types of cancer. Cancer types such as non-small cell lung are resistant to cisplatin while cancers such as ovarian can develop resistance after the first treatment [21].

Cisplatin is a highly relevant molecule for comparison with gold(III) chemotherapeutics as it is one of the metal-based drugs commercially available. The Pt(II) metal centre is also

isoelectronic and shares the same coordination geometry with the gold(III) chelates proposed in this work.

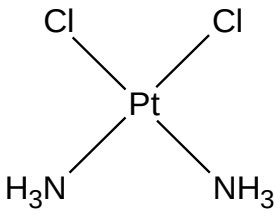

Figure 1.5.1: Structure of cisplatin.

1.5.1 Mechanism of action of cisplatin

Cisplatin works in a two-step process: firstly it enters the cell and binds to non-DNA targets and secondly it binds to the DNA of the cell.

In the non-DNA binding the Pt(II) coordinates to the constituents in the lipid bilayer, which contains nitrogen and sulphur atoms, as it passes through the cell wall. In the cytoplasm many cellular components have soft nucleocytoplasm sites such as proteins. The most important target in the non-DNA aspect of the mechanism is the tripeptide glutathione (GSH). Cisplatin may also alter enzymes, receptors, and proteins *via* sulphur co-ordination [21].

In the DNA binding mechanism the main target for cisplatin is gDNA. The cisplatin attaches to the N7 nitrogen atoms of guanine and adenine in the major groove of the double helix because this is the most accessible and most reactive site for cisplatin. When bound to the DNA it prevents DNA replication from occurring by blocking transcription [21].

Due to the severe side-effects and acquired resistance to cisplatin, derivatives i.e. carboplatin and oxaliplatin (structures shown in Figure 1.5.2) were developed and are available for commercial use. Carboplatin was developed in the 1980's to reduce the side-effects of cisplatin while retaining the anticancer properties [20]. In this analogue, the two chlorides are replaced with a cyclobutanedicarboxylate ligand. Replacing the chlorides does not eliminate the drugs ability to be an anti-cancer agent. Oxaliplatin is a third generation platinum compound and was developed to overcome cisplatin resistance. Oxaliplatin shows good antitumour effects *in vivo* and *in vitro* [22]. The chlorides are replaced by an oxalate ligand and the ammines are replaced with a diaminocyclohexane ring [21].

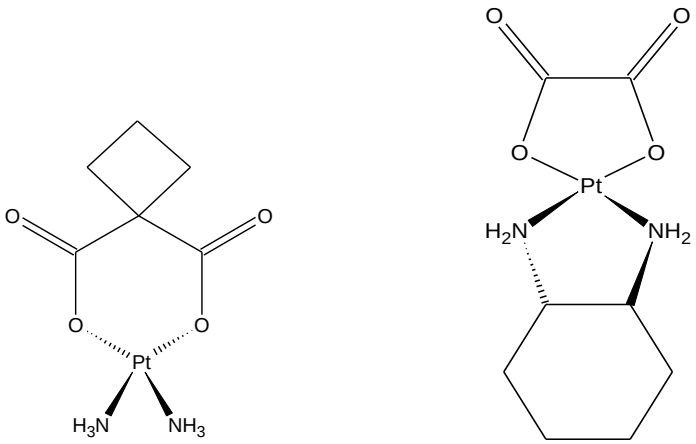

(a) (b)

Figure 1.5.2: Structure of cisplatin derivatives. (a) Carboplatin and (b) Oxaliplatin.

Although cisplatin is not an example of a DNA intercalator, as are the gold(III) chelates in this work, it is an example of how effective the inclusion of metal ions can be in the synthesis of anti-cancer agents.

1.6 DNA topoisomerase I

DNA topoisomerase enzymes manage the topological state of the DNA strand during DNA replication and are a common target for chemotherapeutic agents. There are two classes of the topoisomerase enzyme i.e. topoisomerase I and topoisomerase II. The first class regulates the supercoiled DNA structure and relieves the tension in the DNA strand caused by unwinding and winding during DNA replication. It works by causing a single strand break in the DNA which allows the torque to spin the broken strand before the relaxed strand is religated. The second class passes a region of duplex DNA from the same or a different molecule through a double-stranded break generated in the DNA helix [23]. The structure of *E. coli* topoisomerase is illustrated below in Figure 1.6.1.

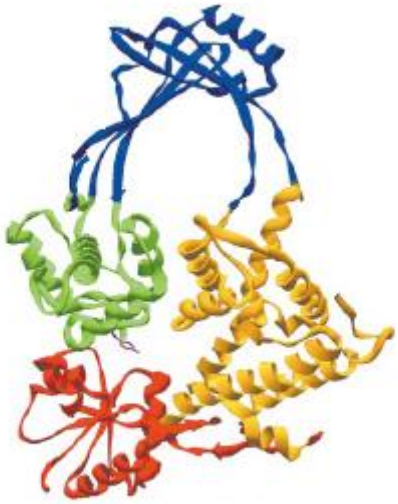

Figure 1.6.1: Structure of *E. coli* topoisomerase [32].

1.7 DNA topoisomerase I inhibitors

DNA topoisomerase is the target for many anticancer drugs. Topoisomerase inhibitors have two categories: catalytic inhibitors and topoisomerase poisons. The topoisomerase poisons are cytotoxic and work by stabilising the covalent complexes between the enzyme and DNA. They interfere with the religation step and leave the DNA strands unligated. Catalytic inhibitors stop the enzyme activity by preventing the enzyme inducing DNA strand breaks. A well known topoisomerase inhibitor is camptothecin [24].

Camptothecin is found in the bark of the Chinese camptotheca tree. It was used in China as a treatment for many illnesses like psoriasis, leukemia, diseases of the liver and stomach and infection of the spleen. In modern medicine, it is used as an anti-cancer agent. The mode of action of camptothecin is that it prevents the topoisomerase I enzyme from producing reversible single-strand breaks in DNA during DNA replication. These strand breaks relieve torsional strain and allow DNA replication to continue. When camptothecin is present it binds to the topoisomerase I enzyme and prevents the topoisomerase I enzyme from functioning and thus the enzyme is released from the DNA strand and DNA replication is stopped [25].

The gold(III) chelates that will be synthesised in this work share many structural features with topotecan and other topoisomerase inhibitors such as an aromatic planar region, a hydrogen bonding region and have a positive charge. Shown in Figure 1.7.1 is a comparison of the

structure of camptothecin and $[Au(L4)]^+$. The red regions are aromatic planar regions and the green atoms indicate potential hydrogen bonding.

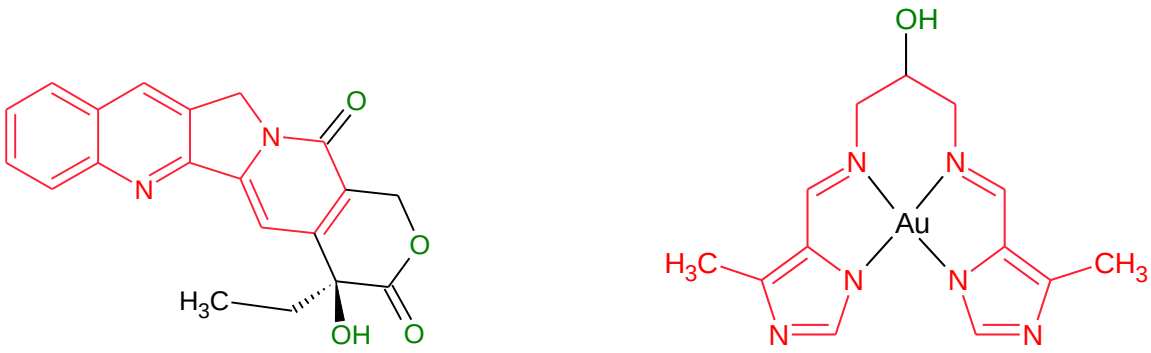

(a) (b)

Figure 1.7.1: Comparison of the structures of (a) Camptothecin, an example of a topoisomerase inhibitor and (b) $[Au(L4)]^+$.

1.8 Gold in medicine

Gold has always been viewed as an extraordinary metal which denotes status, wealth and royalty, so naturally ancient civilizations that had access to gold began to explore the medicinal properties of this precious metal. Ancient civilizations such as China in 2500 B.C. believed that gold could cure or heal people suffering from small pox, ulcers and measles. Japanese traditional healers said gold should be placed in food items and in tea to ensure good health. Gold(I) was used clinically for the first time in the 1920's for its *in vitro* bacteriostatic effect [35].

In recent years gold(I) complexes have been used to treat rheumatoid arthritis, which is an autoimmune inflammatory disease. Rheumatoid arthritis is characterised by the erosion of joints. The first gold compounds used in treatment were aurothioglucose (ATG) and aurothiomalate (ATM). The structures of these two drugs are shown below in Figure 1.8.1. These drugs were given intramuscularly and were cleared quickly from the plasma, but sufficient amounts of the drug were spread throughout the body to allow the compounds to be therapeutic. The highest concentration of the drug is found in the kidney which results in unwanted nephrotoxicity. ATM and ATG have serious side effects which prompted the synthesis of new drugs [26].

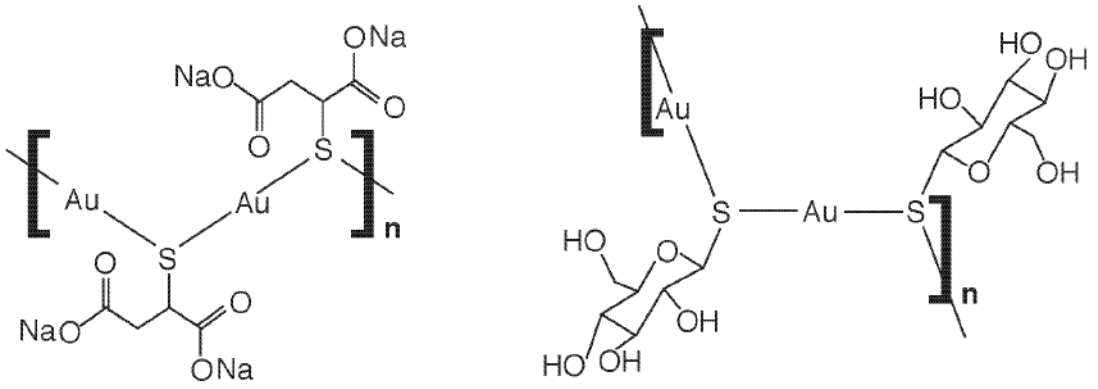

(a) (b)

Figure 1.8.1: Early gold(I)-based drugs for treatment of rheumatoid arthritis. (a) aurothiomalate and (b) aurothioglucose [26].

Gold(III) was not seen as a viable option in the fight against cancer due to its high reactivity, high redox potential and low stability. It has subsequently been determined that the gold(III) ion can be sufficiently stabilised by the use of ligands which donate electron density to the electron deficient gold(III) ion. Some of the ligands used for this purpose are polyamines. Nitrogen donor ligands, particularly anionic N-donor ligands, are very effective for gold(III) ion stabilisation. This breakthrough opened the door for new research. One area the gold(III) ion could be used in is anticancer research. Cisplatin has dominated this field and is the benchmark for future drugs. Both Pt(II) and gold(III) are d^8 metals and both have a square planar geometry. So the circumstantial evidence suggests that gold(III) complexes should mimic the anti-cancer properties of the popular cisplatin [33].

Gold(III) complexes that have been synthesized as anti-cancer drugs contain ligands with nitrogen, oxygen and sulphur donor atoms. There are two species of pyridine complexes $[AuCl_3(Hpm)]$ and $[AuCl_2(pm)]$(structures shown in Figure 1.8.2). Both these complexes show good cytotoxicity against Tlymphoblastoid and human ovarian cell lines. $[Au(phen)Cl_2]Cl$, $[Au(terpy)Cl]Cl_2$, $[AuCl(dien)Cl_2]$ and $[Au(en)_2]Cl_3$ all showed reasonable stability under physiological conditions. The IC_{50} value for $[Au(phen)Cl_2]Cl$ is 7.4 μM and for $[AuCl(dien)Cl_2]$ is 6.0 μM. The Au-azpy bidentate (structure shown in Figure 1.8.2) complex also shows good cytotoxicity against cisplatin-resistant ovarian tumour cells [26].

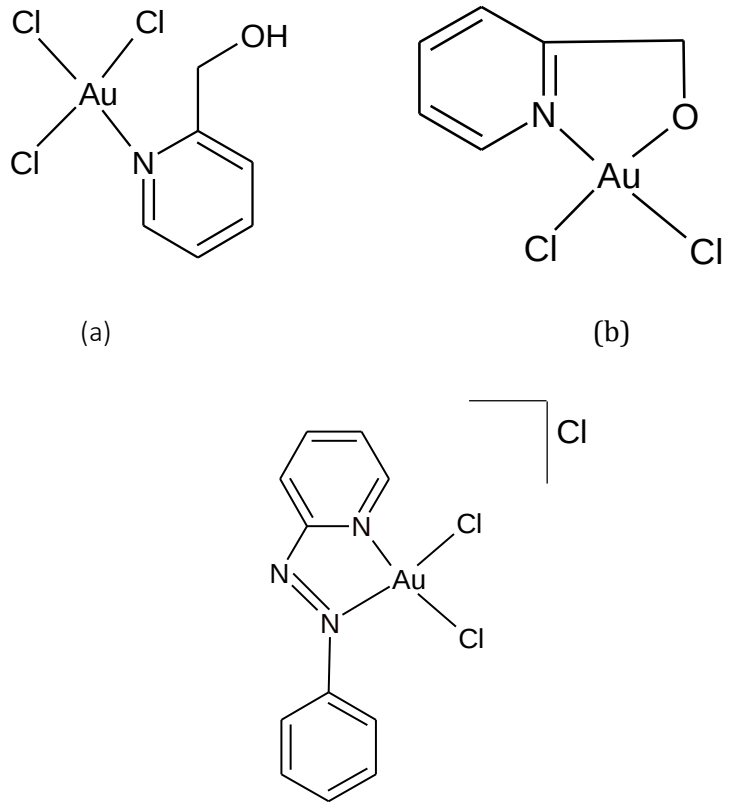

Figure 1.8.2: Structures of (a) ($AuCl_3$(Hpm)), (b) $AuCl_2$(pm) and (c) Au-azpy bidentate.

Gold(III) tetraarylporphyrins, Schiff bases and bis(pyridyl)carboxamidechelates all exhibit anti-cancer properties. The IC_{50} values of the gold(III) porphyrin (general structure shown in Figure 1.9.2.) complexes were found to be in the range of 0.11-0.73 μM. It was also noted that the gold(III) porphyrins complexes were effective against cisplatin resistant cells , having IC_{50} values of 0.17, 0.14 and 0.11 μM against promyelocytic leukemia, nasopharyngeal carcinoma, cervical epithelioid carcinoma, hepatocellular carcinoma and oral epidermoid carcinoma. The gold(III) Schiff base complexes (structure shown in Figure 1.8.4.) and bis(pyridyl)carboxamide (general structure shown in Figure 1.8.5.) compounds displayed IC_{50} values in the range of 10-30 μM. These are comparable to cisplatin which has a mean IC_{50} value of approximately 15 μM [26].

The gold(III) complexes proposed in this study will share three structural similarities with the gold complexes mentioned above. The complexes have a planar aromatic region, a hydrogen bonding region and will have a positive charge. They are therefore anticipated to be effective DNA intercalators and chemotherapeutic agents.

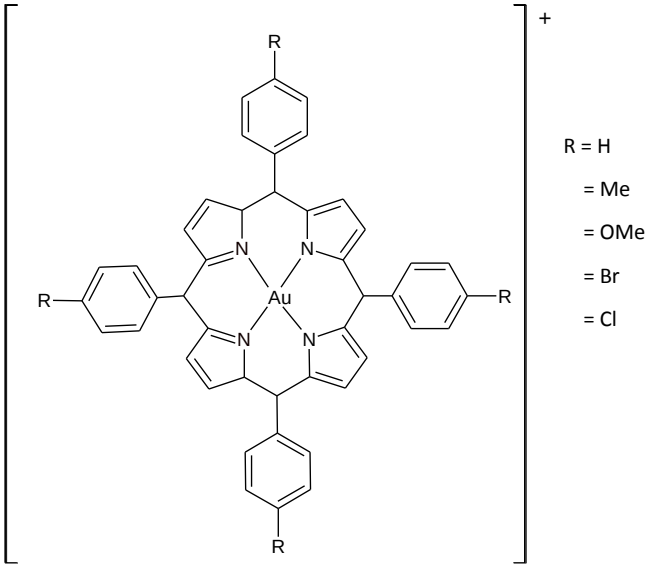

Figure 1.8.3: Structure of gold(III) porphyrins.

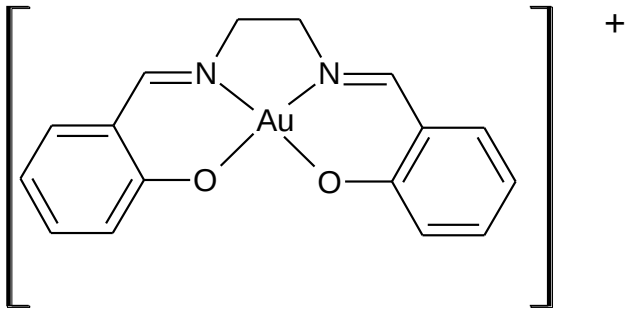

Figure 1.8.4: Structure of gold(III) Schiff base complex.

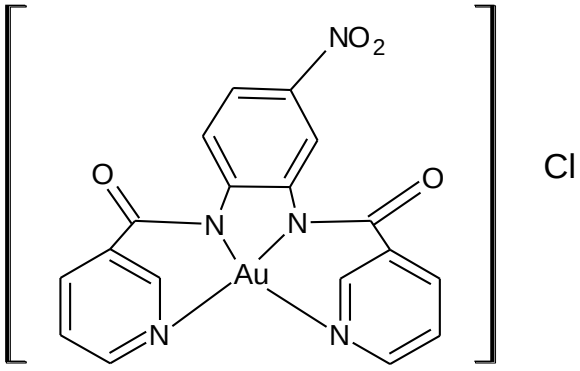

Figure1.8.5: Structure of gold(III) bis(pyridyl)carboxamide.

Both the gold(III) porphyrins and bis(pyridyl)carboxamide complexes have dianionic, tetradentate *N*-donor ligands. These ligands have been shown to stabilise the gold (III) ion

under physiological conditions. This suggests that the ligands proposed in this work which are also examples of dianionic tetradentate *N*-donor ligands will similarly stabilise the gold(III) ion.

1.9 Schiff bases

The ligands that will be coordinated to gold(III) in this work are examples of Schiff bases. Schiff bases are derived from primary amines and carbonyl compounds. These ligands coordinate through the azomethine nitrogen atoms. Schiff bases have many applications and are found in the food industry, analytical chemistry, catalysis and biological applications [30].

A scheme for the general synthesis of a Schiff base is shown in Figure 1.9.1. Schiff base reactions are mostly reversible and the use of an acid/base catalyst or heating is employed during the reaction. This reaction does not follow a nucleophilic addition, but forms an unstable intermediate compound, carbinolamine. Due to the unstable nature of the carbinolamine, it eliminates a water molecule. This step leads to the formation of the Schiff base and is the rate determining step [29].

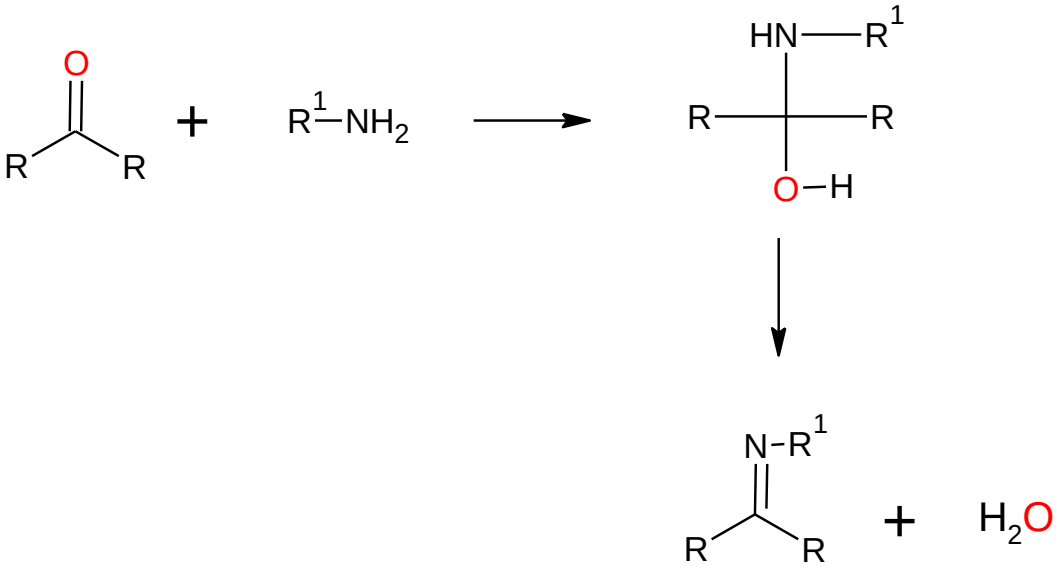

Figure 1.9.1: Scheme for a general Schiff base synthesis.

Schiff bases derived from pyrrole are mainly used in the pharmaceutical field and in electroconducting polymers. Imidazole derived Schiff bases are used in a wide range of applications in the pharmaceutical field such as anti-fungals, anti-inflammatories, anti-tubular activities, anti-depressants, anti-cancer agents and anti-virals. 4-methyl imidazole, one of the key compounds in this work, is similarly used in pharmaceuticals as a raw material, but is also found in chemical dyes and rubber. Imidazole and 4-methyl imidazole have also been commonly

used as starting material for ligands [26]. These ligands coordinate through the nitrogen atoms with a wide variety of transition metals, for example copper(II), manganese(II), nickel(II) and zinc(II) [31].

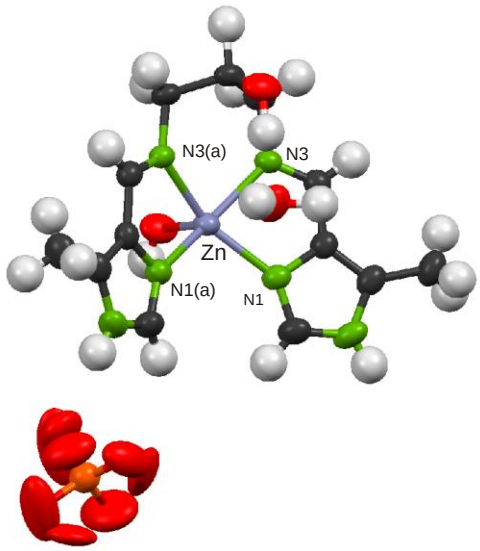

Figure 1.9.2: Structure of Imidazole derived Schiff bases with a zinc(II) metal centre [31].

The methyl imidazole analogues of the ligands proposed for chelation to gold(III) have been successfully coordinated to a range of metal ions including zinc(II) and copper(II) [31]. A notable feature of the chelates is that the coordination sphere is square planar. This coupled with the planarity of the imidazole-imine moiety suggests that these compounds will effectively intercalate DNA. The addition of a methyl group at the 4-position of the imidazole would have an inductive effect making the nitrogen atoms stronger sigma donors and will likely further stabilise the gold(III) ion.

1.10 Proposed Research

The aim of this project is to synthesise a range of bis(imidazole-imine) ligands. The ligands and complexes are varied by the structures of the di(azomethine) linkage. Seven of the ten ligands are novel, ligands H_2L4, H_2L7 and H_2L7 have previously been synthesised. Metal chelation will require deprotonation of the imidazole NH leading to a dianionic ligand. Coordination of these dianionic ligands to the gold(III) ion will yield a monocationic complex. The compounds have been designed to intercalate DNA and inhibit the topoisomerase enzyme thus preventing tumour cell replication. Ten ligands are proposed for chelation to gold(III) (Figure 1.10.1).

The gold(III) complexes have a planar aromatic region, a hydrogen bonding region (in some cases) and an overall positive charge. They are therefore anticipated to be effective DNA intercalators and chemotherapeutic agents. Both gold(III) porphyrins and gold(III) bis(pyridyl)carboxamide complexes have dianionic, tetradentate ^{N}-donor ligands. These ligands have been shown to stabilize the gold(III) ion under physiological conditions. This suggests that the ligands proposed in this work will sufficiently stabilise the gold(III) ion.

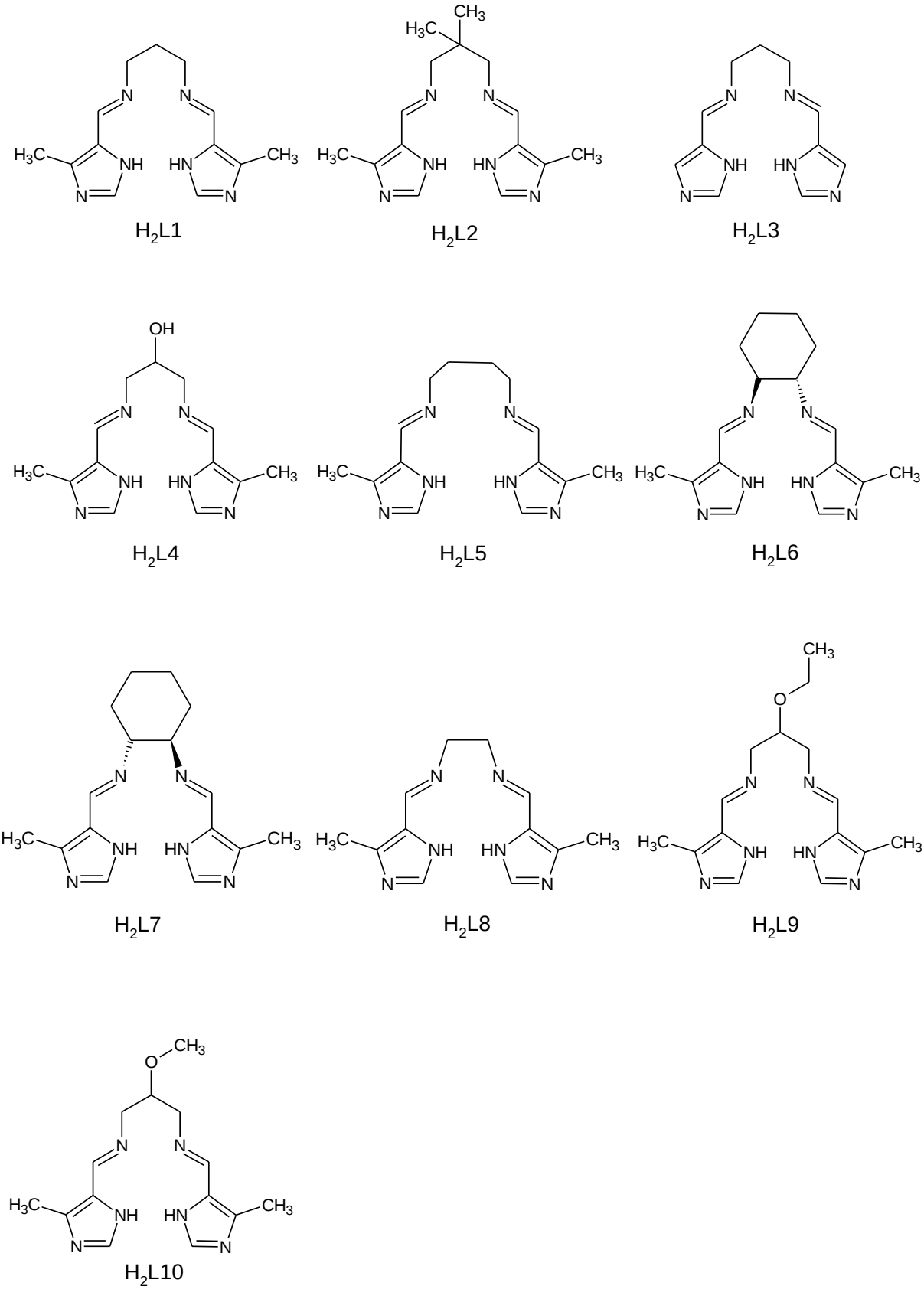

Figure 1.10.1: Structures and abbreviated names of the bis(imidazole-imine) Schiff base ligands proposed for chelation to gold(III).

1.11 Objectives

1. To synthesise a range of bis(imidazole-imine) ligands.
2. Fully characterize the free ligands by ^{1}H, ^{13}C, IR and UV/visible spectroscopy and mass spectrometry.
3. To synthesise a range of novel bis(imidazole-imine) gold(III) Schiff base complexes.
4. Fully characterize the gold complexes by ^{1}H, ^{13}C, ^{19}F, ^{31}P, IR and UV/visible spectroscopy as well as mass spectrometry.
5. Study the ligands and metal chelates by single crystal X-ray crystallography.
6. Computational studies, using DFT (density functional theory), will be performed on free ligands and gold(III) complexes. The results of the DFT will be compared to the experimental data to determine accuracy as well as to aid in interpretation of the experimental data.
7. Determine the affinity of the metal chelates for calf-thymus DNA.

1.12 References

1. Zimmerman, M.*Am. J. Phys. Anthropol*., **1979**, 51, 235-253.
2. Cancer in Africa, American Cancer Society, Atlanta, 2011.
3. Ryerson, A.; Eheman, C.; Altekruse, S.; Ward, J.; Jemal, A.; Sherman, R.; Henley, S.; Holtzman, D.; Lake, A. and Noone, A. *Cancer* **2016**, 122, 1312-1337.
4. Templeton, D. M., *Toxic*, **2015**, *3*,170-186.
5. Fricker, S., *Medical Uses Of Gold Compounds Past, Present And Future*; World Gold Council, Londres, 1996.
6. Clapp, R.W.; Jacobs, M.M. and Loechler, E.L. , *Rev. Environ. Health*, 2008, 23, 1–37.
7. Proctor, R. *Cancer wars*; BasicBooks: New York, 1995.
8. Rahman, A. Studies In Natural Products Chemistry; Elsevier: Amsterdam, 2013; p. 4.
9. Snustad, D. Simmons, M. *Principles Of Genetics*; 4th ed.; Wiley; 2006; pp. 687-690.
10. Brenner, D.Hall, E. *Making the radiation therapy decision*; Lowell House: Los Angeles, 1996.
11. Bremers, A.; Rutgers, E.; van de Velde, C., *Cancer Treat. Rev.*,**1999**, 25, 333-353.
12. Payne S and Miles D. Mechanisms of anticancer drugs. Edited by Michael Gleeson. *CRC press*. 2008.
13. Ithimakin, S.; Chuthapisith, S. Neoadjuvant Chemotherapy - Increasing Relevance In Cancer Management; *InTech*, 2013; p. 49.
14. William, D. *The Design and Development of Anticancer Drugs; Chemical Processes in New Zealand, Volume 2*; 1st ed.; New Zealand Institute of Chemistry, 1998, 1998.
15. Richards, A.Rodger, A. *Chem. Soc. Rev*. **2007**, 36, 471-483.
16. Liu, H.; Sadler, P., *Acc. Chem. Res.* ,**2011**, 44, 349-359.
17. Brian M. Zeglis, Valerie C. Pierre and Jacqueline K. Barton*., Chem. Commun*., **2007**, 4565–4579
18. Rescifina, A.; Zagni, C.; Varrica, M.; Pistarà, V.; Corsaro, A.*, Eur. J. Med. Chem.*, **2014**, 74, 95-115.
19. Richards, A.; Rodger, A., *Chem. Soc. Rev.*, **2007**, 36, 471-483.
20. Galluzzi, L.; Senovilla, L.; Vitale, I.; Michels, J.; Martins, I.; Kepp, O.; Castedo, M.; Kroemer, G., *Oncogene* ,**2011**, 31, 1869-1883.
21. Victoria Cepeda; Miguel A. Fuertes; Josefina Castilla; Carlos Alonso1; Celia Quevedo and Jose M. Pérez., Anticancer Agents Med. Chem., **2007**, 7, 3-18.
22. Florea, A.; Büsselberg, D., *Cancer*, **2011**, 3, 1351-1371.

23. Andersen, A.H., Bendixen, C., and Westergaard, O., *DNA Topoisomerases*, *DNA* Replication in Eukaryotic Cells, Cold Spring Harbor Laboratory Press: [Plainview, New York], 1996; pp. 587-617.
24. Dwarakanath, B.; Khaitan, D.; Mathur, R*., Indian J. Exp. Biol., **2004***, 42, 649-549.
25. Comins, D. L., *Org. Lett*, **2001**, 3, 4255-4257.
26. Sun, R.; Li, C.; Ma, D.; Yan, J.; Lok, C.; Leung, C.; Zhu, N.; Che, C., *Chem. Eur. J.l*, **2010**, 16, 3097-3113.
27. Milacic, V.; Dou, Q., *Coord. Chem. Rev.* **2009**, 253, 1649-1660.
28. Prakash, A., Adhikari, D*., Int. J. ChemTech Res.*, **2011**, 3, 1891-1896
29. Anis, I.; Aslam, M.; Afza, N.; Iqbal, L.; Noreen, Z.; Hussain, A.; Safder, M., *ChemInform*, **2015**, 46.
30. Shalini, K.,Sharma, P.K., Kumar, N., *Der Chem Sinica*, **2010**, 1 (3): 36-47
31. Long, L.; Chen, X.; Yu, X.; Zhou, Z.; Ji, L., *Polyhedron*, **1999**,18, 1927-1933.
32. James J. Champoux., *Annu. Rev. Biochem*., **2001**. 70:369–413
33. Milacic, V., Fregona, D., and Dou, Q.P., *Histo.l Histopathol.* ,**2008**, 23: 101-108
34. Mames, I.; Rodger, A.; Kowalski, J., *Eur. J. Inorg. Chem*., **2015**, 2015, 630-639.
35. Milacic, V.Dou, Q. *Coord. Chem. Rev.* **2009**, 253, 1649-1660.

Chapter 2| Experimental

2.1 General Methods

All starting materials used in the syntheses were purchased from Sigma-Aldrich (Germany) and used as received. Organic solvents were purchased from Merck (South Africa) and were of analytical reagent (AR) grade. Harmony gold provided the metallic gold (99.999%) which was in the form of gold pellets. Merck silica gel 60 was used for column chromatography.

2.2 Instrumentation

NMR spectra were recorded with a Bruker Avance III 400 MHz spectrometer equipped with a Bruker magnet (9.395 T) using a 5 mm TBIZ probe at the following frequencies: ^{1}H = 400 MHz, ^{13}C = 100 MHz, ^{31}P = 162 MHz and ^{19}F = 376 MHz. The spectra were recorded at 30 °C. All NMR experiments were conducted using Bruker Topspin 2.1, patch level 6. All proton and carbon chemical shifts are quoted relative to the solvents used, DMSO-*d6*: ^{1}H, 2.50 ppm, ^{13}C, 39.52 ppm; $CDCl_3$: ^{1}H 7.26 ppm, ^{13}C, 77.16 ppm and CD_3OD:^{1}H, 3.31 ppm, ^{13}C, 49.00 ppm. The 2D COSY and HSQC data assisted with the assigning of the ^{1}H and ^{13}C NMR spectra for the ligands and metal complexes.

FTIR spectra were recorded using a Bruker Alpha FTIR spectrometer equipped with an ATR Platinum Diamond 1 reflectance accessory. The machine acquired the information in 32 scans with a spectral resolution of 1.0 cm^{-1}. Electronic spectra were recorded using a Shimadzu UVPC-1800 double beam UV-vis scanning spectrometer (1.0 cm path length cuvette). Spectra were recorded from 800 to 200 nm.

High resolution mass spectra were recorded with a Waters Acquity-LCT Premier coupled high performance liquid chromatograph-mass spectrometer (time-of-flight) using electrospray ionization in positive mode.

All experimental data are available in Appendix A

2.3 Synthesis of Ligand Precursors

2.3.1 Synthesis of 2,2,12,12-tetramethyl-3,11-dioxo-4,10-dioxa-5,9-diazatridecan-7-ol

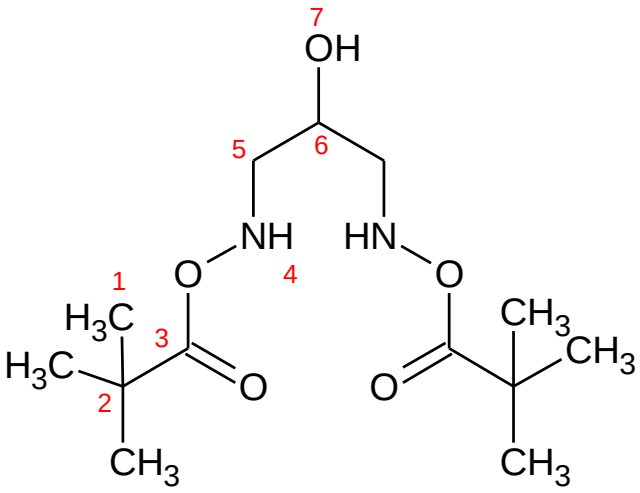

Figure 2.3.1: Structure and atom numbering scheme of 2,2,12,12-tetramethyl-3,11-dioxo-4,10-dioxa-5,9-diazatridecan-7-ol.

Sodium hydrogencarbonate (8.3 g, 99 mmol) was dissolved in a water:acetonitrile mixture (190 mL ratio of 1:1). The solution was placed in an ice bath and cooled to 4 ˚C. Di-tert-butyldicarbonate (12.8 g, 59 mmol) and 1,3-diamino-2-hydroxypropane (2.5 g, 27 mmol) were dissolved in the same solvent system (65 mL). This solution was added to the cooled solution and stirred in an ice bath for 2 hours. The reaction was warmed to room temperature and stirred overnight. The acetonitrile was removed by rotary evaporation. The desired amine was then extracted into DCM (3 × 75 mL portions). The organic portions were combined and dried over anhydrous sodium carbonate; the DCM was removed by rotary evaporation. The crude product was re-crystallized from diethylether/hexane, resulting in colourless crystals (7.4 g, 93.5 % yield). The crystals were characterized by ^{1}H and ^{13}C NMR and IR spectroscopy.

^{1}H NMR (400 MHz, $CDCl_3$, 303K)[δ, ppm]: 1.45 (s, 18H, H-1), 3.21 (m, 4H, H-5), 3.75 (m, 2H, H-6 and H-7), 5.18 (s br, 2H, H-4). ^{13}C NMR (100 MHz, $CDCl_3$, 303k) [δ, ppm]: 28.56 (1), 43.74 (2), 71.09 (5), 79.86 (6), 157.27 (3). IR (cm^{-1}): 3316m br (OH and NH), 2971 m and 2930 m υ(CH_3 and CH), 1681s υ(C=O).

2.3.2 Synthesis of 2-ethoxypropane-1,3-diaminium dichloride

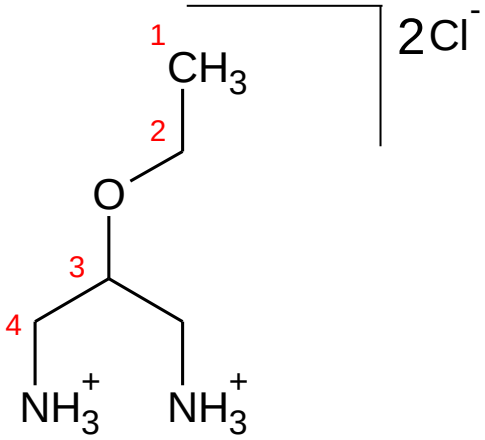

Figure 2.3.2: Structure and atom numbering scheme of 2-ethoxypropane-1,3-diaminium dichloride.

The precursor 2,2,12,12-tetramethyl-3,11-dioxo-4,10-dioxa-5,9-diazatridecan-7-ol (2.0 g, 6.9 mmol) and $[Bu_4N][HSO4]$ (0.44 g, 1.3 mmol) were dissolved in toluene (7.5 mL). A 50% aqueous solution of NaOH (7.5 mL) and ethyl iodide (1.67 mL, 20.7 mmol) were added to the toluene solution. The reaction mixture was then heated to 100 ˚C for 18 hours. The reaction mixture was diluted with water (50 mL) and the alkylated compound extracted into ethylacetate (75 mL) and washed with 5% brine and dried over anhydrous Na_2CO_3. The solvent was removed by rotary evaporation. The resulting oil was purified by column chromatography on silica gel using 1:4 ethylacetate:hexane as the eluent. The alkylated compound was collected and the solvent removed by rotary evaporation. The resulting oil was dissolved in HCl in dioxane (4 M) and stirred for 4 hours. A white precipitate formed and was separated from the HCl solution by centrifugation, washed with THF and diethyl ether and dried over P_2O_5. The product was characterised by ^{1}H NMR spectroscopy.

^{1}H NMR (400 MHz, D_2O, 303 K) [δ, ppm]: 1.21 (t, 3H, H-1), 3.12 (dd, 2H, $^3J_1$=7.13 Hz, $^3J_2$=14.3 Hz, H-4), 3.32 (dd, 2H, $^3J_1$=4.2 Hz, $^3J_2$=12.9 Hz, H-4), 3.69 (q, 2H, H-2), 4.03 (m, 1H, H-3),

2.3.3 Synthesis of 2-methoxypropane-1,3-diaminium dichloride

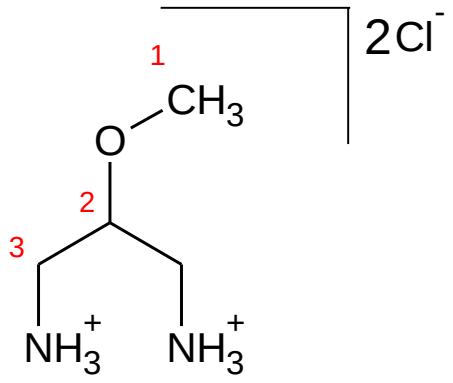

Figure 2.3.3: Structure and atom numbering scheme of 2-methoxypropane-1,3-diaminium dichloride.

The precursor 2,2,12,12-tetramethyl-3,11-dioxo-4,10-dioxa-5,9-diazatridecan-7-ol (2.0 g, 6.9 mmol) and $[Bu_4N][HSO_4]$ (0.44 g, 1.3 mmol) were dissolved in toluene (7.5 mL). A 50% aqueous NaOH solution (7.5 mL) and methyl iodide (1.67 mL, 20.7 mmol) were then added to the toluene solution. The reaction mixture was then heated to 100 ˚C for 18 hours. The solution was diluted with water (50 mL) and the alkylated compound extracted into ethylacetate (75 mL) and washed with 5% brine and dried over anhydrous Na_2CO_3. The solvent was removed by rotary evaporation. The resulting oil was purified by column chromatography on silica gel using 1:4 ethylacetate:hexane as the eluent. The alkylated compound was collected and the solvent removed by rotary evaporation. The resulting oil was dissolved in HCl in dioxane (4 M) and stirred for 4 hours. A white precipitate formed and was separated from the HCl solution by centrifugation, washed with THF and diethyl ether and dried over P_2O_5. The product was characterised by ^{1}H NMR spectroscopy.

^{1}H NMR (400 MHz, D_2O, 303 K) [δ, ppm]: 2.77 (s, 3H,H-1), 3.33 (dd, 2H, $^3J_1$=7.13 Hz, $^3J_2$=14.3 Hz, H-3), 3.89 (m, 1H, H-2),

2.4 Synthesis of Ligands

2.4.1 Synthesis of N,N'-bis[(E)-(4-methyl-1H-imidazol-5-yl) methylidene]propane- 1,3-diamine (H_2L1)

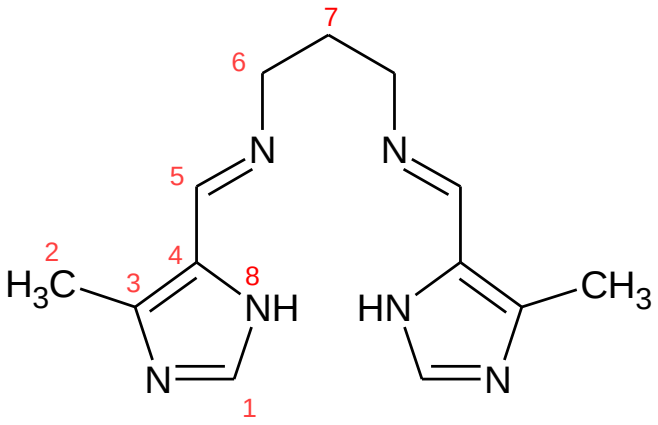

Figure 2.4.1: Structure and atom numbering scheme used for H_2L1.

The ligand precursor 4-methyl-1*H*-imidazole-5-carbaldehyde (0.500 g, 4.54 mmol) was dissolved in ethanol (20 mL). To this solution was added 1,3-diaminopropane (0.189 mL, 2.27 mmol) (ratio of 4-methyl-1*H*-imidazole-5-carbaldehyde: 1,3-diaminopropane is 2:1). The resulting mixture was heated to reflux for 3 hours during which a white precipitate formed. The precipitate was isolated by gravity filtration, yielding the final product (0.483 g, 1.86 mmol, 81.9 % yield). The product was analysed by ^{1}H and ^{13}C NMR, IR and UV/visible spectroscopy as well as mass spectrometry.

^{1}H NMR (400 MHz, CD_3OD, 303 K) [δ ppm]: 2.05 (m, 2H, H-7), 2.37 (s, 6H, H-2), 3.56 (s, 4H, H-6), 7.54(s, 2H, H-1), 8.24(s, 2H, H-5), 12.14 (s, 2H, NH). ^{13}C NMR (100 MHz, DMSO-d_6, 303 K), [δ ppm]: 10.33 (2), 31.88 (7), 58.15 (6), 128.46 (1), 134.34 (3), 137.50 (4), 150.22 (5). IR (cm^{-1}): 2931.55 υ(NH), 1645.02 υ(C=N), 1307.49 υ(C-N stretch), 1461.92 υ(C-C aromatic region). UV-vis (CH_3OH) λ_{max} [nm] (ε/ M^{-1} cm^{-1}): 266 (2.01×10^4). ESI-MS: m/z 281.1491 ($M+Na^+$), calculated m/z: 281.1485 ($M+Na^+$).

2.4.2 Synthesis of 2,2-dimethyl-N,N'-bis[(E)-(4-methyl-1H-imidazol-5-yl) methylidene] propane- 1,3-diamine (H_2L2)

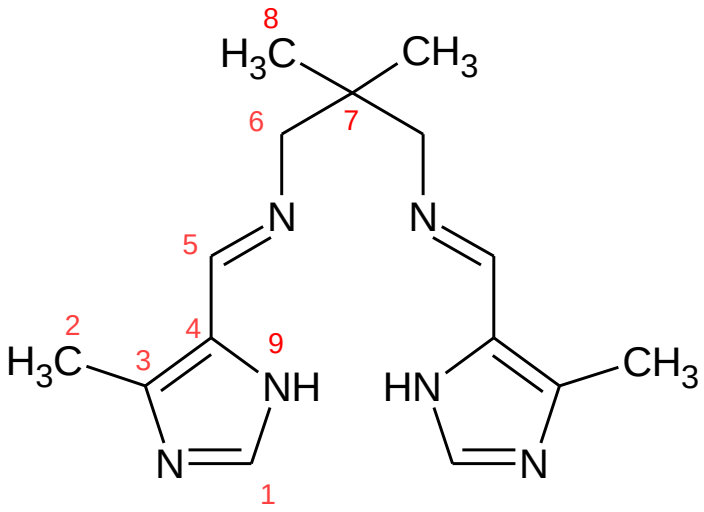

Figure 2.4.2: Structure and atom numbering scheme used for H_2L2.

The ligand precursor 4-methyl-1*H*-imidazole-5-carbaldehyde (0.500 g, 4.54 mmol) was dissolved in ethanol (20 mL). To this solution was added 2,2-dimethylpropane-1,3-diamine (0.273 mL, 2.27 mmol). The resulting mixture was then heated to reflux for 3 hours, yielding a yellow solution. The volume of solvent was reduced *via* a rotary evaporation giving a light yellow precipitate. The precipitate was isolated by gravity filtration, yielding the final product (0.432 g, 1.51 mmol, 66.5 % yield). The product was analysed by ^{1}H and ^{13}C NMR, IR and UV/visible spectroscopy as well as mass spectrometry.

^{1}H NMR (400 MHz, CD_3OD CD_3OD, 303 K) [δ ppm]: 0.93 (s, 6H, H-8), 2.32 (s, 6H, H-2), 2.50 (s, 4H, H-6), 7.56 (s, 2H, H-1), 8.20 (s, 2H, H-5). ^{13}C NMR (100 MHZ, CD_3OD, 303 K), [δ ppm]: 10.56 (2),
23.55 (8), 36.19 (7), 69.14 (6), 127.73 (1), 133.85 (3), 137.24 (4), 152.27 (5). IR (cm^{-1}): 2807.19 υ(NH), 1645.85 υ(C=N), 1336.47.49 υ(C-N stretch), 1456.47 υ(C-C aromatic region). UV-vis (CH_3OH) λ_{max} [nm] (ε/ M^{-1} cm^{-1}): 267 (1.35×10^5). ESI-MS: m/z 287.1985 (M^+), calculated m/z: 286.1905 Da ($M\text{-}H^+$).

2.4.3 Synthesis of N,N'-bis[(E)-1H-imidazol-5-ylmethylidene]propane-1,3- diamine (H_2L3)

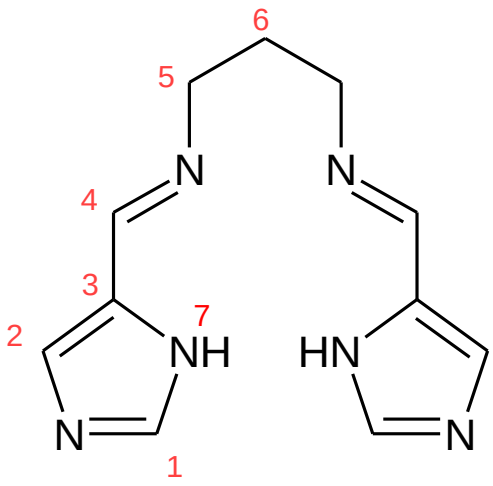

Figure 2.4.3: Structure and atom numbering scheme used for H_2L3.

The ligand precursor 1*H*-imidazole-5-carbaldehyde (0.500 g, 5.20 mmol) was dissolved in ethanol (20 mL). To this solution was added 1,3 –diaminopropane (0.217 mL, 2.601 mmol). The resulting mixture was heated to reflux for 3 hours during which a white precipitate formed. The precipitate was isolated by gravity filtration, yielding the final product (0.402 g, 1.75 mmol, 67.3% yield). The product was analysed by ^{1}H and ^{13}C NMR, IR and UV/visible spectroscopy as well as mass spectrometry.

^{1}H NMR (400 MHz, DMSO-d_6, 303 K) [δ ppm]: 1.97 (m, 2H, H-6), 3.65 (t, 4H, H-5), 7.07 (s, 2H, H-2), 7.19(s, 2H, H-1), 8.19(s, 2H, H-4), 12.57 (s, 2H, NH). ^{13}C NMR (100MHz, DMSO-d_6, 303 K), [δ ppm]: 32.19 (6), 58.29 (5), 119.59 (2), 130.08 (1), 145.04 (3), 152.76 (4). IR (cm^{-1}): 2831.54 υ(NH) 1648.24, υ(C=N), 1387.39 υ(C-N stretch), 1447.73 υ(C-C aromatic region). UV-vis (CH_3OH) λ_{max} [nm] (ε/ M^{-1} cm^{-1}): 273.5 (9.00×10^4). ESI-MS: m/z 253.1178 ($M+Na^+$), calculated m/z: 253.11721 ($M+Na^+$).

2.4.4 Synthesis of *N,N'*-bis[(*E*)-1*H*-imidazol-5-ylmethylidene]propane-1,3- diamine (H_2L4)

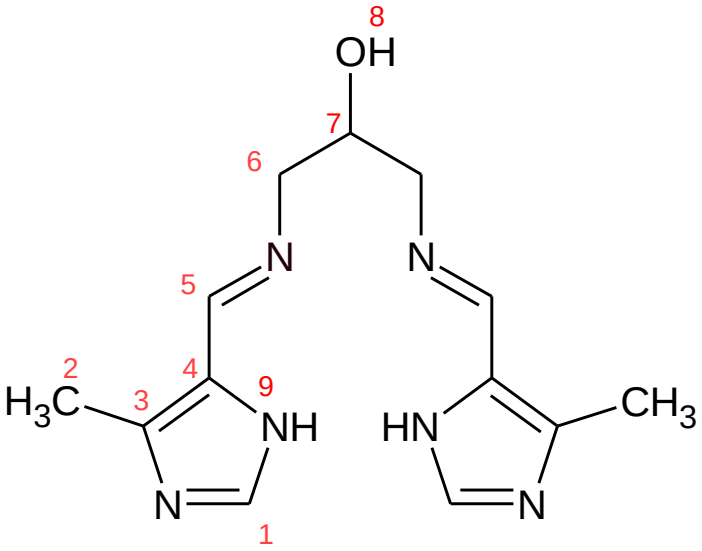

Figure 2.4.4: Structure and atom numbering scheme used for H_2L4.

The ligand precursor 4-methyl-1*H*-imidazole-5-carbaldehyde (0.500 g, 4.54 mmol) was dissolved in ethanol (20 mL). To this solution was added 1,3-diamino-2-propanol (0.204 g, 2.27 mmol). The resulting mixture was then heated to reflux for 3 hours during which a pale pink precipitate formed. The precipitate was isolated by gravity filtration and was washed with ethanol, yielding the final product (0.412g, 1.50 mmol, 66.1% yield). The product was analysed by ^{1}H and ^{13}C NMR, IR and UV/visible spectroscopy as well as mass spectrometry.

^{1}H NMR (400 MHz, DMSO-d_6, 303 K) [δ, ppm]: 2.31 (s, 6H, H-2), 2.45 (s, 1H, H-8), 3.48 (dd, 2H, $^{6}J_1$=6.4 Hz, $^{6}J_2$=11.2 Hz, H-6), 3.68 (dd, 2H, $^{6}J_1$=6.1 Hz, $^{6}J_2$=7.2 Hz, H-6), 3.91 (m, 1H, H-7), 7.13(s, 2H, H-1), 8.19 (s, 2H, H-5), 12.11 (s, 2H, NH). ^{13}C NMR (100 MHZ, DMSO-d_6, 303 K) [δ ppm]: 10.29 (2), 56.52 (7), 65.79 (6), 126.00 (1), 137.06 (3), 141.42 (4), 151.79 (5). IR (cm^{-1}): 2848.34 υ(NH), 1648.24 υ(C=N), 1387.39 υ(C-N stretch), 1447.73 υ(C-C aromatic region). UV-vis (CH_3OH) λ_{max} [nm] (ε/ M^{-1} cm^{-1}): 267.5 (1.37×10^5). ESI-MS: m/z 297.1442 ($M+Na^+$), calculated m/z: 297.1434 ($M+Na^+$).

2.4.5 Synthesis of *N,N'*-bis[(1*E*)-(4-methyl-1*H*-imidazol-5-yl)methylene]butane- 1,4-diamine (H_2L5)

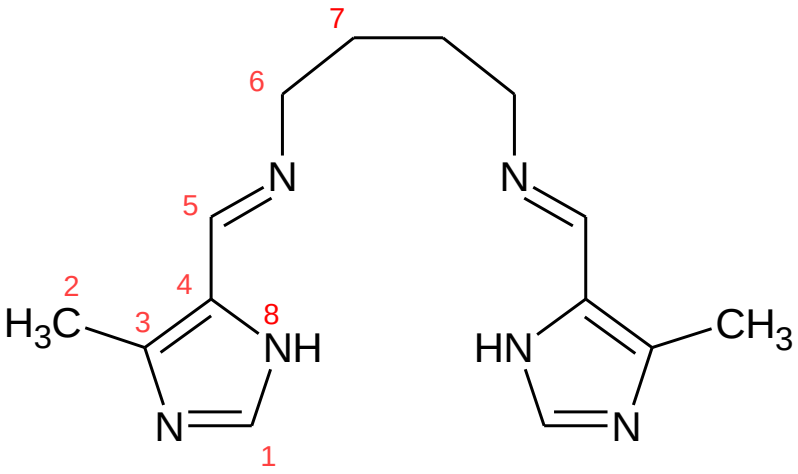

Figure 2.4.5: Structure and atom numbering scheme used for H_2L5.

The ligand precursor 4-methyl-1*H*-imidazole-5-carbaldehyde (0.500 g, 4.54 mmol) was dissolved in ethanol (20 mL). To this solution was added 1,4-diaminobutane (0.228 mL, 2.27 mmol). The resulting mixture was then heated to reflux for 3 hours during which a pale yellow precipitate formed. The precipitate was isolated by gravity filtration, yielding the final product (0.372 g, 1.37 mmol, 60.4% yield). The product was analysed by ^{1}H and ^{13}C NMR, IR and UV/visible spectroscopy as well as mass spectrometry.

^{1}H NMR (400 MHz, CD_3OD/ $CDCl_3$, 303 K) [δ ppm]:1.62 (m, 4H, H-7), 2.26 (s, 6H, H-2), 3.51 (t, 4H, H-6), 7.52 (s, 2H, H-1), 8.27 (s, 2H, H-5). ^{13}C NMR (100 MHz, CD_3OD/ $CDCl_3$, 303 K), [δ ppm]: 11.38 (2), 28.59 (7), 60.37 (6), 124.96 (1), 136.86 (3), 142.81 (4), 150.69 (5). IR (cm^{-1}): 2856.69 υ(NH), 1645.38 υ(C=N), 1356.92 υ(C-N stretch), 1443.84 υ(C-C aromatic region); UV-vis (CH_3OH) λ_{max} [nm] (ε/ M^{-1} cm^{-1}): 265 (3.0×10^4). ESI-MS: m/z 295.1651 ($M+Na^+$), calculated m/z: 295.1641 ($M+Na^+$).

2.4.6 Synthesis of (1*S*,2*S*)-*N*,*N*′-bis[(*E*)-(4-methyl-1H-imidazol-5-yl) methylidene]cyclohexane-1,2-diamine (H_2L6)

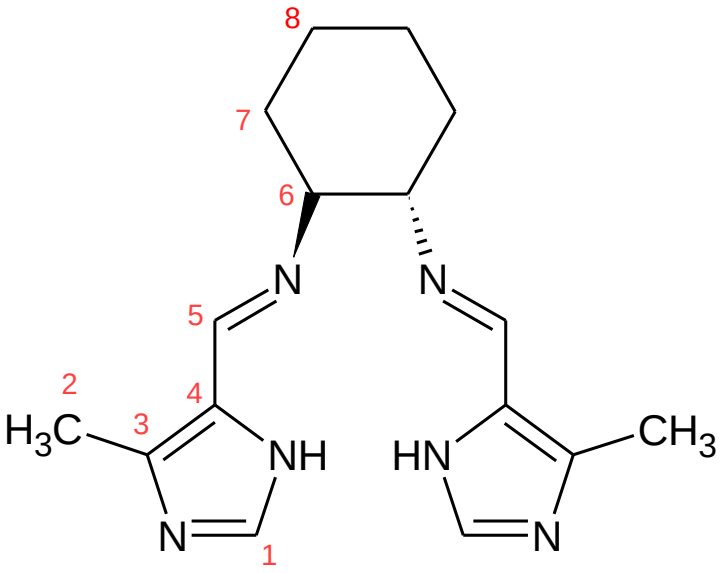

Figure 2.4.6: Structure and atom numbering scheme used for H_2L6.

The ligand precursor 4-methyl-1*H*-imidazole-5-carbaldehyde (0.500 g, 4.54 mmol) was dissolved in ethanol (20 mL). To this solution was added (*1S,2S*)-(+)-1,2-diaminocyclohexane (0.273 mL, 2.27 mmol). The resulting mixture was then heated to reflux for 3 hours after which a clear brown solution was obtained. The volume of solvent was reduced *via* rotary evaporation and a brown oil formed from which a brown precipitate formed on standing overnight (0.536 g, 1.80 mmol , 79.3% yield). The product was analysed by ^{1}H and ^{13}C NMR, IR and UV/visible spectroscopy as well as mass spectrometry.

^{1}H NMR (400 MHz, DMSO-d_6, 303 K) [δ ppm]: 1.40 (m, 4H, H-8), 1.77 (m, 4H, H-7), 2.29 (s, 6H, H-2), 3.21 (m, 2H, H-6), 7.44 (s, 2H, H-1), 8.06 (s, 2H, H-5) , 12.00 (s, 2H, NH). ^{13}C NMR (100 MHz, DMSO-d_6, 303 K) [δ ppm]: 11.88 (2), 24.65 (8), 33.57 (7), 74.20 (6), 125.96 (1), 136.67 (3), 141.62 (4), 150.09 (5). IR (cm^{-1}): 2847.77 υ(NH), 1634.61 υ(C=N), 1362.30 υ(C-N stretch), 1443.57 υ(C-C aromatic region). UV-vis (CH_3OH) λ_{max} [nm] (ε/ M^{-1} cm^{-1}): 260 (2.11×10^4). ESI-MS: m/z 299.1981 ($M+H^+$), calculated m/z: 298.1906 (M^+).

2.4.7 Synthesis of (1*R*,2*R*)-*N*,*N*′- bis[(*E*)- (4-methyl-1H-imidazol-5-yl) methylidene]cyclohexane-1,2-diamine (H_2L7)

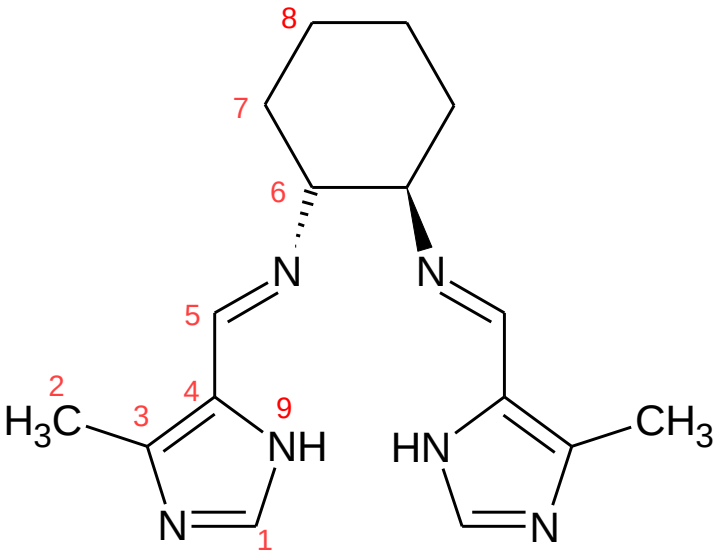

Figure 2.4.7: Structure and atom numbering scheme used for H_2L7.

The ligand precursor 4-methyl-1*H*-imidazole-5-carbaldehyde (0.500 g, 4.54 mmol) was dissolved in ethanol (20 mL). To this solution was added (*1R,2R*)-(-)-1,2-diaminocyclohexane (0.273 mL, 2.27 mmol). The resulting mixture was then heated to reflux for 3 hours, after which a clear brown solution was obtained. The volume of solvent was reduced *via* rotary evaporation leaving a brown oil from which a brown precipitate formed on standing (0.554 g, 1.86 mmol, 81.9% yield). The product was analysed by ^{1}H and ^{13}C NMR, IR and UV/visible spectroscopy as well as mass spectrometry.

^{1}H NMR (400 MHz, DMSO-d_6, 303 K) [δ ppm]: 1.40 (m, 4H, H-8), 1.76 (m, 4H, H-7), 2.13 (s, 6H, H-2), 3.20 (m, 2H, H-6), 7.45 (s, 2H, H-1), 8.07 (s, 2H, H-5) , 12.02 (s, 2H, NH). ^{13}C NMR (100 MHz, DMSO-d_6, 303 K) [δ ppm]: 11.6(2), 24.62(8), 33.36 (7), 58.20 (6), 130.18 (1), 136.14 (3), 138.02 (4), 152.04 (5). IR (cm^{-1}): 2853.12 υ(NH), 1645.38 υ(C=N), 1356.91 υ(C-N stretch), 1443.84 υ(C-C aromatic region). UV-vis (CH_3OH) λ_{max} [nm] (ε/ M^{-1} cm^{-1}): 268 (2.4×10^4). ESI-MS: m/z 299.1985 ($M+H^+$), calculated m/z: 298.1906 (M^+).

2.4.8 Synthesis of *N,N'*-bis[(1*E*)-(4-methyl-1*H*-imidazol-5-yl)methylene]ethane- 1,2-diamine (H_2L8)

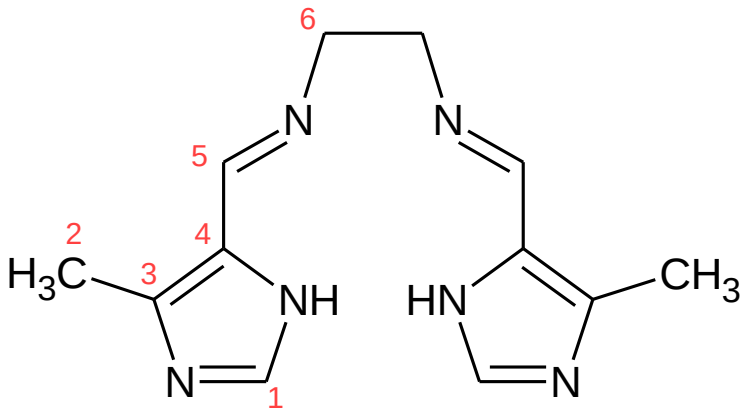

Figure 2.4.8: Structure and atom numbering scheme used for H_2L8.

The ligand precursor 4-methyl-1*H*-imidazole-5-carbaldehyde (0.500 g, 4.54 mmol) was dissolved in ethanol (20 mL). To this solution was added 1,2-diaminoethane (0.152 mL, 2.27 mmol). The resulting mixture was then heated to reflux for 3 hours during which a pale yellow precipitate formed. The precipitate was isolated by gravity filtration, yielding the final product (0.421 g, 1.72 mmol, 75.8% yield). The product was analysed by ^{1}H and ^{13}C NMR, IR and UV/visible spectroscopy as well as mass spectrometry.

^{1}H NMR (400 MHz, CD_3OD/ $CDCl_3$, 303 K) [δ ppm]: 2.26 (s, 6H, H-2), 3.82 (s, 4H, H-6), 7.52 (s, 2H, H-1), 8.20 (s, 2H, H-5), 12.09 (s, 1H, NH). ^{13}C NMR (100 MHZ, CD_3OD/ $CDCl_3$, 303 K), [δ ppm]: 15.32 (2), 60.06 (6), 129.51 (1), 140.53 (3), 145.56 (4), 156.63 (5). IR (cm^{-1}): 2841.43 υ(NH), 1634.63 υ(C=N), 1356.92 υ(C-N stretch), 1443.94 υ(C-C aromatic region). UV-vis (CH_3OH) λ_{max} [nm] (ε/ M^{-1} cm^{-1}): 265 (2.3×10^4). ESI-MS: m/z 267.1339 ($M+Na^+$), calculated m/z: 267.1328 ($M+Na^+$).

2.4.9 Synthesis of 2-ethoxy-*N*,*N*′-bis[(1*E*)-(4-methyl-1*H*-imidazol-5-yl)methylene]propane- 1,3-diamine (H_2L9)

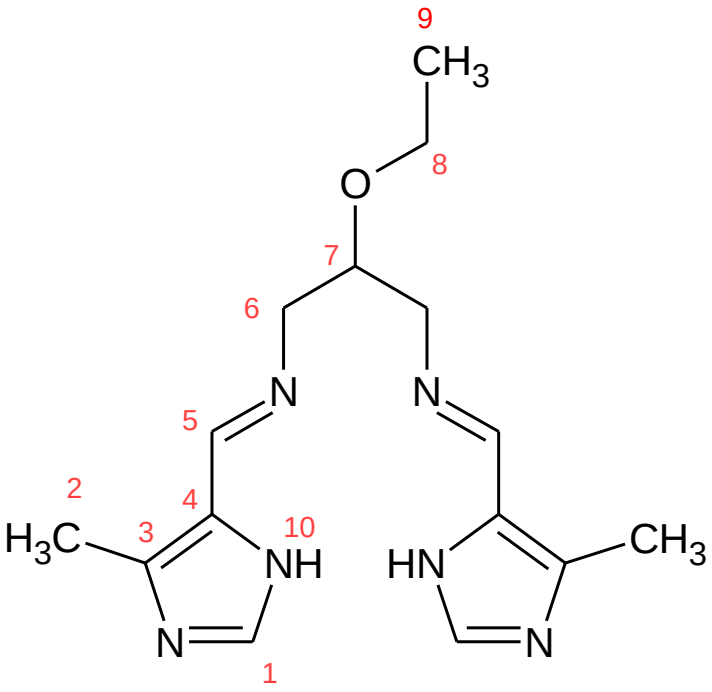

Figure 2.4.9: Structure and atom numbering scheme used for H_2L9.

The ligand precursor 2-ethoxy-1,3-diaminopropane dihydrochloride (0.500 g, 2.62 mmol) was placed in a pestle and mortar with sodium carbonate (0.555 g, 5.23 mmol) and the mixture ground together until a white paste was formed; a mixture of 2-ethoxy-1,3-diaminopropane and sodium chloride. 1*H*-imidazole-5-carbaldehyde (0.576 g, 5.23 mmol) was then added to the pestle and mortar together with 5 drops of piperidine. The mixture was ground together resulting in a pale brown solid. The solid was washed with distilled water and air dried (0.602 g, 1.99 mmol, 76.0% yield). The product was analysed by ^{1}H and ^{13}C NMR, IR and UV/visible spectroscopy as well as mass spectrometry.

^{1}H NMR (400 MHz, DMSO-d_6, 303 K) [δ ppm]: 1.02 (s, 3H, H-9), 2.08 (s, 4H, H-6), 2.31 (m, 6H, H-2), 3.54 (m, 2H, H-8), 3.70(m, 1H, H-7), 7.52 (s, 2H, H-1), 8.20 (s, 2H, H-5) , 12.18 (s, 1H, NH). ^{13}C NMR (100 MHz, CD_3OD, 303 K), [δ ppm]: 10.00 (9), 14.39 (2), 62.29 (8), 65.17 (7), 78.79 (6), 128.07 (1), 137.38 (3), 142.32 (4), 153.76 (5). IR (cm^{-1}): 2857.24 υ(NH), 1646.22 υ(C=N), 1342.15 υ(C-N stretch), 1433.33 υ(C-C aromatic region). UV-vis (CH_3OH) λ_{max} [nm] (ε/ M^{-1} cm^{-1}): 266(1.1×10^4). ESI-MS: m/z 325.1758 ($M+Na^+$), calculated m/z: 325.17473 ($M+Na^+$).

2.4.10 Synthesis of 2-methoxy-*N*,*N*′-bis[(1*E*)-(4-methyl-1*H*-imidazol-5-yl)methylene]propane-1,3-diamine (H_2L10)

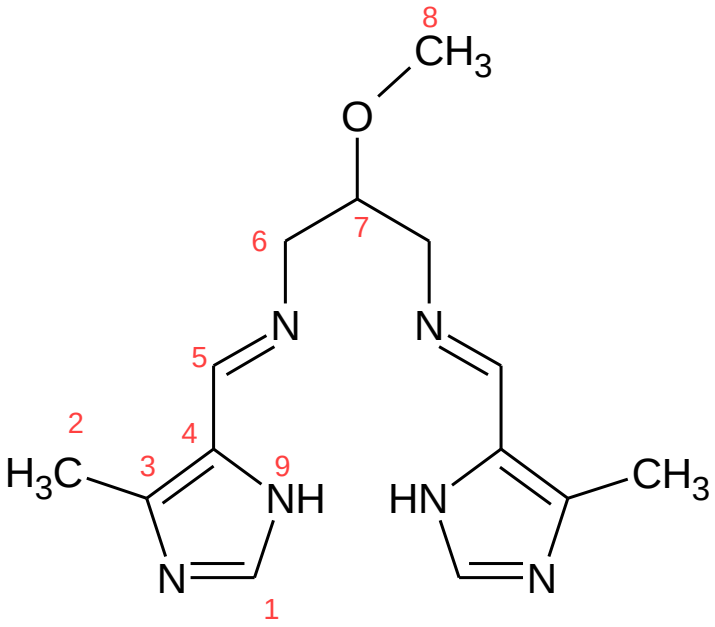

Figure 2.4.10: Structure and atom numbering scheme used for H_2L10.

The ligand precursor 2-methoxy-1,3-diaminopropane dihydrochloride (0.500 g, 2.83 mmol) was ground together with sodium carbonate (0.453 g, 5.54 mmol) in a pestle and mortar until a white paste was formed; a mixture of 2-ethoxy-1,3-diaminopropane and sodium chloride. 1*H*-imidazole-5-carbaldehyde was then added to the pestle and mortar together with 5 drops of piperidine and the mixture ground further resulting in a pale brown solid. The solid was then washed with distilled water and air dried (0.643 g, 2.23 mmol, 79.0% yield). The product was analysed by ^{1}H and ^{13}C NMR, IR and UV/visible spectroscopy as well as mass spectrometry.

^{1}H NMR (400 MHz, CD_3OD, 303 K) [δ ppm]: 2.39 (s, 6H, H-2), 3.33 (s, 3H, H-8), 3.73 (d, 4H, H-6), 3.83 (m, 1H, H-7), 7.66 (s, 2H, H-1), 8.30 (s, 2H, H-5). ^{13}C NMR (100 MHz, CD_3OD, 303 K), [δ ppm]: 10.07 (2), 56.68 (8), 61.79 (7), 80.67 (6), 127.87 (1), 136.00 (3), 142.43 (4), 154.03 (5). IR (cm^{-1}): 2857.36 υ(NH), 1644.80 υ(C=N), 1352.16 υ(C-N stretch), 1440.11 υ(C-C aromatic region). UV-vis (CH_3OH) λ_{max} [nm] (ε/ M^{-1} cm^{-1}): 266 (1. 2 × 10^4). ESI-MS: m/z 311.1601 ($M+Na^+$), calculated m/z: 311.1590 ($M+Na^+$).

2.5 Synthesis of Complexes

2.5.1 Synthesis of 5,5'-{propane-1,3-diylbis [nitrilo(*E*) methylylidene]} bis(4-methylimidazol-1-ide) gold(III) hexafluorophosphate(V) [Au(L1)](PF_6)

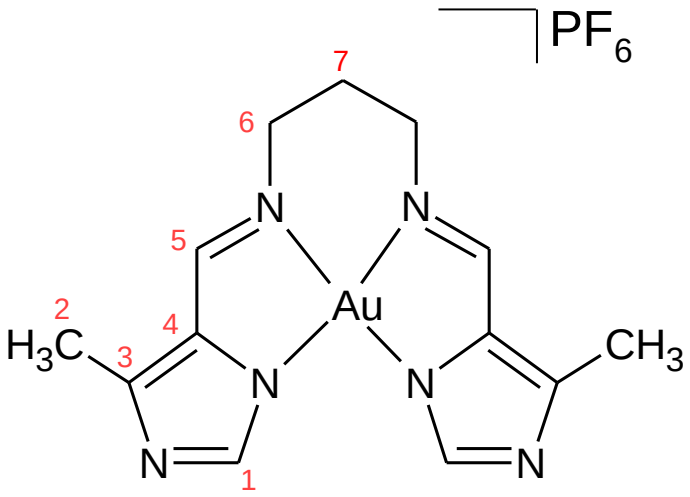

Figure 2.5.1: Structure and atom numbering scheme used for [Au(L1)](PF_6).

[Bu_4N][$AuCl_4$] (0.100 g, 0.172 mmol) was dissolved in DCM (10 mL) in a round bottom flask with two molar equivalents of [Bu_4N][PF_6] (0.133 g, 0.344 mmol). The ligand (0.0889 g, 0.344 mmol) was dissolved in ethanol (10 mL) and added to the solution of [Bu_4N][$AuCl_4$] and [Bu_4N][PF_6]. The resulting mixture was heated to reflux for 3 hours during which a mustard-coloured precipitated formed. The precipitate was isolated by gravity filtration and was washed with ethanol, yielding the final product (0.0677 g, 0.113 mmol, 65.7% yield). The product was analysed by ^1H and ^{13}C NMR, IR and UV/visible spectroscopy as well as mass spectrometry.

^1H NMR (400 MHz, DMSO-*d6*) [δ ppm]: 1.92 (m, 2H, H-7), 2.54 (s, 6H, H-2), 3.77 (t, 4H, H-6), 8.45 (s, 2H, H-1), 8.88 (s, 2H, H-5). ^{13}C NMR (100 MHz, DMSO-*d6*, 303 K) [δ ppm]: 25.62 (2), 36.65 (7), 51.99 (6), 134.59 (1), 147.69 (3), 152.65 (4), 162.23 (5); ^{31}P NMR (162 MHz, DMSO-*d6,* 303 K)[δ ppm]: -144.18 (PF_6); ^{19}F (376 MHz, DMSO-*d6,* 298K)[δ ppm]: -71.11, -69.23(PF_6). IR (cm^{-1}): 1597.51 cm^{-1} υ(C=N), 1297.39cm^{-1} υ(C-N stretch), 1448.08 cm^{-1} υ(C-C aromatic region). UV-vis (DMSO) λ_{max} [nm] (ε/ M^{-1} cm^{-1}): 270 (3.6×10^4), 339 (1.5×10^4). ESI-MS: m/z 453.1110 (M^+), calculated m/z: 453.1107 (M^+).

2.5.2 Synthesis of 5,5'-{(2,2-dimethylpropane-1,3-diyl)bis[nitrilo(*E*) methylylidene]}bis(4-methylimidazol-1-ide)gold(III) hexafluorophosphate(V) [Au(L2)](PF6)

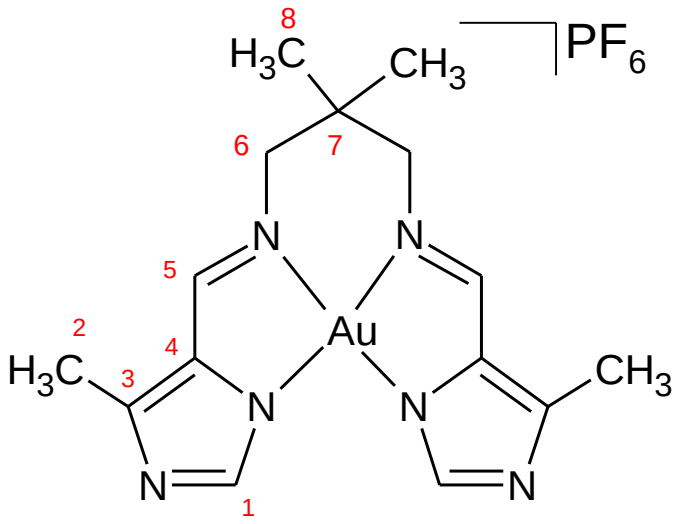

Figure 2.5.2: Structure and atom numbering scheme used for [Au(L2)](PF_6).

[Bu_4N][$AuCl_4$] (0.100g, 0.172 mmol) was dissolved in DCM (10 mL) in a round bottom flask with two molar equivalents of [Bu_4N][PF_6] (0.133 g, 0.344 mmol). The ligand (0.0985 g, 0.344 mmol) was dissolved in ethanol (10 mL) and added to the solution of [Bu_4N][$AuCl_4$] and [Bu_4N][PF_6]. The resulting solution was heated to reflux for 3 hours during which a yellow-orange precipitated formed. The precipitate was isolated by gravity filtration and washed with ethanol, yielding the final product (0.0761 g, 0.122 mmol, 70.9% yield). The product was analysed by ^{1}H and ^{13}C NMR, IR and UV/visible spectroscopy as well as mass spectrometry.

^{1}H NMR (400 MHz, DMSO-d_6, 303 K) [δ ppm]: 1.08 (s, 6H, H-8), 2.53 (s, 6H, H-2), 3.47 (s, 4H, H-6), 8.46 (s, 2H, H-1), 8.81 (s, 2H, H-5). ^{13}C NMR (100 MHz, DMSO-d_6, 303 K), [δ ppm]: 13.93 (2), 14.68 (8), 23.30 (7), 61.62 (6), 134.66 (1), 147.97 (3), 153.20 (4), 162.98 (5). ^{31}P NMR (162 MHz, DMSO-*d6,* 303 K)[δ ppm]: -144.18 (PF_6). ^{19}F (376 MHz, DMSO-*d6,* 298K) [δ ppm]: -71.11,-69.23 (PF_6). IR (cm^{-1}): 1597.30 cm^{-1} υ(C=N), 1278.13 cm^{-1} υ(C-N stretch), 1445.25 cm^{-1} υ(C-C aromatic region). UV-vis (DMSO) λ_{max} [nm] (ε/ M^{-1} cm^{-1}): 261 (1.9×10^4), 342 (2.6×10^4). ESI-MS: m/z 481.1424 (M^+), calculated m/z: 481.1419 (M^+).

2.5.3 Attempted synthesis of *N,N′*-bis[(*E*)-1*H*-imidazol-5-yl methylidene]propane-1,3-diamine gold(III) hexafluorophosphate(V) [Au(L3)](PF_6)

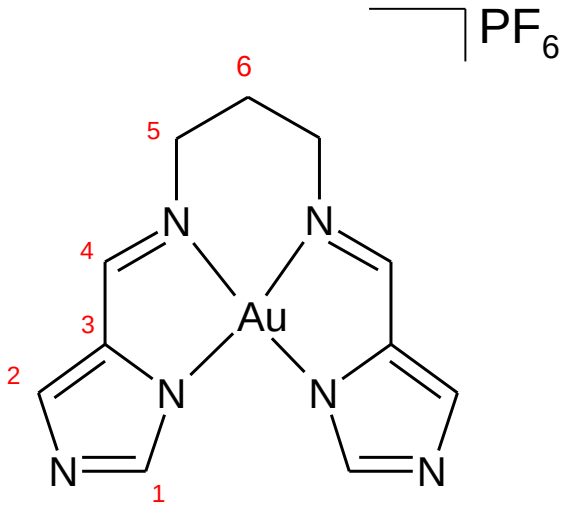

Figure 2.5.3: Structure and atom numbering scheme used for [Au(L3)](PF_6).

[Bu_4N][$AuCl_4$] (0.100g, 0.172 mmol) was dissolved in DCM (10 mL) in a round bottom flask with two molar equivalents of [Bu_4N][PF_6] (0.133 g, 0.344 mmol). The ligand (0.0792 g, 0.344 mmol) was dissolved in ethanol (10 mL) and added to the solution of [Bu_4N][$AuCl_4$] and [Bu_4N][PF_6]. The resulting solution was heated to reflux for 3 hours during which no complex formation could be detected.

2.5.4 Synthesis of 5,5'-{(2-hydroxypropane-1,3-diyl)bis[nitrilo(*E*)methylylidene]}bis(4-methylimidazol-1-ide) gold(III) hexafluorophosphate(V) [Au(L4)](PF$_6$)

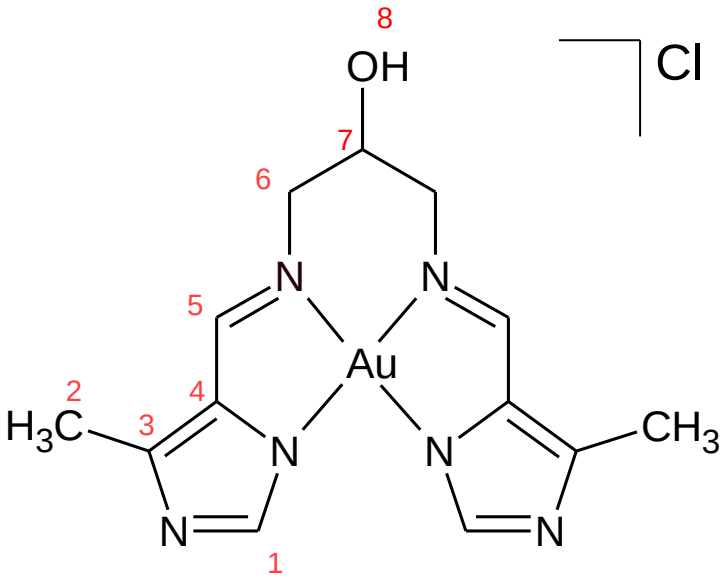

Figure 2.5.4: Structure and atom numbering scheme used for [Au(L4)](Cl).

[Bu$_4$N][AuCl$_4$] (0.100g, 0.172 mmol) was dissolved in DCM (10 mL) in a round bottom flask with two molar equivalents of [Bu$_4$N][PF$_6$] (0.133 g, 0.344 mmol). The ligand (0.0944 g, 0.344 mmol) was dissolved in ethanol (10 mL) and added to the solution of [Bu$_4$N][AuCl$_4$] and [Bu$_4$N][PF$_6$]. The resulting solution was heated to reflux for 3 hours during which a dark yellow precipitate formed. The precipitate was isolated by gravity filtration and washed with ethanol, yielding the final product (0.0517 g, 0.102 mmol, 59.3% yield). The product was analysed by ^{1}H and ^{13}C NMR, IR and UV/visible spectroscopy as well as mass spectrometry.

^{1}H NMR (400 MHz, DMSO-d$_6$, 303 K) [δ ppm]: 2.53 (s, 6H, H-2), 3.74 (dd, 2H, $^6J_1$=5.8 Hz, $^6J_2$=8.8 Hz, H-6) , 3.85 (dd, 2H, H-6), 4.48 (m, 1H, H-7), 5.79 (d, 1H, H-8), 8.44 (s, 2H, H-1), 8.94 (s, 2H, H-5). ^{13}C NMR (100 MHz, DMSO-d$_6$, 303 K), [δ ppm]: 14.60 (2), 56.14 (7), 68.60 (6), 134.75 (1), 148.01 (3), 152.97 (4), 163.51 (5). IR (cm^{-1}): 1598.44 cm^{-1} υ(C=N), 1282.79 cm^{-1} υ(C-N stretch), 1440.11 cm^{-1} υ(C-C aromatic region). UV-vis (DMSO) λ_{max} [nm] (ε/ M^{-1} cm^{-1}): 265 (2.6×10^4), 339(2.1×10^4). ESI-MS: m/z 469.1050 (M$^+$), calculated m/z: 469.1056 (M$^+$).

2.5.5 Attempted synthesis of 5,5'-{butane-1,4-diylbis[nitrilo(*E*)methylylidene]}bis(4-methylimidazol-1-ide) gold(III) hexafluorophosphate(V) [Au(L5)](PF_6)

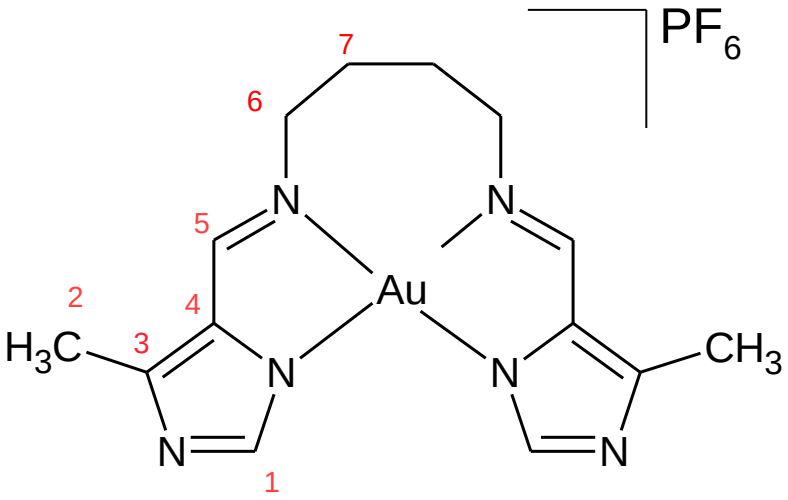

Figure 2.5.5: Structure and atom numbering scheme used for [Au (L5)](PF_6).

[Bu_4N][$AuCl_4$] (0.100g, 0.172 mmol) was dissolved in DCM (10 mL) in a round bottom flask with two molar equivalents of [Bu_4N][PF_6] (0.133 g, 0.344 mmol). The ligand (0.0937 g, 0.344 mmol) was dissolved in ethanol (10 mL) and added to the solution of [Bu_4N][$AuCl_4$] and [Bu_4N][PF_6]. The resulting solution was heated to reflux for 3 hours during which no complex formation could be detected.

2.5.6 Attempted Synthesis of 5,5'-{(1*S*,2*S*)-cyclohexane-1,2-diylbis[nitrilo(*E*)methylylidene]}bis(4-methylimidazol-1-ide) gold(III) hexafluorophosphate(V)[Au(L6)](PF_6)

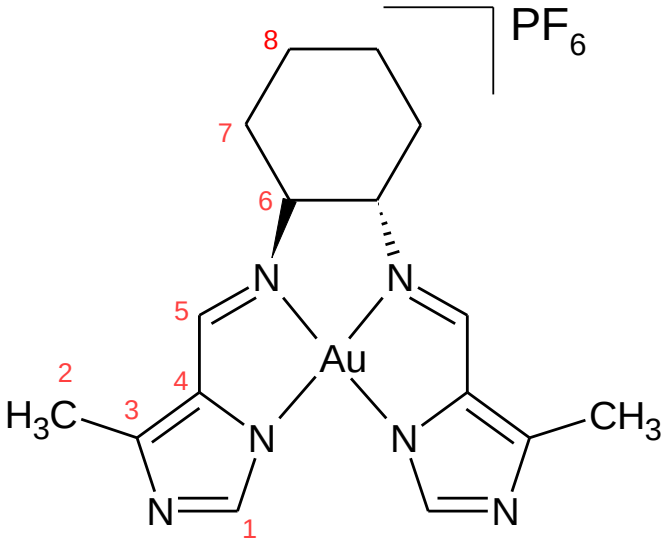

Figure 2.5.6: Structure and atom numbering scheme used for [Au(L6)](PF_6).

[Bu_4N][$AuCl_4$] (0.100g, 0.172 mmol) was dissolved in DCM (10 mL) in a round bottom flask with two molar equivalents of [Bu_4N][PF_6] (0.133 g, 0.344 mmol). The ligand (0.103 g, 0.344 mmol) was dissolved in ethanol (10 mL) and added to the solution of [Bu_4N][$AuCl_4$] and [Bu_4N][PF_6]. The resulting solution was heated to reflux for 3 hours during which no complex formation could be detected.

2.5.7 Attempted synthesis of 5,5'-{(1*R*,2*R*)-cyclohexane-1,2-diylbis[nitrilo(*E*)methylylidene]}bis(4-methylimidazol-1-ide) gold(III) hexafluorophosphate(V) [Au(L4)](PF_6)

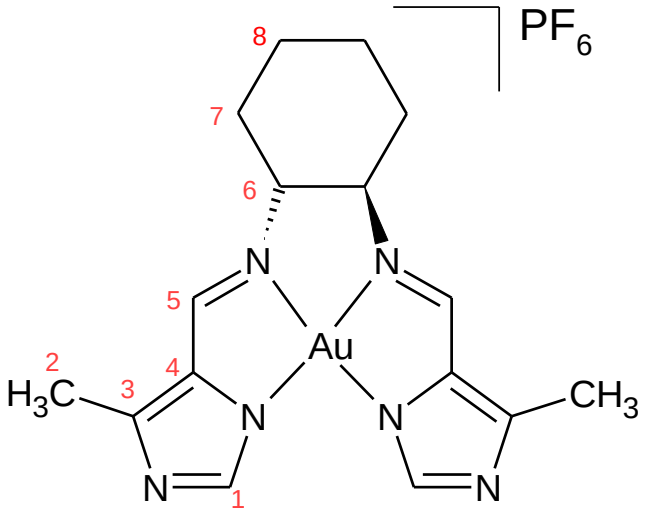

Figure 2.5.7: Structure and atom numbering scheme used for [Au(L7)](PF_6).

[Bu_4N][$AuCl_4$] (0.100g, 0.172 mmol) was dissolved in DCM (10 mL) in a round bottom flask with two molar equivalents of [Bu_4N][PF_6] (0.133 g, 0.344 mmol). The ligand (0.103 g, 0.344 mmol) was dissolved in ethanol (10 mL) and added to the solution of [Bu_4N][$AuCl_4$] and [Bu_4N][PF_6]. The resulting solution was heated to reflux for 3 hours during which no complex formation could be detected.

2.5.8 Attempted synthesis of 5,5'-{(2,2-dimethylethane-1,3-diyl)bis[nitrilo(*E*) methylylidene]}bis(4-methylimidazol-1-ide)gold(III) hexafluorophosphate(V) [Au(L8)](PF_6)

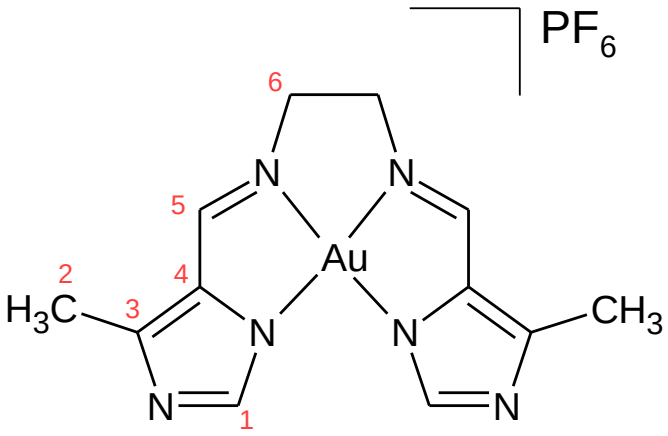

Figure 2.5.8: Structure and atom numbering scheme used for [Au(L8)](PF_6).

[Bu_4N][$AuCl_4$] (0.100g, 0.172 mmol) was dissolved in DCM (10 mL) in a round bottom flask with two molar equivalents of [Bu_4N][PF_6] (0.133 g, 0.344 mmol). The ligand (0.0840 g, 0.344 mmol) was dissolved in ethanol (10 mL) and added to the solution of [Bu_4N][$AuCl_4$] and [Bu_4N][PF_6]. The resulting solution was heated to reflux for 3 hours during which no complex formation could be detected.

2.5.9 Synthesis of 5,5'-{(2-ethoxypropane-1,3-diyl)bis[nitrilo(E)methylylidene]}bis(4-methylimidazol-1-ide) gold(III) hexafluorophosphate(V) [Au(L9)]Cl

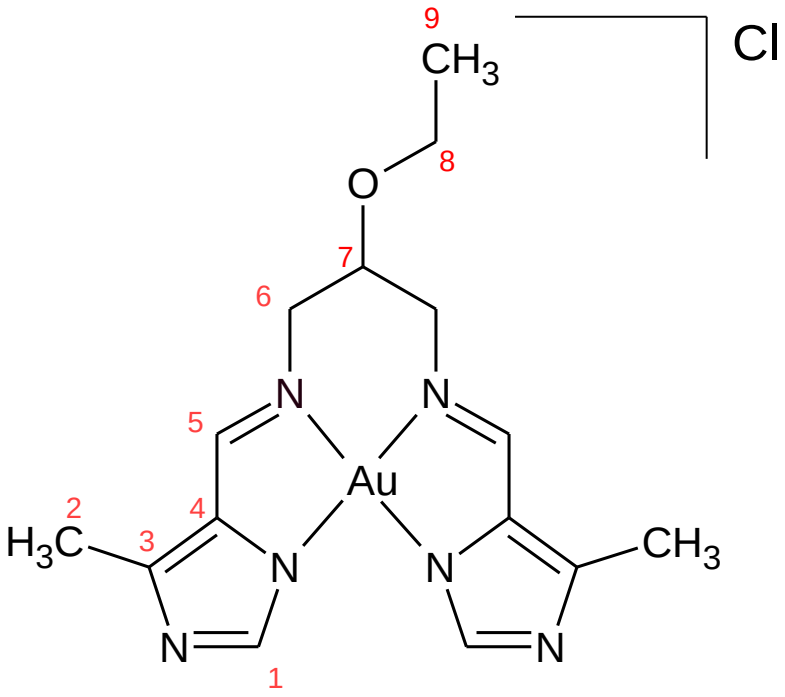

Figure 2.5.9: Structure and atom numbering scheme used for [Au(L9)](Cl).

$[Bu_4N][AuCl_4]$ (0.100g, 0.172 mmol) was dissolved in DCM (10 mL) in a round bottom flask with two molar equivalents of $[Bu_4N][PF_6]$ (0.133 g, 0.344 mmol). The ligand (0.104 g, 0.344 mmol) was dissolved in ethanol (10 mL) and the ligand solution added to the $[Bu_4N][AuCl_4]$ and $[Bu_4N][PF_6]$ mixture. The resulting solution was heated to reflux for 3 hours during which the solution turned yellow-orange. The solvent volume was reduced by rotary evaporation yielding an orange precipitate. The precipitate was isolated by gravity filtration and washed with THF (0.0125 g, 0.023 mmol, 13.4%). The product was analysed by ^{1}H and ^{13}C NMR, IR and UV/visible spectroscopy as well as mass spectrometry.

^{1}H NMR (400 MHz, DMSO-d_6 , 303 K) [δ ppm]: 1.10 (t, 3H, H-9), 2.54 (s, 6H, H-2), 3.57 (m, 2H, H-8), 3.95 (d, 4H, H-6), 4.37 (m, 1H, H-7), 8.44 (s, 2H, H-1), 8.95 (s, 2H, H-5). ^{13}C NMR (100 MHz, DMSO-d_6, 303 K), [δ ppm]: 14.60 (2), 15.60 (9), 53.27 (8), 63.97 (7), 75.16 (6), 134.59 (1), 148.01 (3), 152.97 (4), 163.19 (5). IR (cm^{-1}): 1597.49 cm^{-1} υ(C=N), 1295.02 cm^{-1} υ(C-N stretch), 1350.17 cm^{-1} υ(C-C aromatic region). UV-vis (DMSO) λ_{max} [nm] (ε/ M^{-1} cm^{-1}): 267 (2.82×10^4), 331 (1.1×10^4). ESI-MS: m/z 497.1347 (M^+), calculated m/z: 497.1369 (M^+).

2.5.10 Synthesis 5,5'-{(2-methoxypropane-1,3-diyl)bis[nitrilo(E)methylylidene]}bis(4-methylimidazol-1-ide) gold(III) hexafluorophosphate(V) [Au(L10)][PF_6]

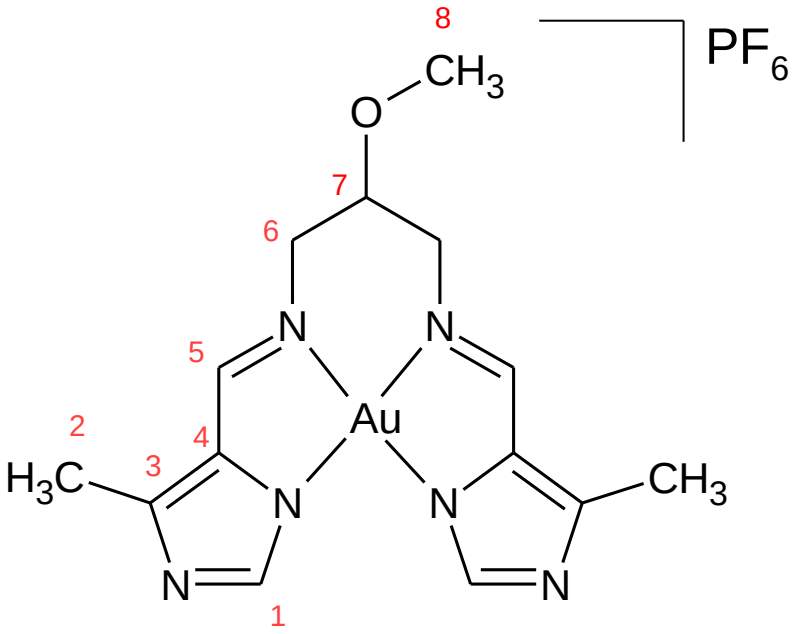

Figure 2.5.10: Structure and atom numbering scheme used for [Au(L10)](PF_6).

[Bu_4N][$AuCl_4$] (0.100g, 0.172 mmol) was dissolved in DCM (10 mL) in a round bottom flask with two molar equivalents of [Bu_4N][PF_6] (0.133 g, 0.344 mmol). The ligand (0.0991 g, 0.344 mmol) was dissolved in ethanol (10 mL) and the ligand solution added to the [Bu_4N][$AuCl_4$] and [Bu_4N][PF_6] mixture. The resulting solution was heated to reflux for 3 hours during which a yellow-orange precipitated formed. The precipitate was isolated by gravity filtration and washed with ethanol, yielding the final product (0.759 g, 0.121 mmol, 70.3% yield). The product was analysed by ^{1}H and ^{13}C NMR, IR and UV/visible spectroscopy as well as mass spectrometry.

^{1}H NMR (400 MHz, DMSO-d_6, 303 K) [δ ppm]: 2.54 (s, 6H, H-2), 3.36 (s, 3H, H-8), 4.03 (d, 4H, H-6), 4.26 (m, 1H, H-7), 8.45 (s, 2H, H-1), 8.93 (s, 2H, H-5). ^{13}C NMR (100 MHz, DMSO-d_6, 298 K), [δ ppm]: 14.71 (2), 52.69 (6), 56.71(8), 76.84 (7), 134.41 (1), 148.06 (3), 153.14 (4), 163.46 (5). ^{31}P NMR (162 MHz, DMSO-*d6*, 303 K) [δ ppm]: -144.18 (PF_6). ^{19}F (376 MHz, DMSO-*d6*, 303 K)[δ ppm]:- 71.11,-69.23 (PF_6). IR (cm^{-1}): 1598.02 cm^{-1} υ(C=N), 1291.14 cm^{-1} υ(C-N stretch), 1410.96 cm^{-1} υ(C-C aromatic region). UV-vis (DMSO) λ_{max} [nm] (ε/ M^{-1} cm^{-1}): 267 (2.54×10^4), 340 (5.1×10^3). ESI-MS: m/z 483.1226 (M^+), calculated m/z: 483.1212 (M^+).

Chapter 3| Synthesis

3.1 Introduction

Schiff Base ligands were chosen to help stabilise the gold(III) ion in this research. These Schiff base ligands were synthesized via a condensation reaction between a carbonyl and primary amine. This reaction was first discovered by Hugo Schiff in 1864 [1]. The general mechanism for the synthesis of a Schiff base is shown in Scheme 3.1. The synthesis actually occurs in three steps: firstly the lone pair of electrons on the nitrogen atom attacks the carbonyl carbon forming a bond between the nitrogen and carbon. The positively charged nitrogen loses one hydrogen, which bonds to the negatively charged oxygen forming an OH group boned to the "carbonyl" carbon. Finally, the OH group and the remaining hydrogen on the nitrogen leave as water and the Schiff base is formed. The lone pair of electrons on the nitrogen atom of the imine bond make it an ideal donor atom for coordination to various metal ions.

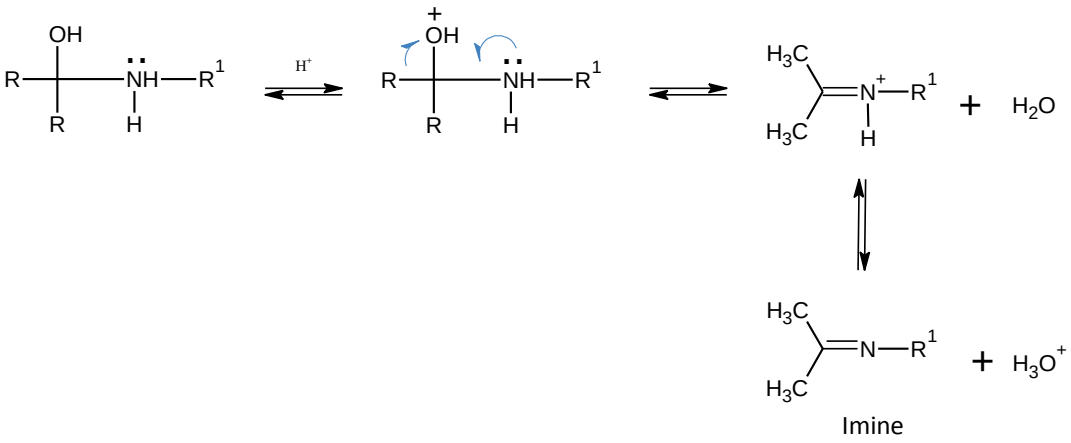

Scheme 3.1: General mechanism for a Schiff base reaction. [2]

These Schiff base ligands have been successfully coordinated to gold(III) as they are effective sigma-donor groups able to stabilise the metal in its high oxidation state. The aim of my project was to synthesise a range of bis(imidazole-imine) ligands and coordinate them to gold(III) to form novel metal-based chemotherapeutic agents. This high oxidation state of gold(III) is potentially unstable in the presence of biological reducing agents such as glutathione thus strong sigma-donor ligands are required for stability. The ligands will be dianionic when the imidazole NH is deprotonated. Coordination of these dianionic ligands to the gold(III) ion will

yield a monocationic complex. The addition of a methyl group at the 4- position on the imidazole ring would have an inductive effect making the deprotonated nitrogen atoms stronger sigma donors thus stabilizing the complexes more effectively. The ligands and complexes are mainly varied by the structures of the di(azomethine) linkage, by adjusting the structure of this group the solubility profile (i.e. the lipophilicity) can be tuned. The ability of the complex to cross the phospholipid bilayer and reach its intended cellular target (DNA) can therefore be optimised.

3.2 Synthesis of the Schiff Base Ligand

3.2.1 Synthesis of H2L1- H2L8

The synthesis of these ligands involved a simple condensation reaction between an imidazole carboxaldehyde and the respective diamine. The general synthesis is shown in Scheme 3.2.1 below.

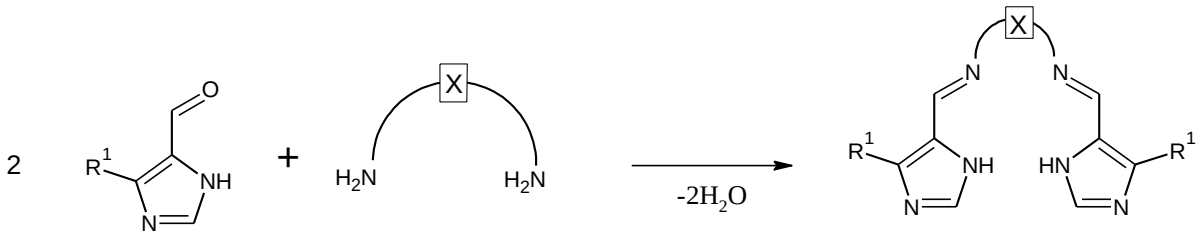

Ligand	R^1	X
H_2L1	CH_3	$CH_2CH_3CH_2$
H_2L2	CH_3	$CH_2CH_2(CH_3CH_3)CH_2$
H_2L3	H	$CH_2CH_3CH_2$
H_2L4	CH_3	$CH_2CH_2(OH)CH_2$
H_2L5	CH_3	$CH_2CH_2CH_2CH_2$
H_2L6	CH_3	*R,R*-cyclohexyl
H_2L7	CH_3	*S,S*-cyclohexyl
H_2L8	CH_3	CH_2CH_2

Scheme 3.2.1: Condensation reaction for the synthesis of H_2L1-H_2L8.

The above reactions all involve the condensation of an aldehyde with a primary alkyl amine. The structure of the alkyl amine bridging unit did not have any notable influence on the efficiency of the reaction and a single method was therefore applied in the synthesis of H_2L1 - H_2L8.

3.2.2 Synthesis of H_2L9 and H_2L10

For the synthesis of ligand H_2L9 and H_2L10 the ethoxy bridging unit and methoxy bridging unit respectively had to be synthesised from 1,3-diamino-2-propanol. The hydroxyl group on the second carbon can be easily derivatised. Before the hydroxyl group can be converted, the primary amines need to be protected with di-*tert*-butyl dicarbonate (Boc_2O) as primary amines (pK_a= 10-11) are more reactive than alcohols (pK_a=16.5) [3]. Scheme 3.2.2 below shows the conversion of the primary amines to amides resulting in them being less nucleophilic and thus less reactive.

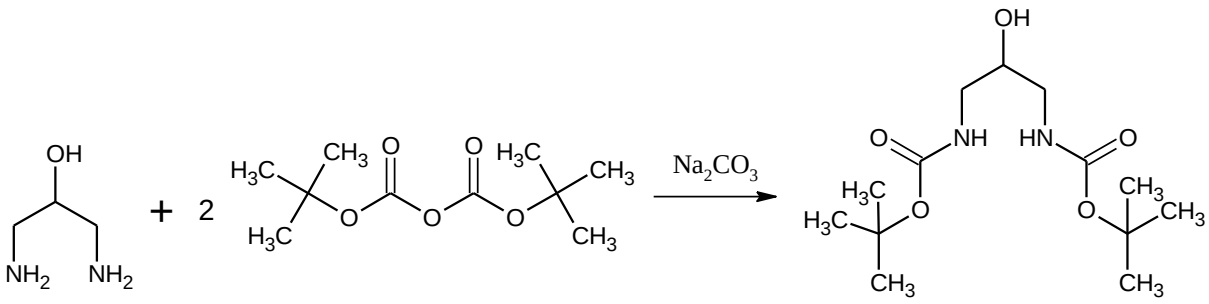

Scheme: 3.2.2: The protection of primary amines using di-*tert*-butyl dicarbonate.

The newly formed amine bond formed exhibits resonance. In the resonance form the amine is deprotonated making it unreactive. Scheme 3.2.3 below illustrates the resonance forms.

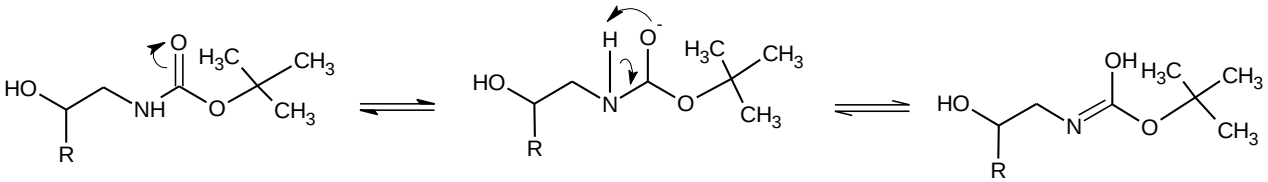

Scheme: 3.2.3: The different resonance forms of the protected diamine.

After protection, the hydroxyl group is converted to an ether with the addition of an alkyl iodide in the presence of $[Bu_4N][HSO_4]$ and 50% NaOH. The hydroxyl group is deprotonated leading to an S_N2 type reaction with the alkyl halide resulting in the formation of the ethoxy and methoxy groups. The $[Bu_4N][HSO_4]$ acts as a phase transfer catalyst in the biphasic reaction mixture. It

carries hydroxide ions from the aqueous to the organic layer allowing deprotonation of the lipophilic protected amine. Scheme 3.2.4 below shows the S_N2 type reaction.

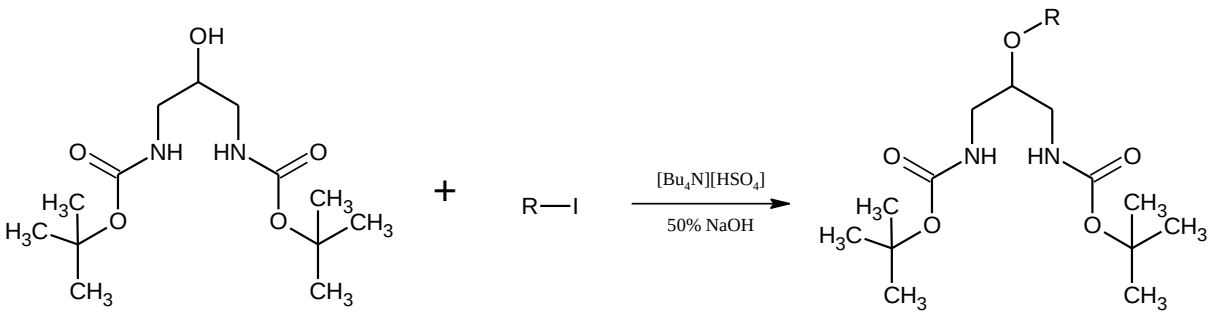

Scheme 3.2.4: S_N2 type reaction of the hydroxyl group.

After the formation of the ether the amines are deprotected by the addition of excess HCl. This results in the formation of a hydrochloride salt. Scheme 3.2.8 illustrates the synthesis of the hydrochloride salt.

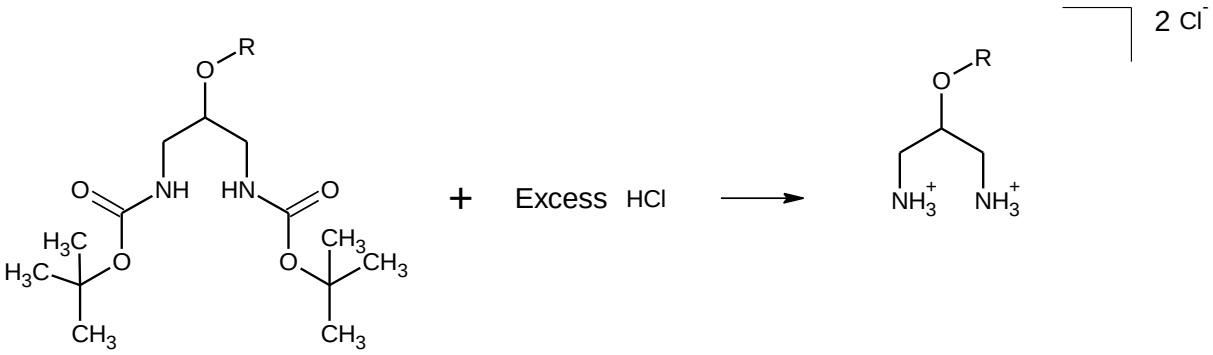

Scheme 3.2.5: Deprotection reaction to form hydrochloride salt.

The acidity of the hydrochloride salt was found to hinder the condensation reaction therefore 2-ethoxy-1,3-diamino-2-propane was synthesised *via* a solid state reaction by grinding 2-ethoxy-1,3-diamino-2-propane dihydrochloride and sodium carbonate in an agate pestle and mortar. Once the 2-ethoxy-1,3-diamino-2-propane was formed 4-methyl-1H-imidazole-5-carbaldehyde was added to the mortar and the two were ground together in the presence of piperidine which was used as a catalyst. The solid-state method proved to be very effective with high yields and short reaction times. The method also conforms to modern green chemistry practices by minimising the amount of solvent used in the reaction and work-up [10].

3.3 Metallation of Schiff Base Ligands

3.3.1 Gold(III) salts

As a source of gold(III) ions, the tetra-butylammonium tetrachloroaurate ($[Bu_4N][AuCl_4]$) was used. Although $Na[AuCl_4]$, $H[AuCl_4]$ are also viable sources of gold(III) ions [4][5], they have been associated with the formation of unwanted $[AuCl_4]^-$ or $[AuCl_2]^-$ counter ions when isolating cationic metal chelates. The drawbacks of these gold-based anions are that it leads to a poor aqueous solubility, making characterization difficult. Secondly if a gold counter ion is formed only half of the moles of gold go towards forming the complex. $H[AuCl_4]$ has been reported as an efficient source of gold(III) ions for chelation by N-donor ligands. This is dependent on the nature of the N-donor ligands as some research states that the salt is favoured as it lowers the pH of the solution which aids the chelation. In some cases where ligand deprotonation is required, the lower pH hinders this process preventing metal chelation [5][6][7][8].

Previous reactions have attempted to use $Na[AuCl_4]$ or $H[AuCl_4]$ as a gold(III) ion source at varying temperatures. The reactions were unsuccessful resulting in black precipitate (Au_2O_3) or colloidal gold [9].

Barnholtz *et al.* concluded that $[Bu_4N][AuCl_4]$ is the most effective gold salt from the three mentioned. For a successful reaction with the $[Bu_4N][AuCl_4]$ salt it requires the presence of a hexafluorophosphate(V) salt and ethanol. If one of the two are not present the reaction fails. The reagents seem to pay a role in breaking the $[Bu_4N][AuCl_4]$ ion pair[5].

An added advantage of using $[Bu_4N][AuCl_4]$ is that it is lipophilic and dissolves in non-polar organic solvents, whereas the target cationic gold(III) chelates are soluble in polar organic solvents therefore the gold chelates precipitate out of solution simplifying the required reaction workup.

3.3.2 Metallation of H_2L1, H_2L2 and H_2L10

Metallation of free ligands H_2L1, H_2L2 and H_2L10 were successful using $[Bu_4N][AuCl_4]$. The ligand was dissolved in ethanol while the $[Bu_4N][AuCl_4]$ was dissolved in DCM. The two solutions were added and the relative complex precipitated out of solution. The three resulting complexes contain a PF_6^- counter ion. Scheme 3.3.2.1 shows the general metalation of ligands H_2L1, H_2L2 and H_2L10.

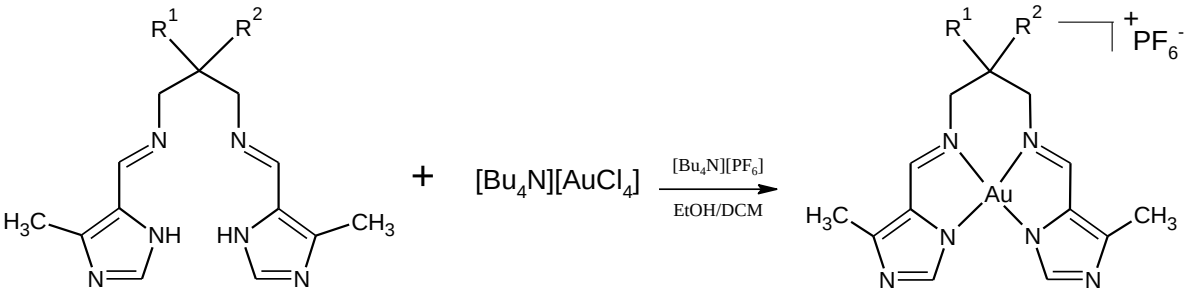

Scheme 3.3.1: General reaction outline for metalation of ligands H_2L1, H_2L2 and H_2L10.

Table 3.3.1: Summary of R groups of different ligands.

Ligand	R^1	R^2
AuL1	H	H
AuL2	CH_3	CH_3
AuL10	H	OCH_3

3.3.3 Metallation of H_2L4 and H_2L9

Metallation of free ligands H_2L4 and H_2L9 were successful using $[Bu_4N][AuCl_4]$. The ligand was dissolved in ethanol while the $[Bu_4N][AuCl_4]$ was dissolved in DCM. Complex $[Au(L4)Cl^-]$ precipitated out of solution while $[Au(L9)Cl^-]$ remained in solution. The solution containing $[Au(L9)Cl^-]$ had the solvent removed *via* rotary evaporation and was washed with THF. Both these complexes have a Cl^- counter ion also $[Bu_4N][PF_6]$ was added to the reaction. Scheme 3.3.3.1 shows the general metalation of ligands H_2L4 and H_2L9.

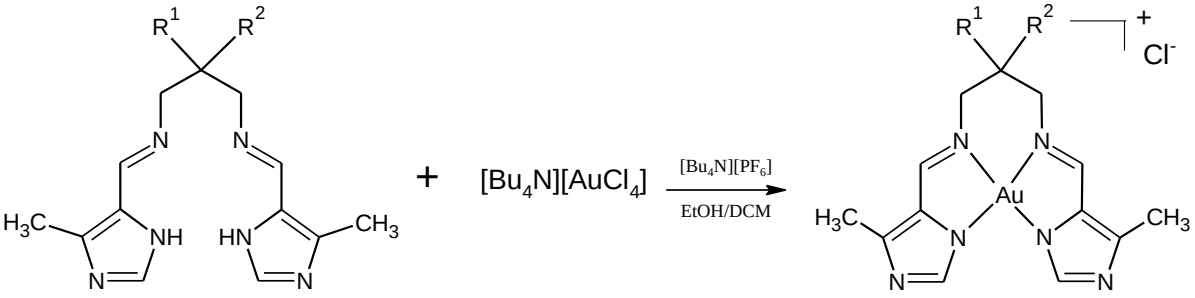

Scheme 3.3.2: General reaction outline for metalation of ligands H_2L4 and H_2L9.

Table 3.3.2: Summary of R groups of different ligands.

Ligand	R^1	R^2
AuL4	H	OH
AuL9	H	OCH_2CH_3

3.3.4 Metallation of H_2L3, H_2L5, H_2L6, H_2L7 and H_2L8

Metalation of ligands H_2L3, H_2L5, H_2L6, H_2L7 and H_2L8 was unsuccessful using the above method. The reaction was carried out with 2 molar equivalents of ligand, but no metal ion chelation could be detected.. The possible reason for the failure of the metallation is the two-carbon bridging units creating a small coordination site for the large gold(III) ion. Considering that all the ligands which have a three carbon bridging unit easily coordinated the gold(III) ion it can be concluded that for this system a three-carbon bridge leading to two five-membered and a six-membered chelation rings is ideal.

In conclusion, seven novel Schiff base ligands and five novel gold(III) Shiff base chelates were successfully synthesized. The ligand synthesis gave consistently good yields and the metallation reactions resulted in decent yields except in AuL9 where the yield was low due to the complex being soluble in the solution.

3.4 References

1. Schiff, H. *Annalen* **1864**, *131*, 118.
2. Xavier, A.; Srividhya, N. Synthesis And Study Of Schiff Base Ligands. *J. Appl. Chem.,* 2014, 7, 06-15.
3. March, J. *Advanced Organic Chemistry*; Wiley-Interscience.
4. Block, B. P., Bailer, J. C. *J. Am. Chem. Soc* **1951**, *73*, 4722.
5. Best, S. L., Chattopadhyay, T. K., Djuran, M. I., Palmer, R. A., Sadler, P. J., Sóvágó, I., Varnagy, K. *Dalton Trans.* **1997**, 2587.
6. Barnholtz, S. L., Lydon, J. D., Huang, G., Venkatesh, M., Barnes, C. L., Ketring, A. R., Jurisson, S. S. *Inorg. Chem.* **2001**, *40*, 972.
7. Bourrosh, P., Bologa, O., Simonov, Y., Gerbeleu, N., Lipkowski, J., Gdaniec, M. *Inorg. Chim. Acta* **2006**, *359*, 721.
8. Suh, M. P., Kim, I. S., Shim, B. Y., Hong, D., Yoon, T.-S. *Inorg. Chem.* **1996**, *35*, 3595.
9. Akerman, M. P., University of KwaZulu Natal, 2011.
10. Farhanullah, Kang, T., Yoon, E., Choi, E., Kim, S. and Lee, J. (2009). 2-[2-Substituted-3-(3,4-dichlorobenzylamino)propylamino]-1H-quinolin-4-ones as Staphylococcus aureus methionyl-tRNA synthetase inhibitors. Eur. J.Med. Chem., 44(1), pp.239-250.

Chapter 4| Spectroscopy

4.1 Infrared spectroscopy

4.1.1 Introduction

The bonds in molecules are continuously stretching and bending. Stretching occurs along the bond line while bending changes the bond angle [1]. Molecules that have covalent bonds have the ability to absorb light in the infrared region (700 mm – 1 mm). The region of greatest interest is 2500 nm – 25000 nm (400 to 4000 cm^{-1}) which is the region for vibrational transitions. The molecule absorbs the infrared radiation which results in transitions between the vibrational and ground state energy levels. These transitions are presented as an IR spectrum [1].

The total energy of a molecule comprises the movement of electrons in the molecules, the vibrations of each atom in the molecule and rotation of the molecule. Analysis can be performed by measuring absorption, emission and reflection. This technique is used to determine the functional groups present in the compound as different functional groups vibrate at different stretching frequencies (wavenumbers). In general, stronger bonds (i.e. higher bond orders) vibrate at higher wavenumbers [2].

One of the key stretching frequencies that will confirm a successful Schiff base condensation is the imine C=N stretch. This bond will typically have a stretching frequency in the region of 1680 cm^{-1}.

4.1.2 Results and discussion

The most significant band in the IR spectrum of a Schiff base ligand is the imine (C=N) group which is found in the range of 1690 – 1640 cm^{-1} [1]. When chelated to the gold(III) ion there is a considerable spectral shift to lower wavenumbers of the imine C=N stretching frequency. This is due to the strongly electron withdrawing metal ion removing electron density from the coordinated imine nitrogen atom and weakening the double bond. The imine stretching frequencies of the imine groups for the free ligands and gold(III) chelated ligands are summarised in Table 4.1.1.

Table 4.1.1: Imine stretching frequencies of the free ligands and gold(III) chelates.

Schiff base	**Free Ligand (cm^{-1})**	**Gold(III) Chelate (cm^{-1})**
H_2L1	1645	1597
H_2L2	1646	1597
H_2L3	1648	N/A
H_2L4	1648	1598
H_2L5	1645	N/A
H_2L6	1634	N/A
H_2L7	1645	N/A
H_2L8	1635	N/A
H_2L9	1646	1597
H_2L10	1645	1598

The data in Table 4.1.1 clearly show that the imine stretching frequencies of the free ligands are higher than those of the gold(III) chelates. The decrease in stretching frequency is due to the electron density moving from the ligand to the gold(III) ion. The data summarised in Table 4.1.1 also show that all the ligands have similar imine stretching frequencies. This suggests that the substitution on the alkyl bridging unit has little influence on the vibrational energy of the relatively remote imine bond.

The frequency of an NH stretching band is typically in the region of 3500-3300 cm^{-1}, but the NH bands observed herein are at lower frequencies [3]. This is likely due to hydrogen bonding between the imidazole NH and imine nitrogen atom (*vida infra*). This hydrogen bonding motif is illustrated in Chapter 5 and is a common feature of imidazole- and pyrrole-based Schiff base ligands. This electrostatic intermolecular interaction results in a lower force constant for the pyrrole NH, therefore lowering the vibrational frequency. Table 4.1.2 summarises the NH stretching frequencies for each free ligand. This band is not evident in the IR spectra of the gold(III) chelates, indicating deprotonation of the imidazole NH upon metal ion chelation.

Table 4.1.2: Imdazole NH stretching frequencies for the free ligands.

Schiff Base Ligand	**(NH, imidazole)/cm^{-1}**
H_2L1	2932
H_2L2	2807
H_2L3	2832
H_2L4	2848
H_2L5	2857
H_2L6	2848
H_2L7	2853
H_2L8	2841
H_2L9	2857
H_2L10	2857

Ligand H_2L4 and complex [Au(L4)](PF_6) have OH stretching frequencies at 3587 and 3365 cm^{-1}, respectively. These values correlate with typical OH stretches [13]. There are also C-O stretching frequencies for H_2L4 and [Au(L4)](PF_6) found at 987 and 970 cm^{-1}, respectively.

The IR spectra of the ligands differ from those of the complexes in two key ways. The first is the absence of the pyrrole NH peak in the complexes, which indicates chelation and secondly the decreasing of the C=N stretching frequencies upon chelation. The IR spectra for the metal chelates with the PF_6 anion also have a strong band at 826 nm which correlates to the P-F stretch [18]. The vibrational frequencies of these key functional groups are illustrated in Figures 4.1.1 and 4.1.2 which show the IR spectra of the H_2L2 and [Au((L2)](PF_6), respectively as representative examples.

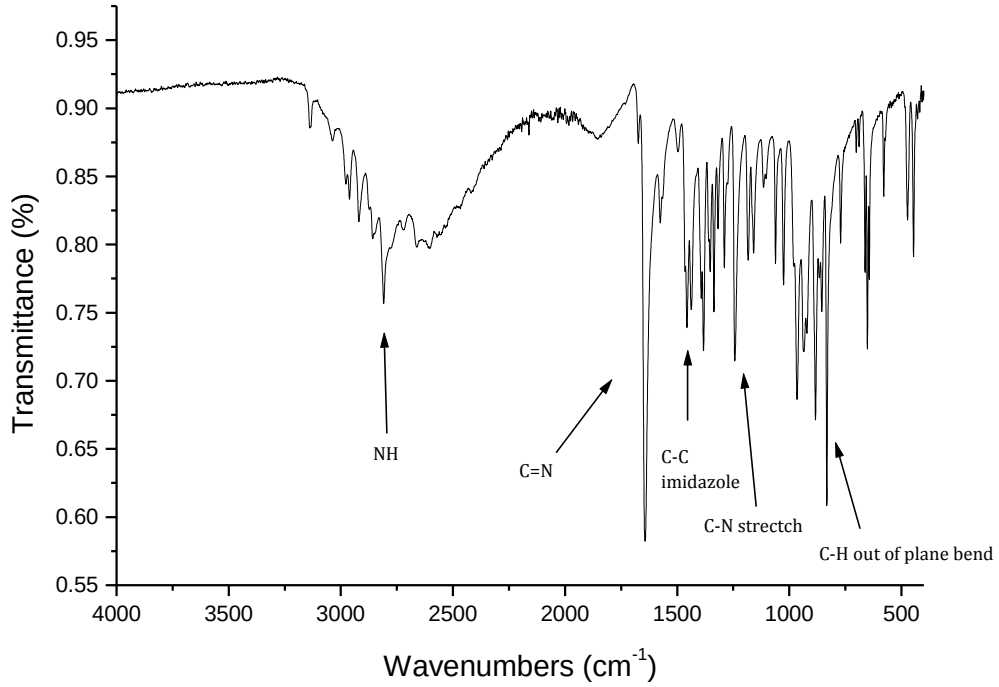

Figure 4.1.1: IR spectrum of ligand H_2L2.

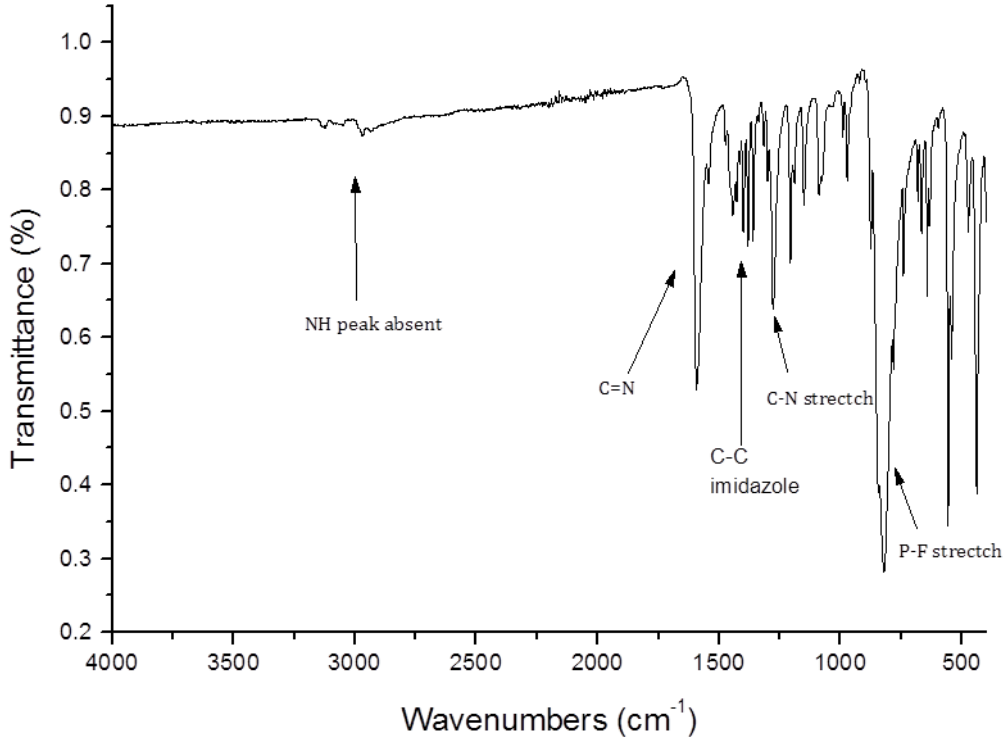

Figure 4.1.2: IR spectrum of complex $[Au(L2)](PF_6)$.

4.2 UV/visible spectroscopy

4.2.1 Introduction

The energy of ultraviolet and visible light (200 nm-800 nm) is sufficient to cause an electronic transition within a molecule. Depending on the amount of energy needed for the transition either ultraviolet or visible light will be absorbed [1].

When a molecule is in its ground state, all electrons are in the lowest energy molecular orbitals. When the molecule absorbs a photon of light the electrons move to a higher energy molecular orbital, the electron is now excited. This is called an electronic transition. Figure 4.2.1 illustrates the different transitions possible for an electron.

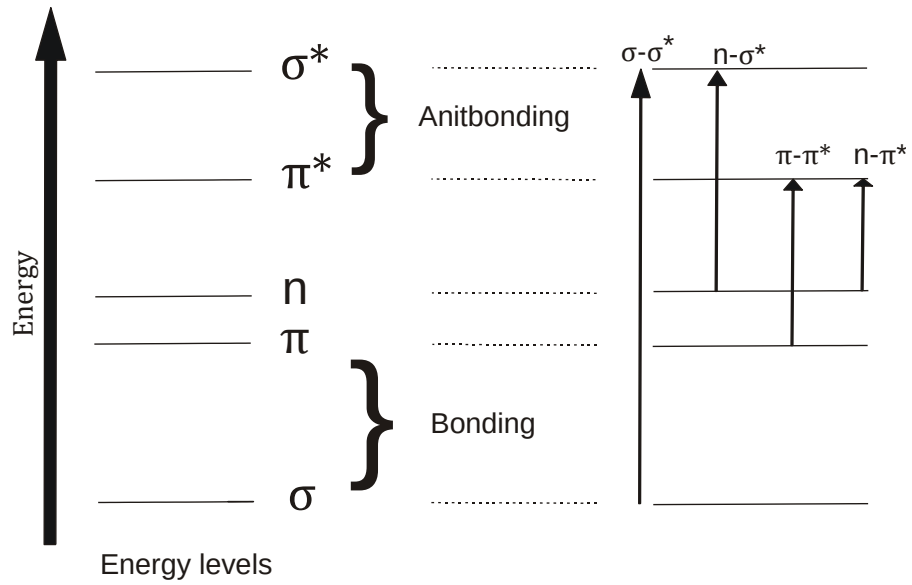

Figure 4.2.1: Diagram showing possible electronic transitions [2].

Using a UV/visible spectrophotometer the transmittance can be measured which is the fraction of original light passing through the sample. The absorbance can be calculated using:

$$A = \log\left(\frac{I_o}{I}\right) = -\log T \ldots (1)$$

In the above equation A is absorbance, I_o is intensity of applied energy, I is the resultant energy after passing through the sample and T is the percentage transmittance [4].

All free aromatic ligands will exhibit an intense π-π* transition and a much weaker n-π* transition. Both these transitions will fall into the range of 270-320 nm [5][6]. When the free ligands are chelated to the gold(III) ion there will be a new absorption band expected in the region of 400-450 nm [6]. This new band is common for square planar metal complexes of late transition metal ions, and are ligand to metal charge transfer (LMCT) bands. Due to the high oxidation state of the gold(III) ion metal-to-ligand charge transfer (MLCT) is not possible [5].

4.2.2 Results and discussion

Figures 4.2.2 and 4.2.3 show the UV/visible spectra of H_2L2 and $[Au(L2)](PF_6)$ as representative examples of the free ligands and gold(III) chelates reported herein.

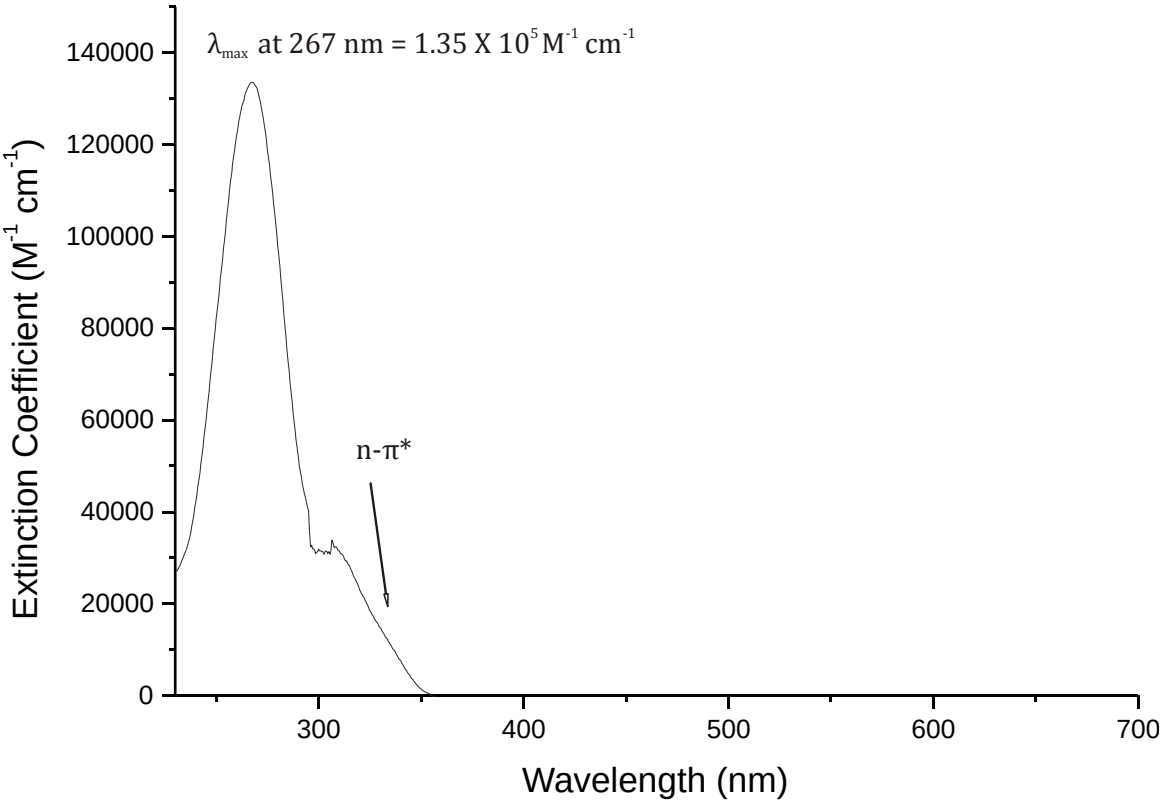

Figure 4.2.2: Electronic spectrum of H_2L2 in methanol showing a π-π* transition. An n-π * transition is evident as a shoulder at approximately 306 nm.

Figure 4.2.2 shows a single peak at 267 nm. This peak corresponds to the π-π* transition characteristic of the free ligands; a result of their extended conjugation. This peak is typical for Schiff base ligands both when chelated to metals and as free ligands. Although the π-π* transition peak dominates the spectrum there is a second electronic band present as a shoulder

of the main band. This is the n-π* transition. This transition, seen at 306 nm, is significantly less intense than the π-π* transition and is responsible for the pale yellow appearance of the compound in solution.

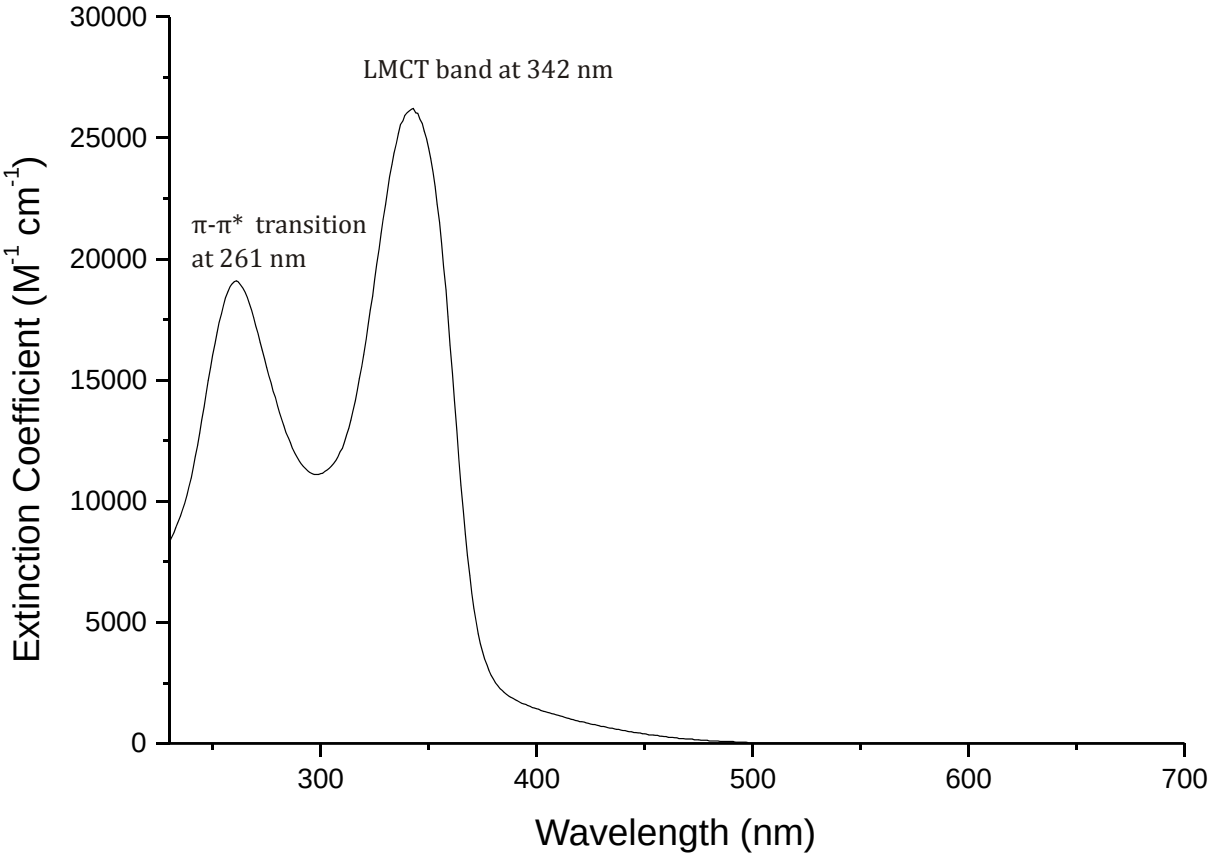

Figure 4.2.3: Electronic spectrum of [Au(L2)](PF_6) in DMSO showing an LMCT and π-π* transition.

The UV/vis spectrum of [Au(L2)](PF_6) shows two peaks. The first transition is at 261 nm and is the π-π* transition as noted in the ligand, but it has a small bathochromatic shift when compared to the free ligand. The second peak is found at 342 nm and is due to the chelation of the gold(III) ion by the free ligand. The transition involves the transfer of electrons between the ligand and gold(III) metal centre : ligand-to-metal charge transfer (LMCT). Since the gold ion is in a high oxidation state metal-to-ligand charge transfer is not possible. The symmetry of the orbitals involved in the LMCT band is discussed in Chapter 6.

A summary of the extinction coefficents of the free ligands and gold(III) chelates is shown in Table 4.2.1.

Table 4.2.1: Extinction Coefficients for the free ligands and gold(III) chelates.

Free Ligand	λ (nm)	Extinction Coefficient (M^{-1} cm^{-1})	Gold(III) Chelate	λ (nm)	Extinction Coefficient (M^{-1} cm^{-1})	
H_2L1	266	2.01×10^4	[Au(L1)](PF_6)	270, 339	3.59×10^4	1.47×10^4
H_2L2	267	1.35×10^5	[Au(L2)](PF_6)	261, 342	1.91×10^4	2.62×10^4
H_2L3	274	9.00×10^4	[Au(L3)](PF_6)	N/A	N/A	N/A
H_2L4	268	1.37×10^5	[Au(L4)](Cl)	265, 339	2.59×10^4	2.06×10^4
H_2L5	265	3.00×10^4	[Au(L5)](PF_6)	N/A	N/A	N/A
H_2L6	260	2.11×10^4	[Au(L6)](PF_6)	N/A	N/A	N/A
H_2L7	268	2.40×10^4	[Au(L7)](PF_6)	N/A	N/A	N/A
H_2L8	265	2.30×10^4	[Au(L8)](PF_6)	N/A	N/A	N/A
H_2L9	266	1.10×10^4	[Au(L9)](Cl)	267, 331	2.82×10^4	1.11×10^4
H_2L10	266	1.21×10^4	[Au(L10)](PF_6)	267, 340	2.54×10^4	5.07×10^3

The data summarised in Table 4.2.1 show that all the ligands and gold(III) chelates have similar extinction coefficients. This suggests that the absorption spectra are dominated by the aromatic imidazole-imine groups; the structure of the alkyl bridging unit has little influence.

4.3 NMR spectroscopy

4.3.1 Introduction

Nuclear magnetic resonance (NMR) spectroscopy is the most commonly used characterization technique. NMR is easy to run, has wide application and provides a large amount of structural information. It was developed in the 1940's by physical chemists studying atomic nuclei, but in 1951 it was found NMR could be used to study organic structures. Atoms that have an odd number of protons or odd number or neutrons or both possess a property know as spin [7].

Due to its charge and spin, the nucleus has a magnetic moment. Without an external magnetic field the magnetic moments of the nuclei are randomly arranged, but in the presence of an external magnetic field the nuclei are ordered. The nuclei either align with or against the magnetic field. The nuclei that align with the magnetic field are in a lower energy state (α-spin) and the nuclei that align against the magnetic field are in a higher energy state (β-spin) [7].

When a pulse of electromagnetic radiation is delivered to the nuclei the α-spin states are promoted to the higher energy state and become β-spin states. This conversion is referred to as flipping. The energy supplied is in the radio frequency (rf) (3 kHz - 300 GHz) range. When flipping occurs a signal is generated whose frequency is proportional to the difference in energy from α-spin state to β-spin state [7].

The most common nuclei studied are ^{1}H, ^{13}C, ^{19}F and ^{31}P. This is because these isotopes have a spin quantum number of $\frac{1}{2}$ and, with the exception of ^{13}C, the NMR-active isotopes have a high natural abundance [8]. Although the gold(III) nucleus is diamagnetic, ^{197}Au NMR is not possible. This is due to the large quadrupole moment of the nucleus, which places it outside the range of most NMR spectrometers [8].

4.3.2 Results and discussion

The ^{1}H and ^{13}C NMR spectra of H_2L9 and $[Au(L9)](PF_6)$ are shown in Figures 4.3.1 to 4.3.4 as representative examples of the NMR spectra of the free ligands and gold(III) chelates.

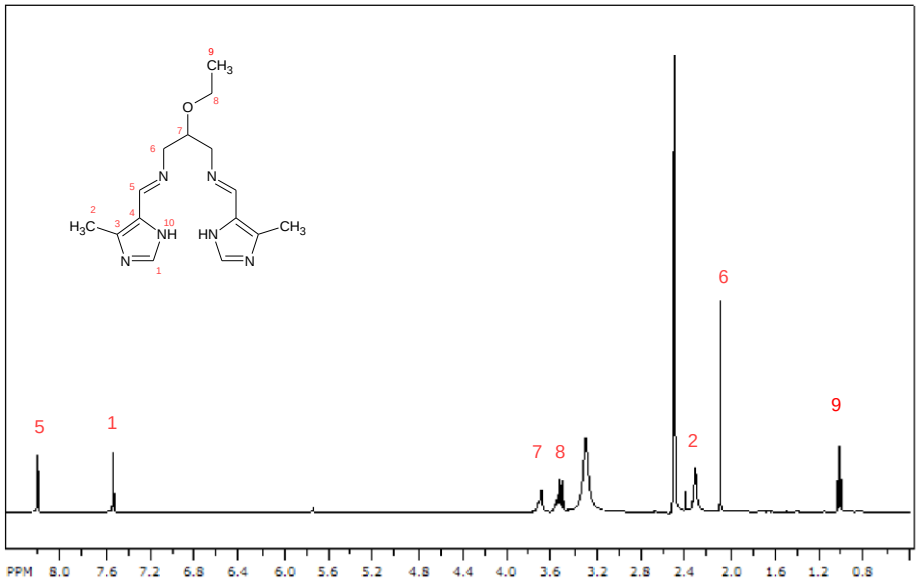

Figure 4.3.1: ^{1}H NMR spectrum of the free ligand H_2L9.

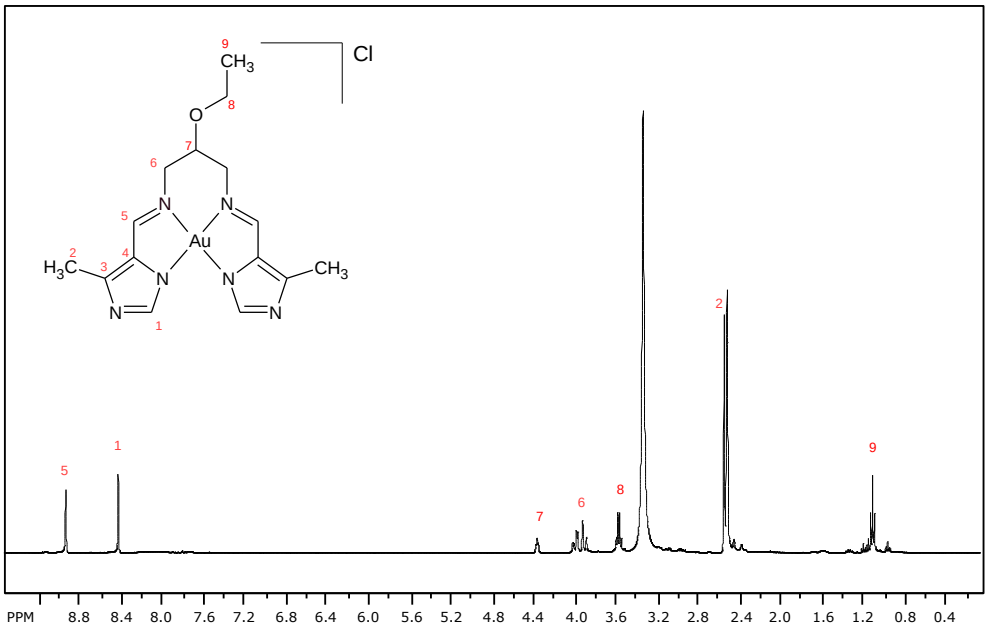

Figure 4.3.2: ^{1}H NMR spectrum of the complex $[Au(L9)](PF_6)$.

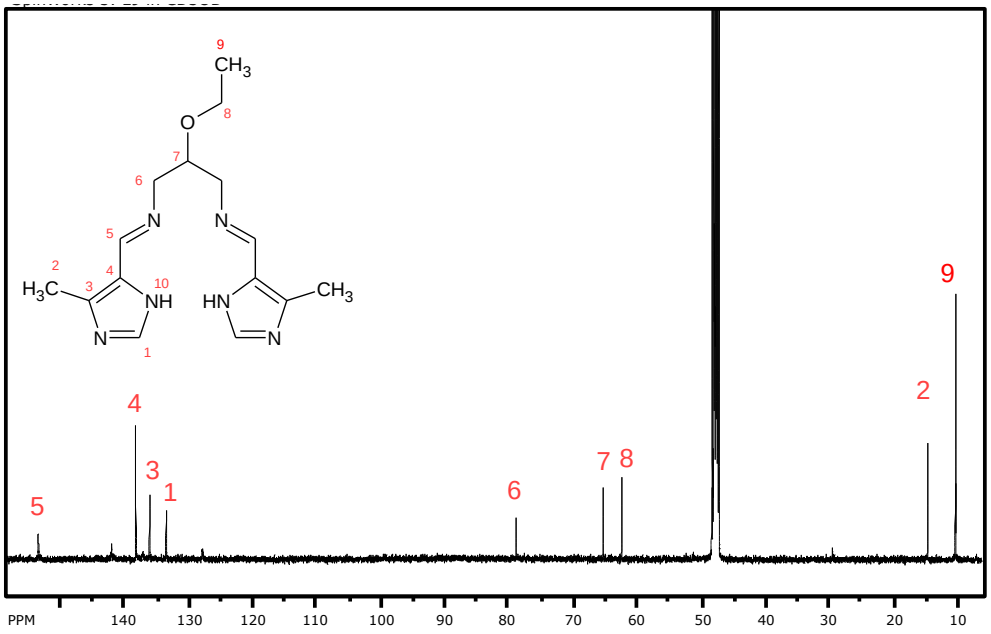

Figure 4.3.3: ^{13}C NMR spectrum of free ligand H_2L9.

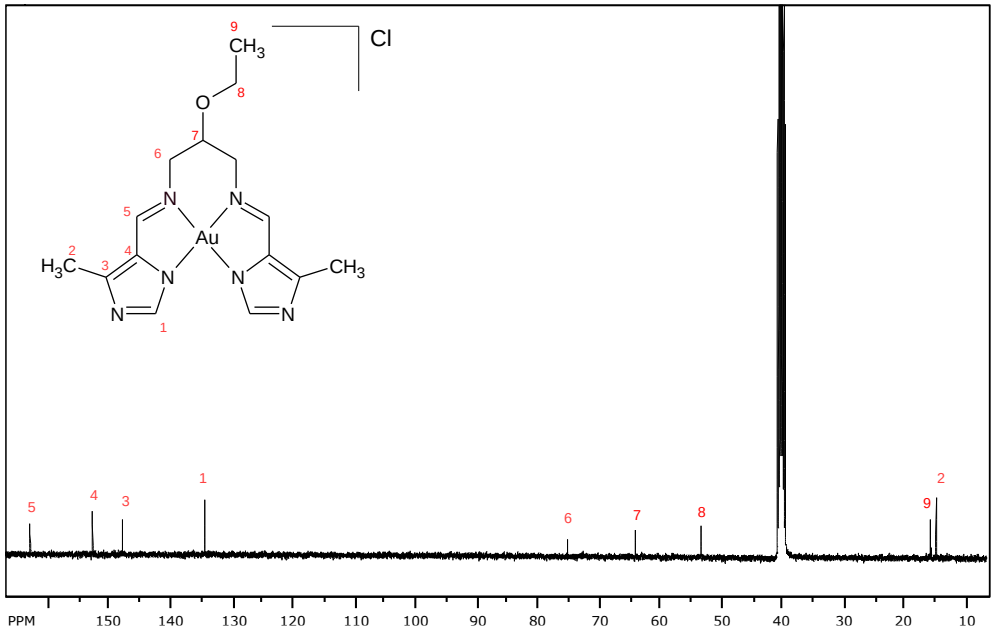

Figure 4.3.4: ^{13}C NMR spectrum of complex $[Au(L9)](PF_6)$.

A comparison of the chemical shifts of the ^{1}H NMR for H_2L9 and $[Au(L9)](PF_6)$ is shown in Table 4.3.1.

Table 4.3.1: A summary of the chemical shifts of the ^{1}H NMR for H_2L9 and $[Au(L9)](PF_6)$.

Proton	**H_2L9 (ppm)**	**$[Au(L9)](PF_6)$ (ppm)**
$CH_2CH(OCH_2C\mathit{H_3})_2CH_2$	1.02	1.10
$C\mathit{H_2}CH(OCH_2CH_3)_2C\mathit{H_2}$	2.08	2.54
Methyl	2.31	3.57
$CH_2CH(O\mathit{CH_2}CH_3)CH_2$	3.54	3.95
$CH_2C\mathit{H}(OCH_2CH_3)CH_2$	3.70	4.37
Imidazole CH	7.52	8.44
Imine	8.20	8.95
Imidazole NH	12.18	N/A

When comparing the ^{1}H NMR spectra of the free ligand and corresponding gold(III) chelate there is an overall downfield shift observed. The imine hydrogen experiences the largest downfield shift which is attributed to the strong deshielding effect of the metal ion. The smallest downfield shift is experienced by the methyl hydrogen atoms of the ethyl ether group which is due to the group being remote to the metal centre. The spectrum indicates a general polarisation of the ligand by the gold(III) Lewis acid. The ^{1}H NMR assignments for the remaining free ligands and metal chelates are reported in Chapter 2.

A comparison of the chemical shifts of the ^{13}C NMR spectra for H_2L9 and $[Au(L9)](PF_6)$ is shown in Table 4.3.2.

Table 4.3.2: A summary of the chemical shifts of the ^{13}C NMR spectra for H_2L9 and $[Au(L9)](PF_6)$.

Carbon	**H_2L9 (ppm)**	**$[Au(L9)](PF_6)$ (ppm)**
Methyl	10.00	14.60
$CH_2CH(OCH_2\mathit{C}H_3)CH_2$	14.39	15.60
$CH_2CH(O\mathit{C}H_2CH_3)CH_2$	62.29	53.27
$CH_2\mathit{C}H(OCH_2CH_3)CH_2$	65.17	63.97
$\mathit{C}H_2CH(OCH_2CH_3)\mathit{C}H_2$	78.79	75.16
1	128.07	134.59
3	137.38	148.01
4	142.32	152.97
Imine	153.76	163.19

The ^{13}C data show that the carbon bonded to the imine has the largest downfield shift while the bridging unit carbons do not experience a significant downfield shift as they are the furthest from the gold(III) ion. This downfield shift is again due to the deshielding effect of the chelated gold(III) metal ion. The methoxy and ethoxy groups do influence the shifts as they are electron donating groups. The ^{13}C NMR assignments for the remaining free ligands and metal chelates are reported in Chapter 2.

The ^{19}F and ^{31}P NMR spectra of [Au(L10)](PF6) are shown in Figures 4.3.5 and 4.3.6 as representative examples of heteronuclear NMR spectra of the gold(III) chelates. These spectra are used to confirm the identity of the counter anion in conjunction with X-ray crystallography. This is important as cationic gold(III) chelates are known to readily form as the tetrachloroaurate(III) and dichloroaurate(I) complex salts.

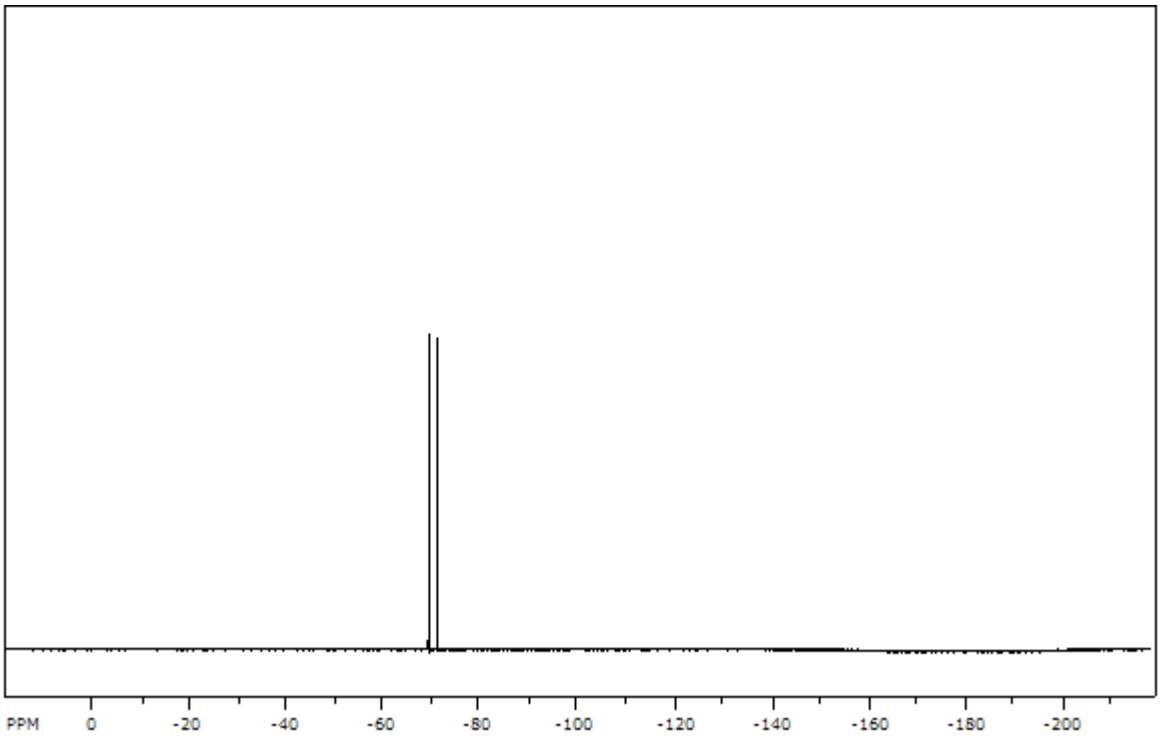

Figure 4.3.5: ^{19}F NMR spectrum of complex [Au(L10)](PF_6).

In the ^{19}F NMR spectra a large doublet is observed indicating coupling between the phosphorous and fluorine atoms in hexafluorophosphate(V).

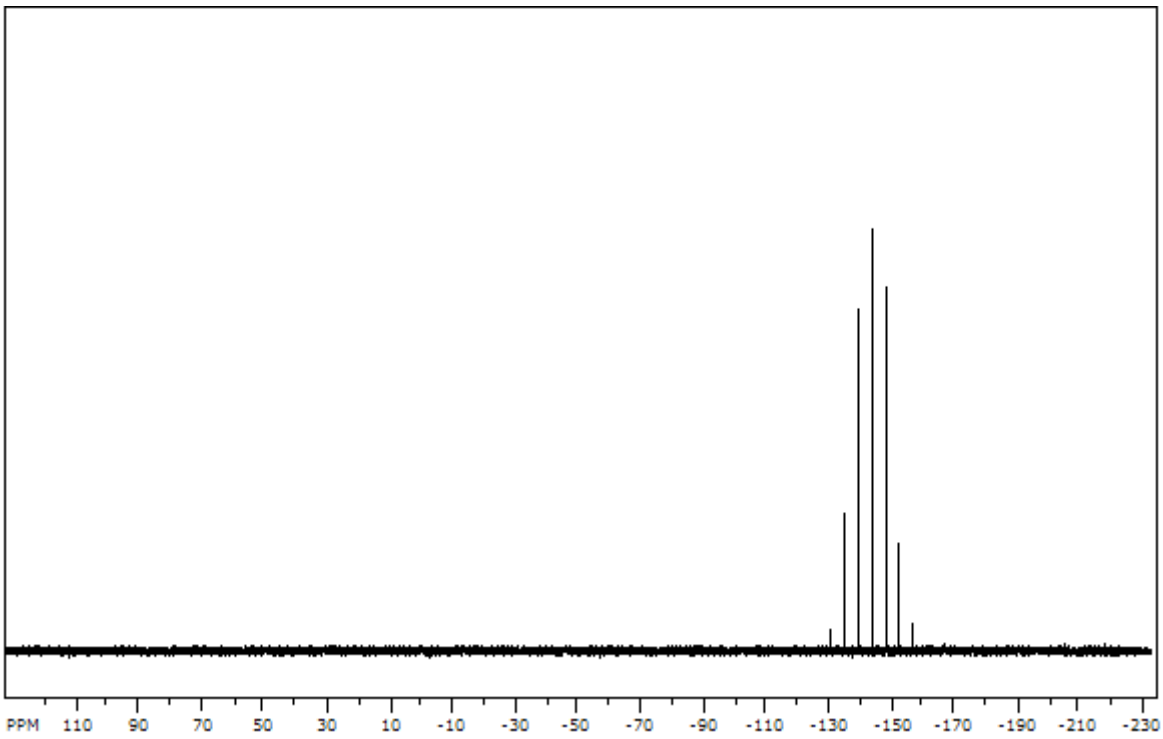

Figure 4.3.6: ^{31}P NMR spectrum of complex [Au(L10)](PF_6).

In the ^{31}P NMR spectra, seven lines are observed indicating that six fluorine atoms are bonded to the phosphorus atom. By using ^{19}F and ^{31}P NMR techniques it is possible to prove that the counter ion is indeed PF_6.

4.4 DNA binding studies

4.4.1 Introduction

DNA is responsible for many aspects of life such as controlling the function of cells. DNA is an important target for a large range of anticancer drugs [10]. The novel gold(III) chelates synthesised in this study are designed to be targeted DNA intercalating chemotherapeutic agents. This intercalation will in inhibit DNA replication resulting in apoptosis [11]. For a metal complex to intercalate it is required to have two vital features:

1. A planar aromatic region which allows the metal complex to insert between DNA base pairs.
2. The metal complex must have an overall cationic charge. This is required to interact with the negatively charged phosphate backbone of DNA stabilising the DNA/drug conjugate [12][13].

Chelate [Au(L4)](PF_6) is expected to form hydrogen bonds with DNA as it has an OH functional group on the bridging unit. This hydrogen bond could potentially further stabilise the DNA/drug conjugate.

In this study, two methods were employed to determine the binding affinity of the gold(III) chelates. The first is a direct binding method and the second is a competitive binding method. In the direct binding method the binding constant is determined by monitoring the absorption spectrum of the metal chelate as a function of calf thymus DNA (ctDNA) concentration. The ctDNA is intercalated by the metal chelate thus lowering the effective concentration of the metal chelate in solution typically leading to both hypochroism and a bathochromic shift. The binding constant is calculated by using the change in absorption as a function of the concentration of ctDNA [14].

In a competetive binding experiment a second, known DNA intercalating compound is used, in this case ethidium bromide (EB). EB and ctDNA both have weak florescence, but when EB intercalates ctDNA it has strong florescence. This large change in florescence is due to the nucleic acids which absorb UV light (260 nm) and then passes on this energy to EB [15]. By introducing the metal chelate (the second intercalator) the florescence emission of ctDNA intercalated by EB can be quenched as the metal chelate replaces the intercalated EB [16]. By monitoring the emission spectrum of the EB/DNA conjugate as a function of metal chelate concentration it is possible to determine an apparent binding constant.

4.4.2 Experimental

The stock ctDNA that was used in all DNA binding experiments was purchased from Sigma Aldrich (Germany).

For direct binding a phosphate buffer was prepared using monosodium phosphate and disodium phosphate. The final ionic strength of the solution was 0.1 M. The pH of the buffer solution was raised to the required 7.1 using a concentrated NaOH solution. The buffers were prepared and the experiments preformed at 37˚C to mimic the mammalian cellular environment.

The masses of the acid and base required were calculated using the Henderson-Hasselbach

equation: $pH = pKa + \log(\frac{[Base]}{[acid]})$ …(1)

Two cuvettes were used; one as a reference and the second for the sample. The reference cuvette contained only 10% DMSO and 90% phosphate buffer while the second cuvette contained DMSO, phosphate buffer and metal complex, at a concentration of approximately 2×10^{-5} M . Aliquots of DNA were added to both cuvettes to account for the absorbance of the DNA itself. The absorption values are fitted to equation 2 shown below.

$$\left(\frac{\varepsilon_a - \varepsilon_f}{\varepsilon_b - \varepsilon_f}\right) = \frac{\left(b - \left(\frac{b^2 - 2K_b^2 C_t[DNA]}{s}\right)^{\frac{1}{2}}\right)}{2K_b C_t} \ldots (2)$$

Where: $b = 1 + K_b C_t + \frac{K_b[DNA]}{2s}$

ε_a = Extinction coefficient of the EB band at given [ctDNA]

ε_f = Extinction coefficient of free EB

ε_b = Extinction coefficient of fully intercalated EB

K_b = Equillibrium binding constant in M^{-1}

C_t = Total concentration of ctDNA

s = Binding site size

For competitive binding a 25 mM tris-HCl buffer was prepared using ulta-pure water. This solution was adjusted to pH 7 using 1 M HCl. The ctDNA was dissolved in the buffer solution and the concentration was determined spectroscopically using an extinction coefficient of 13200 $M^{-1}cm^{-1}$ per base pair. A solution of 15 µM ctDNA and 15 µM EB was prepared with 15% DMSO in the tris-HCl buffer. Gold(III) chelate stock solutions were also prepared in DMSO.

Aliquots of the gold(III) chelate solution were added to the ctDNA-EB solution. The emission of the sample was recorded between 530 nm and 800 nm using an excitation wavelength of 500 nm after each addition. The apparent binding constant is calculated using equation 3.

$$K_{app}\,[complex] = K_{EB}[EB] \ldots (3)$$

Where: K_{EB} = binding constant of EB to ctDNA

$[EB]$ = molar concentration of EB

$[complex]$ = concentration of the gold(III) chelate that causes a 50% quenching of the initial EB fluorescence (C_{50})

Io (initial fluorescence intensity) is determined from a non-linear squares fit of the change in EB emission at 615 nm and f(x), with the concentration of the metal chelate, x, to equation 4.

$$f(x) = \frac{Io \times C_{50}}{x + C_{50}} \ldots (4)$$

The value of K_{EB} is determined in a separate experiment using a direct DNA titration as described above.

4.4.3 Results and discussion

Determination of the ctDNA binding constants was first attempted for all five gold(III) chelates by direct titration using different concentrations of ctDNA and gold(III) chelate. Signs for successful intercalation include a decrease in absorption intensity and a bathochromic shift. These signs are a result of a decrease in concentration of metal complex in solution as it intercalates the DNA. The results of the direct binding DNA titration are shown in Figure 4.4.1.

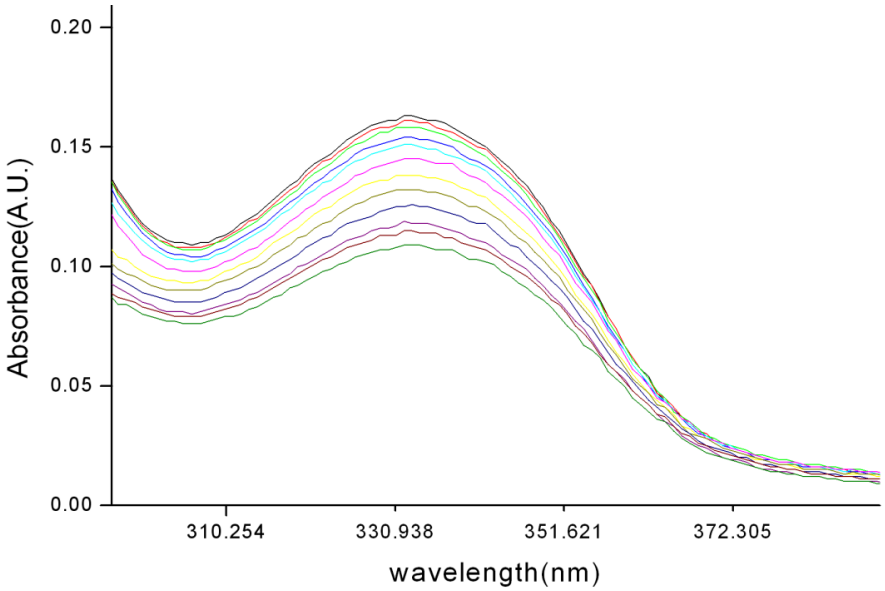

Figure 4.4.1: Absorption spectrum of [Au(L1)](PF_6) with increasing concentrations of ctDNA.

Figure 4.4.1 initially suggests an interaction between the metal complex and ctDNA. However, if the dilution effects of the addition of the aliquots of DNA are accounted for then it is clearly evident that there is no detectable DNA binding. The spectra also show no isosbestic point, which is usually associated with a change of species in solution. The ctDNA has an absorption maximum at 260 nm. It is believed that the absorption of the ctDNA may obscure the absorbance of the metal chelate (lambda max at 330 nm) thus masking the spectroscopic changes associated with intercalation. This leads to a negative result. To solve this issue, a competitive binding experiment was employed as this is independent of the UV/visible absorption properties of the metal chelate.

Competitive binding was attempted with different concentrations of ctDNA and gold(III) chelate, but again only the dilution effect was observed. This lead to the conclusion that the gold(III) chelates in this study are very weak DNA intercalators. This is likely due to the two methyl groups on the imidazole rings. The methyl groups would cause steric hinderence and prevent the gold(III) chelate from intercalating between DNA base pairs. The failure to synthesise [Au(L3)](PF_6) shows that as the inductive effect of the methyl groups is required to stabilise the gold(III) ion. A possible way around this obstacle is to move the position of the methyl groups as shown in Figure 4.4.3.

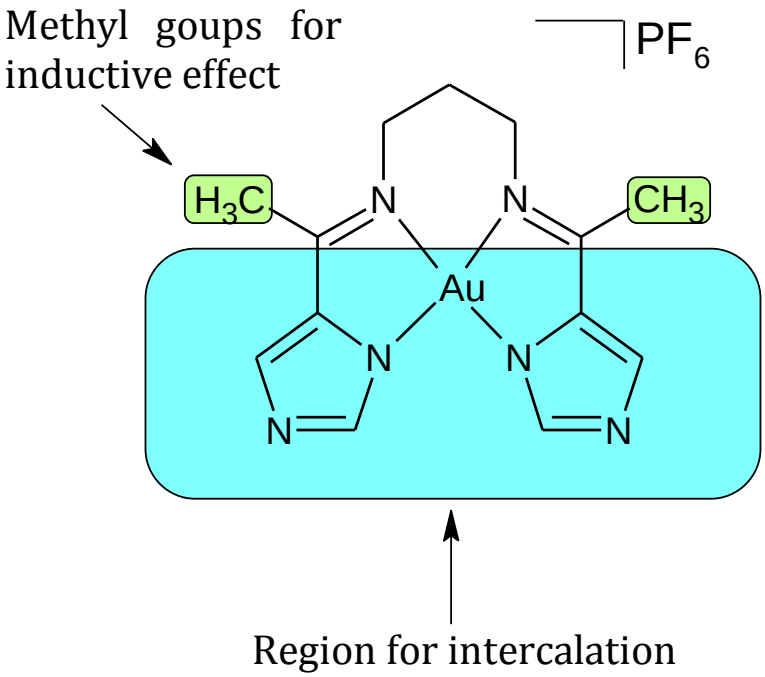

Figure 4.4.3: Proposed structure for gold(III) chelates that would likely improve DNA intercalation.

By using 1-(1*H*-imidazol-5-yl)ethanone instead of 4-methyl-1*H*-imidazole-5-carbaldehyde, it will create a larger planar aromatic region for intercalation while still obtaining the inductive effect of the methyl groups needed to stabilse the gold(III) ion.

4.5 References

1. Bruice, P. *Organic Chemistry*; 6th ed.; Prentice Hall: Upper Saddle River, N.J., 2010; pp. 115-120.
2. Pavia, D. *Introduction to spectroscopy*; Brooks/Cole, Cengage Learning: Belmont, CA, 2009.
3. R. M. Silverstein; *Spectrometric identification of organic compounds*. 7th ed.; John Wiley & sons: Hoboken, NJ, 2005.
4. Brisdon, A. *Inorganic Spectroscopic Methods*; Oxford University Press: Oxford, 1998.
5. Comas-Vives, A.; González-Arellano, C.; Corma, A.; Iglesias, M.; Sánchez, F.; Ujaque, G. *J. Am. Chem*. Soc. **2006**, 128, 4756-4765.
6. Yamada, S.Yamanouchi, K. *Bull. Chem. Soc. of Jpn.,* **1970**, 43, 1744-1746.
7. Bruice, P. Organic Chemistry; 6th ed.; Prentice Hall: Upper Saddle River, N.J., 2010; pp. 115-120.
8. Hore, P. Nuclear Magnetic Resonance; Oxford University Press: Oxford, 1995.
9. Akerman, M. P., *Structural physical and biological studies of gold(III) Bis(Pyrrolide-Imine) Schiff base complexes : potential chemotherapeutic agents*, University of KwaZulu Natal, 2011.
10. Rehman, S. U., Yaseen, Z., Husain, M. A., Sarwar, T., Ishqi, H. M. and Tabish, M.; *PLoS ONE* **2014**, 9 (4), 1-11.
11. Munro, O. Q., Akerman, K. J. and Akerman, M. P. Gold Complexes for Use in the Treatment of Cancer. US Patent 20,130,090,472. 2013.
12. Zeglis, B. M., Pierre, V. C. and Barton, J. K.; *Chem. Commun*. **2007**, 44, 4565-4579.
13. Ke-Liu, H. and Sadler, P. J.; *Acc. Chem. Res.,* **2011**, 44 (5), 349-359.
14. Chen, L.; Liu, J.; Chen, J.; Tan, C.; Shi, S.; Zheng, K.; Ji, L. *J. Inorg. Biochem.*,**2008**, 102, 330-341.
15. LV, Y.-K., Li, P., Jiao, M.-L., Liu, B. S. and Yang, C.; *Turk. J. Chem*. **2014**, 38, 202-209.
16. Garcia-Gimenez, J. L., Gonzalez-Alvarez, M., Liu-Gonzalez, M., Macias, B., Borras, J. and Alzuet, G.; J. *Inorg. Biochem* **2009**, 103, 923-934.
17. Barnholtz, S. L., Lydon, J. D., Huang, G., Venkatesh, M., Barnes, C. L., Ketring, A. R. and Jurisson, S. S.; *Inorg. Chem*. **2001**, 40, 972-976.

Chapter 5| X-Ray Crystallography

5.1 Introduction

5.1.1 Previously reported ligands

A total of ten bis(imidazole-imine) ligands were synthesised in this project, two of which have been crystallised and studied by single crystal X-ray diffraction. A Search of the Cambridge Structural Database (CSD) [1] shows very few bis(imidazole-imine) compounds have been studied by single crystal X-ray diffraction. Related structures which have a common bridging unit to those studied in this work are summarised in Table 5.1.1. the structure of the compounds are illustrated in Figure 5.1.1.

Table 5.1.1: Reported X-ray structures of similar bis(imidazole-imine)ligands

CSD Ref. Code	Compound Name	Lit. Ref.
DAZXOS	*N,N'*-bis(1*H*-Pyrrol-2-ylmethylene)cyclohexane-1,2-diamine	2
XUVQAG	*N,N'*-cycloexylenebis(pyrrol-2-ylmethyleneamine)	3
EFAROU	(1R*,2S*)-*N,N*-Bis[(*E*)-1*H*-pyrrol-2-ylmethylidene]cyclohexane-1,2-diaminemonohydrate	4
WOBNAD	4-Methyl-1*H*-imidazole - 5-((ethylidenehydrazinylidene)methyl)-4-methyl-1*H*-imidazole	5

The X-ray structures reported in Table 5.1.1 exhibit structural similarities to those studied by X-ray crystallography in this work. The similarities include methyl-imidazole rings (in some cases) and imine bonds with six-membered cyclohexyl rings acting as bridging units.

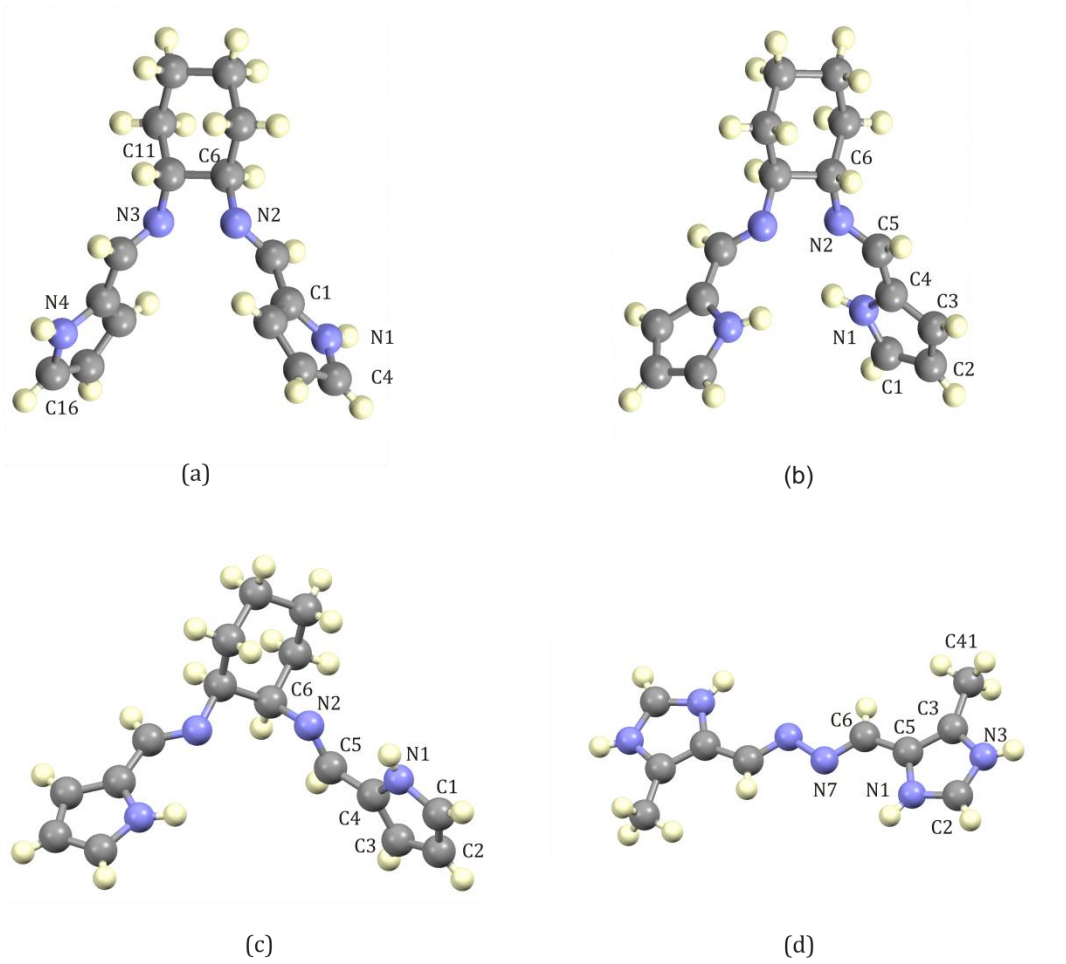

Figure 5.1.1: Partially labelled X-ray structures of (a) DAZXOS (b) XUVQAG (c) EFAROU (d)WOBNAD.

N-(pyridin-2-ylmethylene)-*N*'-(pyridin-4-ylmethylene) cyclohexane-1,2-bis-imine (DAZXOS) crystallized in the monoclinic space group *C*2/*c*. The ligand exhibits a one-dimensional supramolecular network. The one-dimensional network is stabilised by two unique hydrogen bonds between the imine N (H-bond acceptor) of one molecule and the imidazole NH atom (H-bond donor) of an adjacent molecule (N1···H1=2.00(1); N1···N3=2.944(1)Å) as shown in Figure 5.1.2 below.

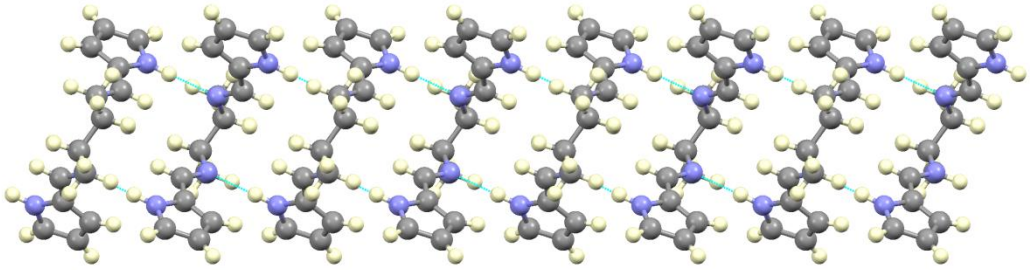

Figure 5.1.2: One-dimensional network of DAZXOS stabilised by hydrogen bonds between the imine N atoms and the imidazole NH atoms of adjacent molecules in the solid state.

N,N'-cyclohexylenebis(pyrrol-2-ylmethyleneamine) (XUVQAG) crystallised in the $P22_12_1$ space group. Significant bond lengths are summarised below in Table 5.1.2

Table 5.1.2: Summarised bond lengths for XUVQAG.

Atoms	Bond length (Å)
N1-C1	1.367(3)
N1-C4	1.352(3)
C4-C5	1.442(3)
N2-C5	1.276(3)
N2-C6	1.459(3)

It is important to note that this compound crystallises as the hydrate with a single water molecule associated with each ligand molecule. The water molecule acts as both a hydrogen bond acceptor and hydrogen bond donor, bridging adjacent ligand molecules. This hydrogen bonding motif leads to a one-dimensional supramolecular structure co-linear with the *c*-axis. The pyrrole NH and imine N atoms act as hydrogen bond donors and acceptors, respectively bonding to the water molecule. This geometry leads to two unique hydrogen bonds. The bond parameters are summarised in Table 5.1.3. The hydrogen-bonded supramolecular structure is shown in Figure 5.1.3.

Table 5.1.3: Hydrogen bond lengths (Å) and bond angles (˚) of XUVQAG.

D-H···*A*	**D-H**	**H···*A***	**D···*A***	**D-H···*A***
O···N2	1.05	1.76(4)	2.783(3)	164.2
O···N1	0.91(3)	2.00(2)	2.868(2)	159.6

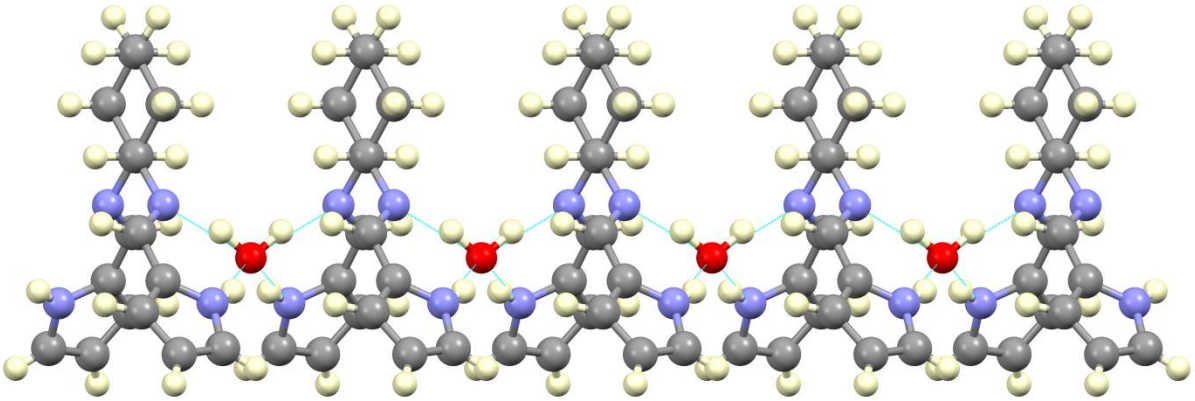

Figure 5.1.3: Structure of XUVQAG stabilised by hydrogen bonds between the water molecule and imine N atoms and the pyrrole NH groups of adjacent molecules in the solid state.

Compound EFAROU crystallised in the monoclinic space group, $P2_1/n$ as the dihydrate with and two water molecules in the asymmetric unit as shown in Figure 5.1.4. Both molecules have similar conformations with an root mean square deviation of 0.242 Å highlighting the similarity. The two water molecules bridge the two ligand molecules through a similar hydrogen bonding motif to that described above. The asymmetric unit is therefore an unusual example of a hydrogen-bonded heterotetramer stabilised by eight unique hydrogen bonds. The bridging water molecule acts as both a hydrogen bond acceptor and donor. The hydrogen bond parameters are summarised in Table 5.1.4. The mean imine bond lengths are 1.270(4) Å, illustrating their double bond character.

Table 5.1.4: Hydrogen bond parameters (Å,°) for EFAROU.

D–H···A	D–H	H···A	D···A	D–H···A
O1W–H1W···N3A	0.82 (3)	2.28 (3)	3.014 (2)	149 (3)
O1W–H2W···N3B	0.92 (3)	1.96 (3)	2.857 (2)	166 (3)
O2W–H3W···N2B	0.80 (3)	2.16 (3)	2.927 (2)	159 (3)
O2W–H4W···N2A	0.98 (3)	1.88 (3)	2.819 (2)	159 (2)
N1A–H01A···O2W	0.93 (2)	2.03 (2)	2.896 (2)	154 (2)
N1B–H01B···O2W	0.95 (2)	1.96 (2)	2.899 (2)	169 (2)
N4A–H04A···O1W	0.88 (2)	2.02 (2)	2.882 (3)	166 (2)
N4B–H04B···O1W	0.86 (3)	2.09 (3)	2.896 (3)	155 (2)

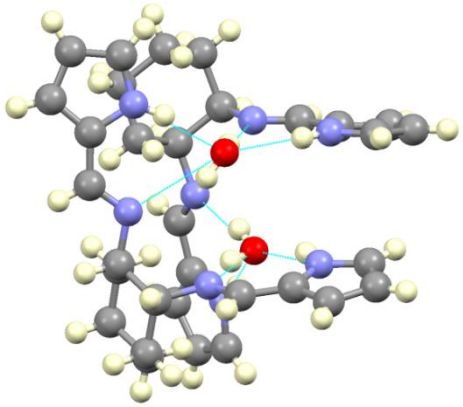

Figure 5.1.4: Heterotetrameric structure of EFAROU stabilised by hydrogen bonds between the water molecules and imine N atoms and pyrrole NH groups.

WOBNAD crystallised in the *Fddd* space group with a half molecule in the asymmetric unit and Z = 16. WOBNAD is the only example of a free ligand derived from methyl imidazole, such as those in this work, to be studied by single crystal X-ray crystallography. There are two unique hydrogen bonds stabilising the solid state structure. The nitrogen atoms act as a hydrogen bond acceptors and the NH groups hydrogen bond donors. The hydrogen bond parameters are summarised in Table 5.1.5. These hydrogen bonds give rise to a two-dimensional network as

shown in Figure 5.1.5. The network comprises one-dimensional chains, which are linear, these are cross-linked through hydrogen bonds to adjacent chains at an angle of ca. 134.1°.

Table 5.1.5: Hydrogen bond parameters (Å,°) for WOBNAD.

D-H···*A*	**D-H**	**H···*A***	**D···*A***	**D-H···*A***
N3–H3···N3	0.861	2.035	2.885(5)	169.2
N1–H1···N1	0.860	2.010	2.836(4)	160.8

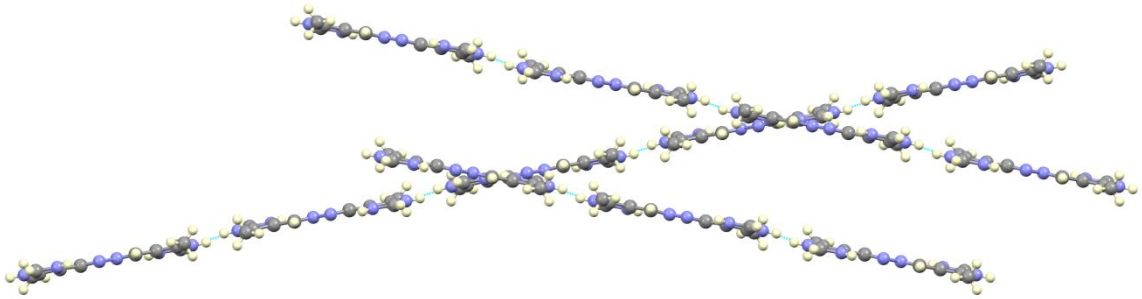

Figure 5.1.5: Two-dimensional hydrogen-bonded network structure of WOBNAD stabilised by hydrogen bonds between the imidazole N atoms and the imidazole NH atoms of adjacent molecules in the solid state.

5.1.2 Previously reported metal chelates

Three of the synthesised gold(III) chelates have been crystallised and studied by single crystal X-ray diffraction. A search of the Cambridge Structural Database (CSD)[1] shows very few gold(III) chelates with related ligands have been previously reported. The few relevant compounds are summarised in Table 5.1.6 and illustrated in Figure 5.1.6.

Table 5.1.6: Reported X-ray structures of related gold(III) chelates.

CSD Ref. Code	Compound Name	Lit. Ref.
RIZHAL	(3,10,17,21,26,27-hexaazapentacycloheptacosa-1(25),2,4(9),5,7,10,12,14,16,21,23-undecaenato)-gold(III) hexafluorophosphate	6
RIZHEP	(19,19-dimethyl-3,10,17,21,26,27-hexaazapentacycloheptacosa-1(25),2,4(9),5,7,10,12,14,16,21,23-undecaenato)-gold(iii) trifluoromethanesulfonate hemihydrate	6
RIZHIT	(12,13,14,15-tetrahydro-6,9:18,21-diepimino[1,6]diazacycloctadecino[12,13-b]-quinoxalinato]gold(III) hexafluorophosphate(V) mono (acetonitrile) solvate	6
RAVHIG	oxonium (5,7,12,14-tetramethyl-1,4,8,11-tetraazacyclo tetradeca-4,7,11,14-tetraene)-gold(III) tetrakis(perchlorate)	7
BAQHEG	BAQHEG : Aqua-(1,3-bis((5-methylimidazol-4-yl)methylideneamino)propan-2-ol)-zinc(II) diperchlorate monohydrate	8
MAYQIM	trans-Diaqua-(1,3-bis((5-methylimidazol-4-yl)methylideneamino)propan-2-ol)-manganese(ii) diperchlorate	8
MAYQOS	trans-Diaqua-(1,3-bis((5-methylimidazol-4-yl)methylideneamino)propan-2-ol)-nickel(II) diperchlorate	8
MAYQUY	Aqua-(1,3-bis((5-methylimidazol-4-yl)methylideneamino)propan-2-ol)-(perchlorato-O)-copper(II) perchlorate monohydrate	8
BAGHAT	(*N,N'*-bis(5-Methyl-4-imidazolylmethylidene)propane-1,2-diamino)-copper(II) diperchlorate	9

Table 5.1.6: Continued.

CSD Ref. Code	Compound Name	Lit. Ref.
KURQAR	Aqua-(N,N'-cyclohexane-1,2-diylbis(1-(5-methyl-1H-imidazol-4-yl)methanimine))-copper(ii) dinitrate	10
GASQEW	Chloro-(N,N'-bis(2-methylimidazol-4-ylmethylidene)-1,4-diaminobutane)-copper(ii) nitrate	11

The X-ray structures reported in Table 5.1.6 exhibit similar structural features to those synthesised in this work. The similarities include square planar gold(III) ions, tetradentate ligands joined through imine bonds and with three carbons acting as a bridging unit. Several of the ligands coordinated to gold(III) in this work have been chelated to various metals. These structures are shown in Figure 5.1.6.

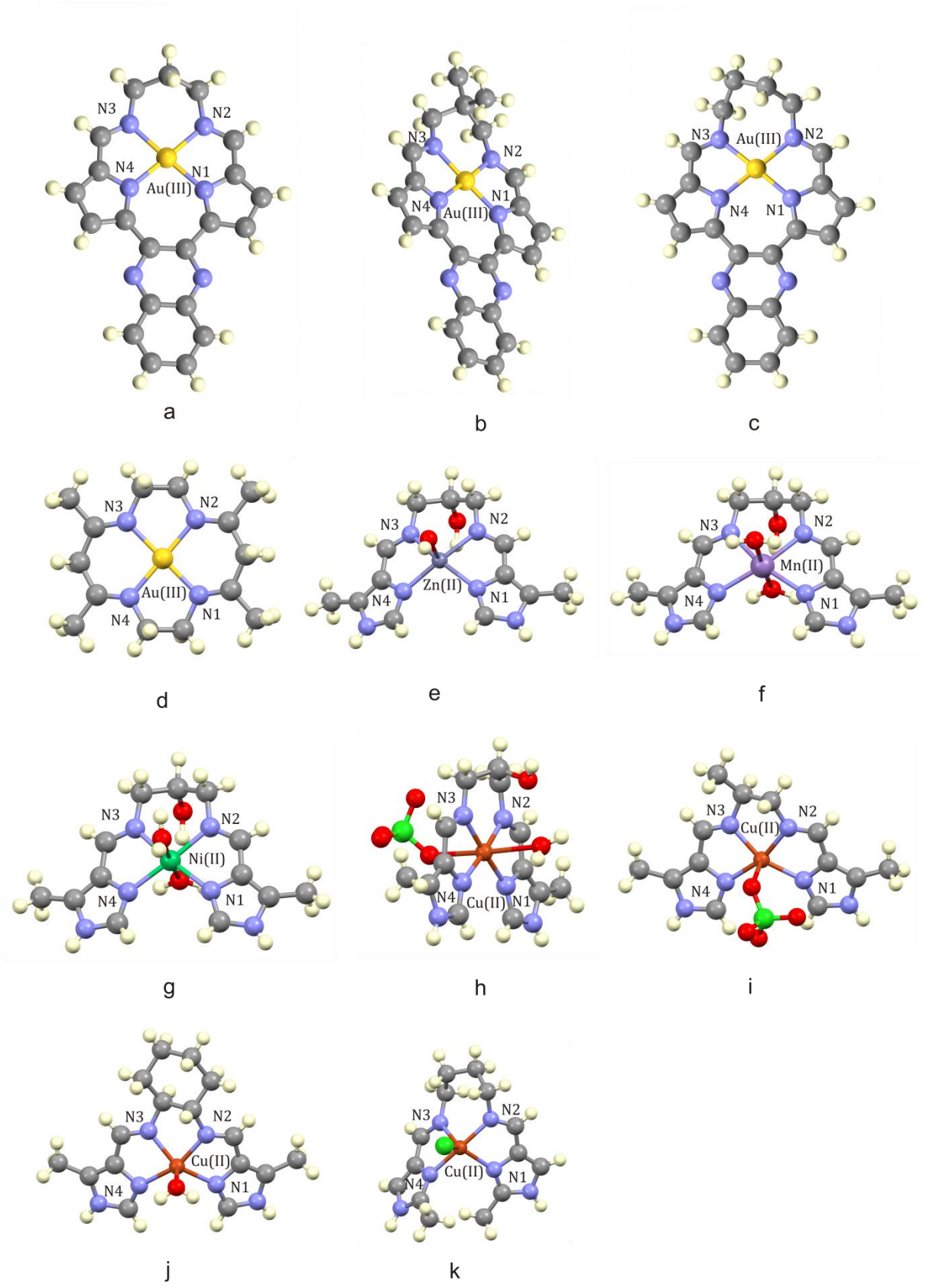

Figure 5.1.6.: Partially labeled structure of (a) RIZHAL (b) RIZHEP (c) RIZHIT (d) RAVHIG (e)BAQHEG (f) MAYQIM (g) MAYQOS (h) MAYQUY (i) BAGHAT (j) KURQAR (k) GASQEW.

Compound RIZHAL crystallised in the Monoclinic, *P*2/*c* space group. RIZHAL has a square planar coordination geometry , this is a result of the vacant dx^2-y^2 orbitals of the d^8 metal ion. The gold(III) ion is displaced slightly above the mean plane defined by the the aromatic rings. Relevant bond angles and bond lengths are summarised in Table 5.1.7. The bridging unit shows a characteristic out-of-plane distortion to accommodate the sp^3 hybridised carbon atoms of the di(azomethine) linkage.

Table 5.1.7: Summary of bond lengths and bond angles describing the coordination sphere of RIZHAL.

Bond	**Bond length (Å)**	**Bond angle(°)**
Average Au-N_{imine}	2.013	
Average Au-$N_{pyrrole}$	1.9845	
N_{imine} -Au-N_{imine}		97.22
N_{imine} -Au- $N_{pyrrole}$		81.77
$N_{pyrrole}$ -Au- $N_{pyrrole}$		99.20

Weak C-H···F interactions between the methylene hydrogen atoms and the fluorine atoms of the counter ion lead to a one-dimensional supramolecular structure co-linear with the *c*-axis. The anion acts as a bridge between the adjacent cationic gold(III) chelates. The structural parameters are summarised in Table 5.1.8. The Supramolecular structure is depicted in Figure 5.1.7.

Table 5.1.8: Bond parameters for the C-H···F interactions (Å,°) for RIZHAL.

D–H···A	**D–H**	**H···A**	**D···A**	**D–H···A**
C8–H8B···F2	0.969	2.559	3.138(9)	118.5
C9–H9···F2	0.930	2.781	3.009(8)	95.0
C5–H5···F5	0.931	2.698	3.084(8)	105.9

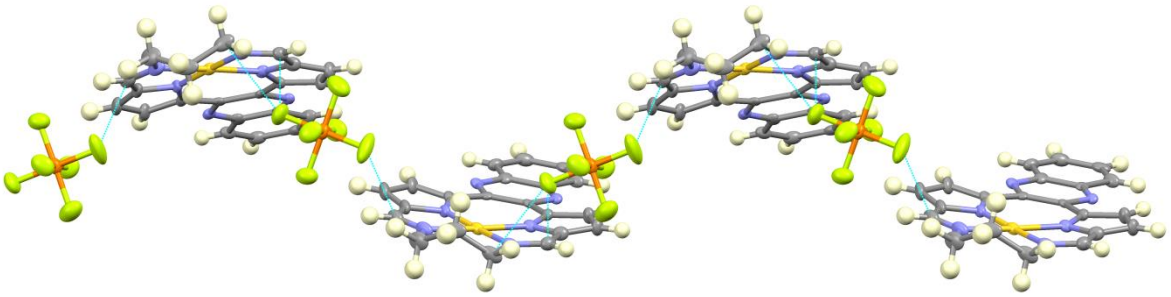

Figure 5.1.7: One dimensional network stabilised by C-H···F interactions in RIZHAL.

RIZHEP and RIZHIT exhibit similar coordination geometries to that described above. The mean Au-N_{imine} and Au-$N_{pyrrole}$ bond lengths for these compounds measure 1.984 Å, 1.984 Å for RIZHEP and 2.028 and 1.976 for RIZHIT, respectively. Weak C-H···O interactions between the pyrrole ring CH hydrogen atoms and the oxygen atoms of the counter ion lead to a one-dimensional supramolecular structure co-linear with the *b*-axis. The anion acts as a bridge between the adjacent cationic gold(III) chelates. The structural parameters are summarised in Table 5.1.9 The supramolecular structure is depicted in Figure 5.1.8.

Table 5.1.9: Bond parameters for the C-H···O interactions (Å,°) for RIZHEP.

D–H···A	**D–H**	**H···A**	**D···A**	**D–H···A**
C2–H2···O4	0.95	2.55	3.20(3)	126
C5–H5···O5	0.95	2.22	3.13(3)	158

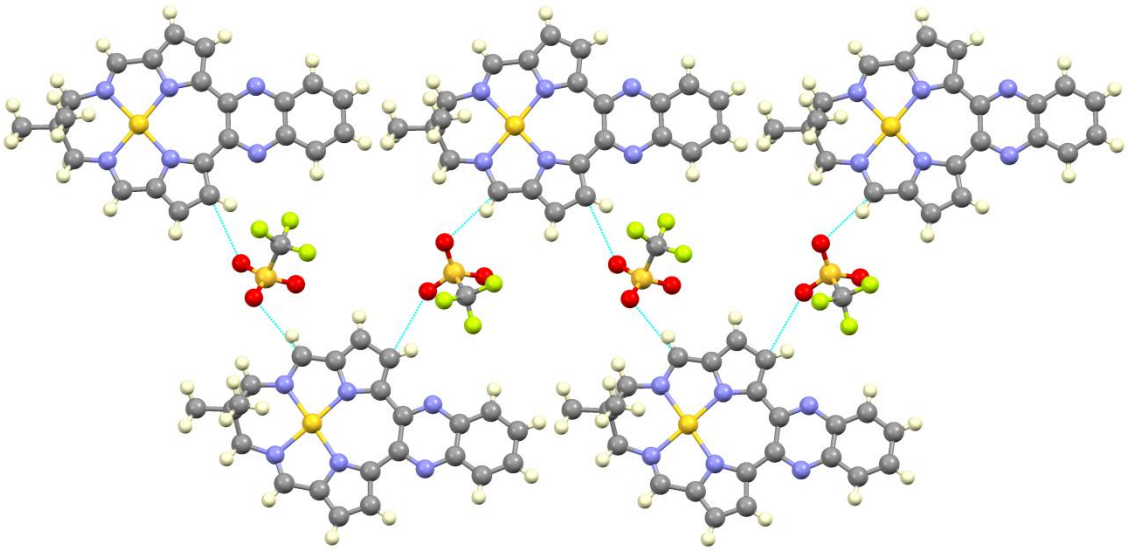

Figure 5.1.8: One dimensional network stabilised by C-H···O interactions in RIZHEP.

RIZHIT shows π-stacking in the form of head-to-tail and oblique dimers as shown below in Figure 5.1.9. The π-stacking is an indication of potential DNA intercalation.

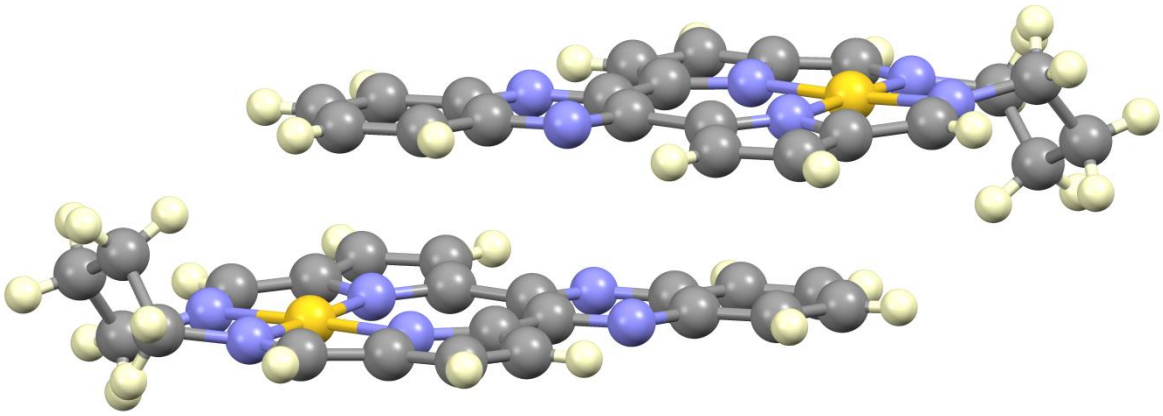

Figure 5.1.9: Head-to-tail π-stacked dimers of RIZHIT.

The ligand H_2L4 has been previously coordinated to a number of transition metals including Zn(II) in the compound BAQHEG. Compound BAQHEG crystallised in the orthorhombic space group *Pnma* with $Z = 4$. BAQHEG has a zinc(II) metal centre which is stabilised by four nitrogen donor atoms and has a distorted square-pyramidal coordination geometry with a water molecule occupying the fifth coordination site. The Zn(II) ion is displaced from the N_4 plane as shown in Figure 5.1.10. In the presence of nitrogen donor atoms zinc favours square planar or square pyramidal coordination geometries. A two-dimensional network is stabilised by four unique hydrogen bonds in the solid state structure. The water and perchlorate molecules

bridges two metal chelates (A and B) in the lattice to form a dimer. The polymer expands along the *c*-axis as shown in Figure 5.1.11. The hydrogen bond parameters are summarised in Table 5.1.10.

Table 5.1.10: Hydrogen bond parameters (Å,°) for BAQHEG.

D–H···A	**D–H**	**H···A**	**D···A**	**D–H···A**
C1–H1···O2	0.946(6)	2.502(9)	3.150(9)	125.7(4)
N2–H5···O4	0.831(5)	2.13(1)	2.91(1)	155.6(5)
O1W–H1W···O1	0.870	1.785	2.642	168.1
O1W–H1W···O2W	1.066	1.687	2.752	179.6

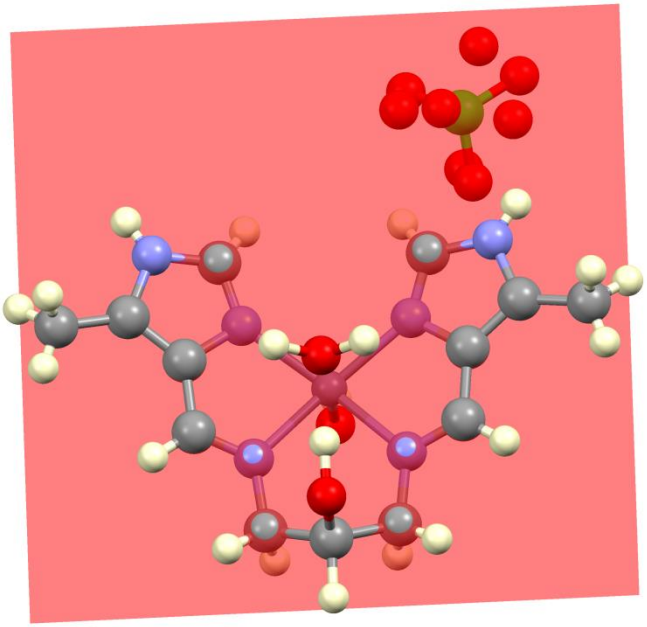

Figure 5.1.10: Out-of-plane distortion of the Zn(II) ion from the four-atom mean plane defined by the imidazole and imine nitrogen atoms for BAQHEG.

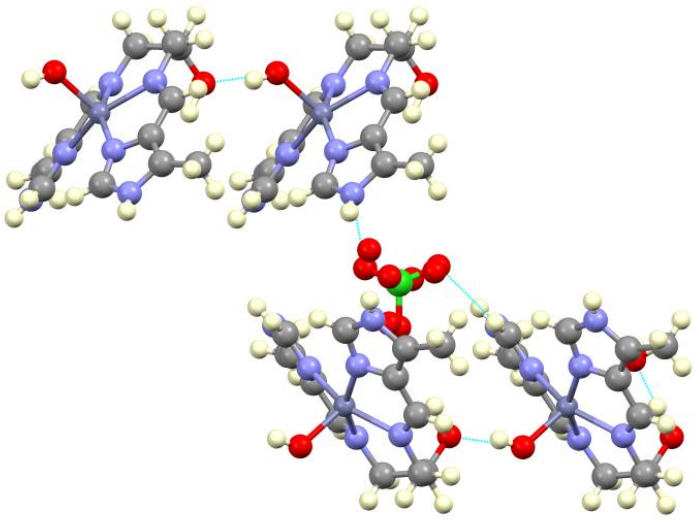

Figure 5.1.11: A two dimensional network is stabilised by four unique hydrogen bonds for BAQHEG.

The ligand H_2L4 has been previously coordinated to Mn(II) in the compound MAYQIM. Compound MAYQIM crystallised in the orthorhombic space group *Pnma* with Z = 4. MAYQIM has a manganese metal centre with is stabilised by four nitrogen donor atoms and two aqua ligands in the axial positons. MAYQIM has a distorted octahedral coordination geometry. The Mn(II) ion is located slightly above the N_4 plane as shown in Figure 5.1.12. In the presence of nitrogen donor groups manganese prefers to form a six-coordinate species.

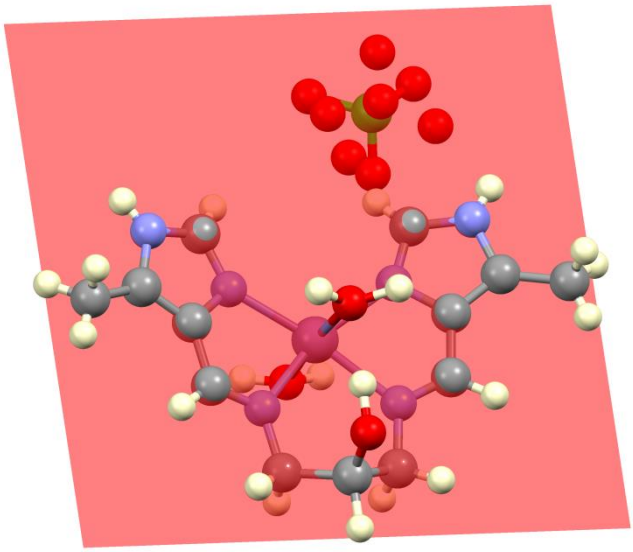

Figure 5.1.12: Deviation of Mn(II) from planarity as defined by the coordinating nitrogen atoms for MAYQIM.

The same ligand has also been coordinated to Ni(II) in the compound MAYQOS. Compound MAYQOS crystallised in the orthorhombic space group *Pnma* with *Z* = 4. MAYQOS has a nickel(II) metal centre with is stabilised by four nitrogen donor atoms from the bis(imidazole-imine) ligand and two aqua ligands found in the axial positons as shown in Figure 5.1.13. MAYQOS has a distorted octahedral coordination geometry. The Ni(II) ion is located slightly above the N_4 plane. In the presence of nitrogen donor groups nickel has a preference for forming six-coordinate species.

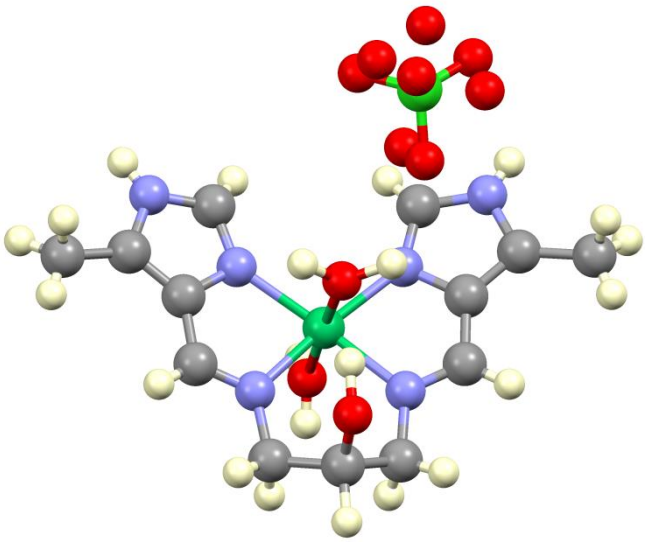

Figure 5.1.13: Crystal structure of MAYQOS showing the nominally octahedral coordination geometry.

The ligand H_2L4 also been coordinated to copper(II) in the compound MAYQUY. Compound MAYQUY crystallised in the monoclinic space group $P2_1/n$ with Z = 4. MAYQUY has a copper(II) metal centre which is stabilised by four nitrogen donor atoms in the equatorial position, one aqua ligands and one perchlorate oxygen atom in the axial positons shows a significant Z-out distortion (elongated axial ligand bonds) as predicted by the Jahn-Teller theorem. This Z-out distortion lowers the energy of all orbitals with a z-component and leads to an overall lower energy structure than could be achieved with an octahedral geometry.. The Cu(II) ion is in the N_4 plane as shown in Figure 5.1.14.

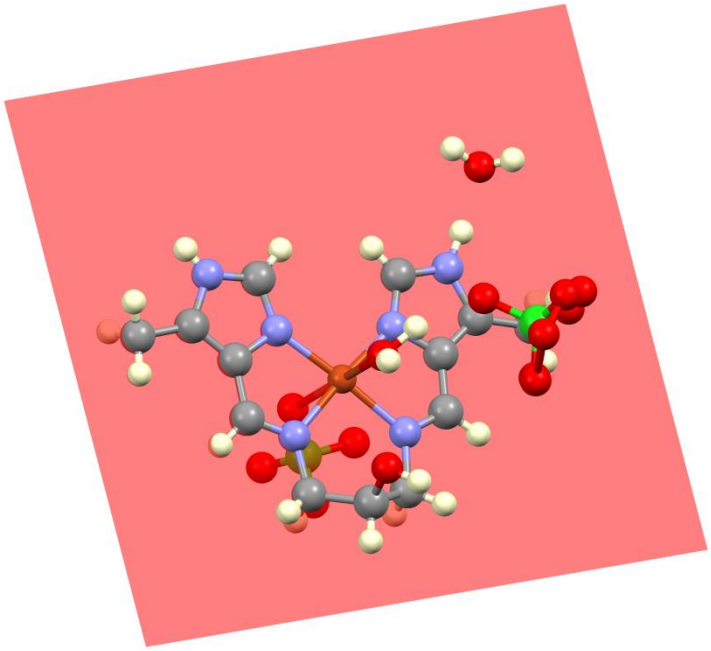

Figure 5.1.14: Deviation of Cu(II) from planarity as defined by coordinating nitrogen atoms for MAYQUY.

A ligand similar to H_2L8 has been coordinated to Cu(II) in the compound BAGHAT. Compound BAGHAT crystallised in the monoclinic space group $P2_1/n$ with Z = 4. BAGHAT has a copper metal centre with is stabilised by four nitrogen donor atoms in the equatorial position and one perchlorate oxygen atom found in the axial positon, forming a distorted square-pyramidal coordination geometry. The Cu(II) ion is in the basal plane of the N_4 donor atoms. The Cu(II) ion has a deviation of 0.143(2) Å from the defined N_4 plane towards the apical position shown in Figure 5.1.15, this is a commonly observed distortion in square pyramidal copper(II) chelates. The imidazole rings are also approximately planar forming dihedral angles of 9.1(3) and 3.0(3)˚.

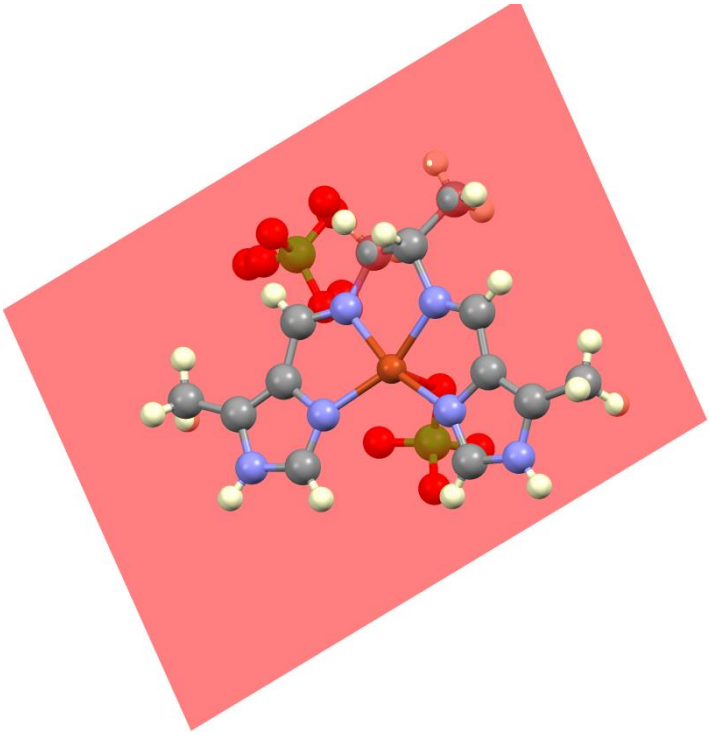

Figure 5.1.15: Deviation of Cu(II) from planarity as defined by the N_4 donor atoms for BAGHAT.

A ligand similar to H_2L6 has been coordinated to Cu(II) in the compound KURQAR. Compound KURQAR crystallised in the monoclinic space group $P2_1$ with Z = 2. KURQAR has a copper(II) metal centre which is stabilised by four nitrogen donor atoms in the equatorial position and one aqua ligand in the axial positon. KURQAR has a distorted square-pyramidal coordination geometry as shown in Figure 5.1.16. The Cu(II) ion again shows an out-of-plane distortion towards the axial aqua ligand. A one-dimensional network is stabilised by hydrogen bonds in KURQAR. The NO_3^- ion bridges three molecules in the lattice to form a two-dimensional supramolecular structure which is co-planar with the ab plane. The bonding motif is complex, an illustration is presented in Figure 5.17.

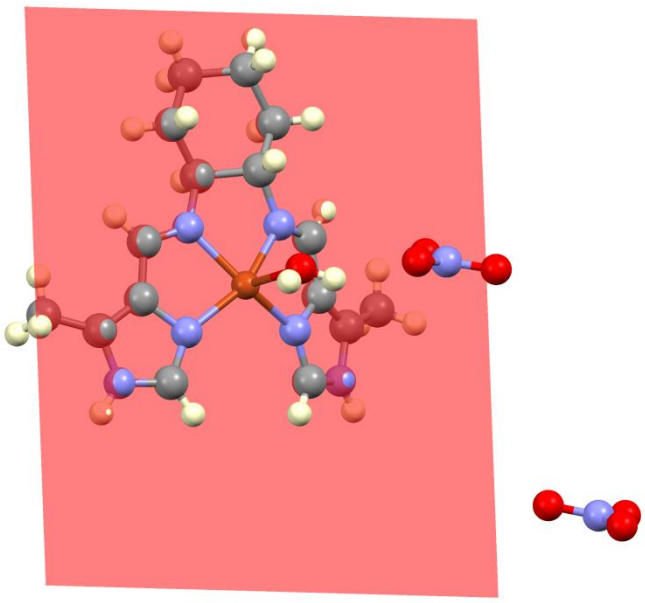

Figure 5.1.16: Deviation of Cu(II) from planarity as defined by the imidazole rings for KURQAR.

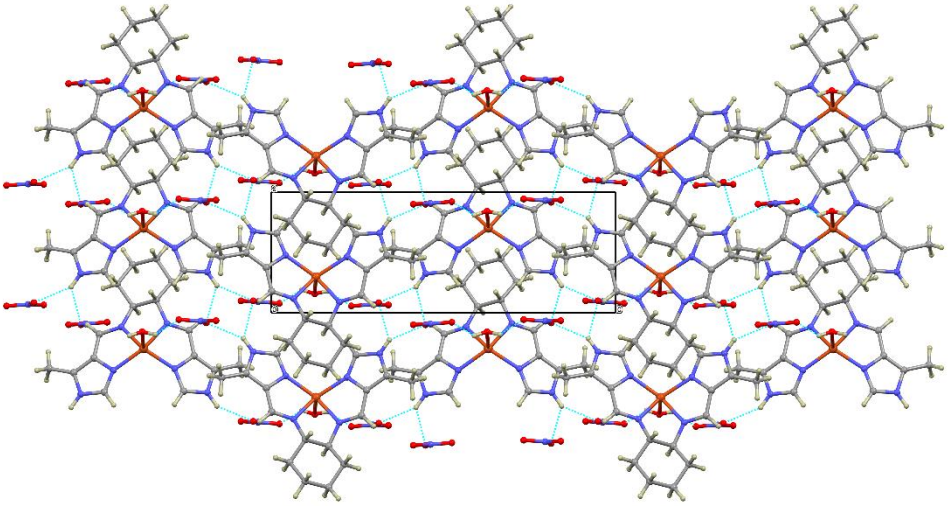

Figure 5.1.17: Two-dimensional supramolecular structure of KURQAR viewed down the c-axis.

The network illustrated in Figure 5.1.17 is supported by extensive hydrogen bonding. The hydrogen bond parameters are summarised in Table 5.1.11.

Table 5.1.11: Hydrogen bond parameters stabilising the two-dimensional network of KURQAR.

H-Bond	D–H	H···A	D···A	D–H···A
N6–H2···O4	0.900	2.160	2.954(7)	146.7
N2–H1···O4	0.901	2.337	2.989(6)	129.2
O1–H4···O2	0.851	2.068	2.775(7)	140.1
N6–H2···O7	0.900	2.341	2.965(7)	126.4
O1–H3···O6	0.850	2.112	2.842(8)	143.9
N2–H1···O7	0.901	2.219	3.007(8)	145.7

The bond lengths described in Table 5.1.11 are all significantly shorter than the sum of the van der Waals radii of the interacting atoms. Although bond length does not always correlate linearly with bond strength due to packing constraints in the lattice, these bonds are significantly shorter. This suggests that the interactions are likely to be moderate to strong.

A ligand similar to H_2L5 has been coordinated to Cu(II) in the compound GASQEW. Compound GASQEW crystallised in the triclinic space group *P*-1 with Z = 2. GASQEW has a copper(II) metal centre with is stabilised by four nitrogen donor atoms in the basal plane and an axial chloro ligand. GASQEW exhibits a severely distorted square-pyramidal coordination as shown in Figure 5.1.18. The Cu(II) ion is displaced from the basal plane towards the apical chloro ligand as has been a trend in the copper(II) chelates studied thus far. The severe distortion of the coordination geometry is likely the result of the additional degrees of freedom allowed by the four-carbon di(azomethine) linkage as opposed to the three -carbon bridges previously studied. The NO_3^- molecules bridges two chelates (A and B) in the lattice to form a dimer, this could also be referred to as a hydrogen-bonded heterotetramer. The supramolecular structure is illustrated in Figure 5.1.19. The hydrogen bond parameters are summarised in Table 5.1.12.

Table 5.1.12: Hydrogen bond parameters (Å,°) for GASQEW.

D–H···A	D–H	H···A	D···A	D–H···A
N1–H4···O2	0.951	1.885	2.785(4)	157.0
N6–H17···O2	0.950	1.900	2.827(4)	164.8

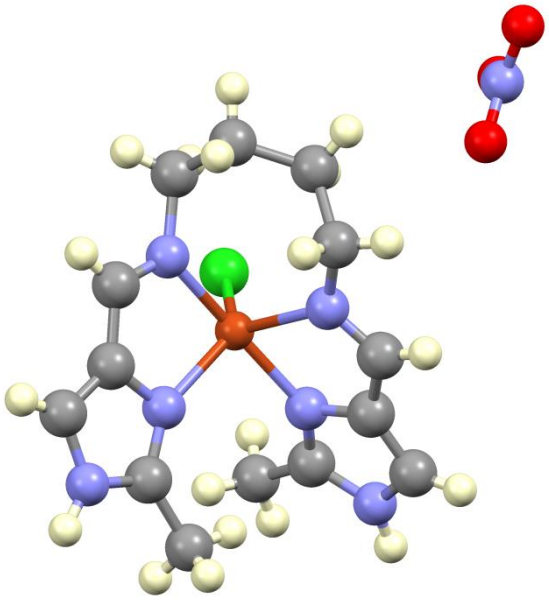

Figure 5.1.18: Crystal structure of GASQEW illustrating a distorted square-pyramidal coordination.

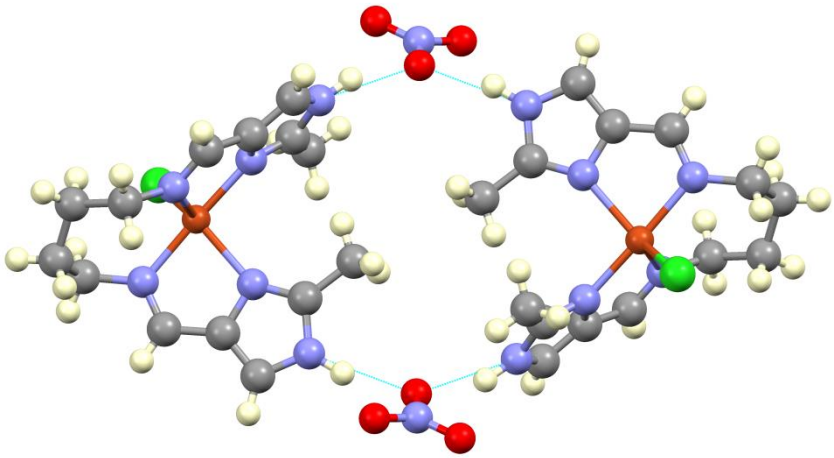

Figure 5.1.19: Metal chelates of GASQEW are bridged by hydrogen bonding through the nitrate counter ions and imidazole NH groups. This leads to a hydrogen-bonded heterotetramer.

An interesting feature of the above metal chelates coordinated to bis(imidazole-imine) ligands is that in all cases metal ion chelation has not required deprotonation of the imidazole NH. This is in stark contrast to the gold(III) chelates presented in this work which show concomitant deprotonation of the NH groups in all cases. This is consistent with the electron deficient gold(III) ion requiring the stronger sigma-donor ability of the anionic deprotonated imidazole NH for stability.

5.1.3 Objectives

The main aim of single crystal diffraction studies is to determine the solid state structure of the bis(imidazole-imine) ligands and their gold(III) chelates. The X-ray data will be used to deduce if these chelates can be effective DNA intercalators.

5.2 Experimental

All X-ray data were recorded on a Bunker Apex Duo diffractometer equipped with an Oxford Instruments Cryojet operating at 100(2) K and an Icoatec microsource operating at 30 W power. Ligand and chelate crystal refinement data are shown in Tables 4.2.1 and 4.2.2, respectively. All data were collected with Mo Kα (λ=0.71073 Å) radiation at a crystal-to-detector distance of 50 mm. All data collections were done using omega and phi scans with exposures taken at 30 W X-Ray power and 0.50˚ frame widths using APEX2[12]. The data were reduced with SAINT [12] using outlier rejection, scan speed scaling and standard Lorentz and polarisation correction factors. A SADABS semi-empirical multi-scan adsorption correction [12] was applied to all data. Direct methods, SHELXS [13] and WinGX [14] were used to solve the crystal structures. All non-hydrogen atoms were located in the difference density map and refined anisotropically with SHELXS [13]. The imidazole NH and water OH hydrogen atoms of the free ligands were located in the difference density map and refined isotropically.

The gold(III) chelates have residual electron density in the E-map. These peaks were found near the gold(III) ion and are the result of strong absorption by the gold(III) ion which was inadequately accounted for by the absorption corrections.

Table 5.2.1: Crystal refinement data for ligands.

Crystal Data	**H_2L6**	**H_2L7**
Chemical formula	$C_{16}\ H_{22}\ N_6.\ \frac{1}{2}\ H_2O$	$C_{16}\ H_{22}\ N_6.\ \frac{1}{2}\ H_2O$
Molar mass (g.mol^{-1})	307.40	307.40
Crystal system, space group	Tetragonal, P 4_3	Tetragonal, P 4_1
Temperature (K)	100	100
a, b, c (Å)	9.6624 (13), 9.6624 (13), 35.901 (5)	9.6384 (6), 9.6384 (6), 35.866 (2)
α, β, γ (°)	90, 90, 90	90, 90, 90
V (Å3)	3351.8 (8)	3331.9 (4)
Z	8	8
Radiation type	Mo Kα	Mo Kα
μ (mm-1)	0.08	0.08
Crystal size (mm)	0.50 × 0.19 × 0.12	0.35 × 0.20 × 0.15
Data collection		
Diffractometer	Bruker APEXII CCD Diffractometer	
Absorption correction	Multi-scanSADABS, Bunker2012	
No. of measured, independent and observed [I>2σ(I)] reflections	14768, 3334, 3214	15571, 3447, 3337
R_{int}	0.049	0.030
(sin θ/λ)max (Å^{-1})	0.617	0.626
Refinement		
R[F^2> 2σ(F^2)], *wR(F^2)*, S	0.056, 0.129, 1.20	0.042, 0.094, 1.19
No. of reflections	3334	3447
No. of parameters	434	434
No. of restrains	1	1
H-atom treatment	H atoms treated by a mixture of independent and constrained refinement	H atoms treated by a mixture of independent and constrained refinement
Δρmax.$\Delta\rho_{min}$ (e Å^{-3})	0.26, −0.26	0.18, −0.24

Table 5.2.2: Crystal refinement data for chelates.

Crystal Data	**[Au(L1)](PF$_6$)**	**[Au(L2)](PF$_6$)**	**[Au(L4)](Cl)**
Chemical formula	$C_{13}H_{16}AuF_6N_6P$	$C_{15}H_{20}AuF_6N_6P$	$C_{13}H_{11}AuCl0N_6O$
Molar mass (g.mol^{-1})	598.25	626.31	499.70
Crystal system, space group	Monoclinic, C c	Monoclinic, P2$_1$/c	Monoclinic, C2/c
Temperature (K)	100	100	100
a, b, c (Å)	16.1594 (11), 11.7820 (8), 9.5150 (7)	6.4295 (4), 17.0068 (11), 17.4120 (11)	10.9751 (7), 16.4315 (10), 9.4081 (6)
α, β, γ (˚)	90, 107.011 (3), 90	90, 90, 90	90,117.171 (2),90
V (Å3)	1732.3 (2)	1903.9 (2)	1509.40 (17)
Z	4	4	8
Radiation type	Mo Kα	Mo Kα	Mo Kα
μ (mm-1)	8.66	7.88	9.93
Crystal size (mm)	0.45 × 0.11 × 0.03	-	-
Data collection			
Diffractometer	Bruker APEXII CCD Diffractometer		
Absorption correction	Multi-scanSADABS, Bunker2012		
No. of measured, independent and observed [I>2σ(I)] reflections	9540, 4263, 4133	17044, 3560, 3241	7552, 2000, 1867
R_{int}	0.026	0.033	0.021
(sin θ/λ)max (Å^{-1})	0.706	0.618	0.682
Refinement			
R[F^2> 2σ(F^2)], *wR(F^2)*, S	0.018, 0.041, 0.87	0.043, 0.113, 1.08	0.023, 0.057, 1.07
No. of reflections	4263	3560	2000
No. of parameters	246	267	112
No. of restrains	2	24	-
H-atom treatment	H atoms treated by a mixture of independent and constrained refinement	H-atom parameters constrained	H-atom parameters constrained
Δρmax.Δρ$_{min}$ (e Å^{-3})	1.03, −0.86	6.98, −0.98	1.45, −0.74

5.3 X-Ray Crystallography of Ligands

5.3.1 X-Ray structural analysis of H_2L6

Ligand H_2L6 crystallised in the tetragonal space group $P4_3$ as a monohydrate with the asymmetric unit containing two ligand molecules (Z = 8) and a single water molecule. A single molecule of the asymmetric unit is shown below in Figure 5.3.1. Key bond lengths and bond angles are summarised in Table 5.3.1. The two independent structures in the asymmetric unit are very similar, as indicated by the least square fit, which gives a root mean square deviation (RMSD) of 0.0804 Å.

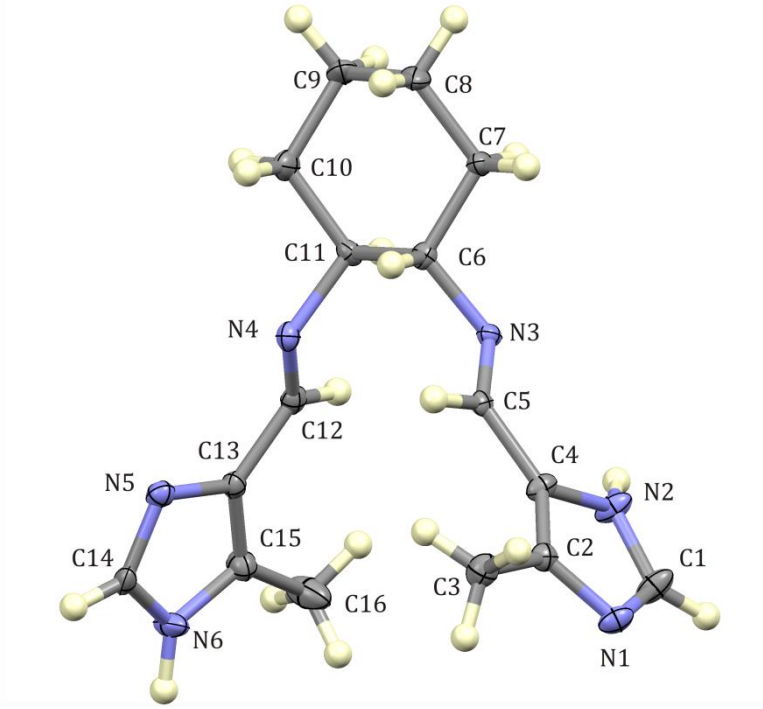

Figure 5.3.1: Thermal ellipsoid plot of H_2L6, shown at 50% probability level. All hydrogen atoms are represented as spheres arbitrary radius. A single molecule from the asymmetric unit is shown.

Table 5.3.1: Key bond lengths and bond angles for H_2L6.

Bond	Length(Å)	Bond	Angle(˚)
N1-C1	1.329(6)	N1-C1-N2	111.9(4)
N1-C4	1.396(6)	N1-C4-C5	121.3(4)
N2-C1	1.349(6)	N2-C2-C4	105.9(4)
N2-C2	1.379(6)	C4-N1-C1	104.6(4)
C4-C5	1.471(7)	N3-C5-C4	121.6(4)
C2-C4	1.360(7)	C1-N2-C2	107.4(4)
N3-C5	1.269(6)	C6-N3-C5	118.4(4)
N3-C6	1.470(6)		

The N3-C5 bond length (1.269(6)˚) coupled with the N3-C5-C4 bond angle which measures 121.6(4)˚ highlight the sp^2 hybridised nature of the imine nitrogen atom and illustrates the double bond character of the imine bond.

Comparing bond lengths, bond angles and torsion of H_2L6 with similar bonds found in previously reported ligands such as EFAROU, NANTUS and XUVQAG clearly shows good correlation.

The two ligand molecules in the asymmetric unit are similar in structure as illustrated by an RMSD = 0.0.791 Å. The key difference between the two molecules is the rotation of the imidazole-imine moieties relative to the six atom mean plane defined by the cyclohexyl rings. The angles between the 6-atom mean plane defined by the cyclohexyl ring and the two 8-atom mean planes defined by the methylimidazole and imine moieties measure 72.27 ˚ and 80.58 ° (mean = 76.42°). The equivalent angles for molecule B measure 71.51 and 84.25 ° (mean = 77.88 °).

The ligand H_2L6 exhibits a complex hydrogen bonded-network that stabilises a three-dimensional supramolecular structure. The three-dimensional network is stabilised by eight unique hydrogen bonds. The water molecule bridges two molecules (A and B) in the lattice to form a dimer. The water molecule acts as the hydrogen bond donor and the imine nitrogen atoms of molecules A and B as the hydrogen bond acceptors. This dimer is then further

stabilised by a hydrogen bond between the imidazole NH (H-bond donor) of molecule A and the imidazole N atom (H-bond acceptor) of molecule B as shown in Figure 5.3.2 below.

The hydrogen bond lengths and angles have been measured and reported below in Table 5.3.2.

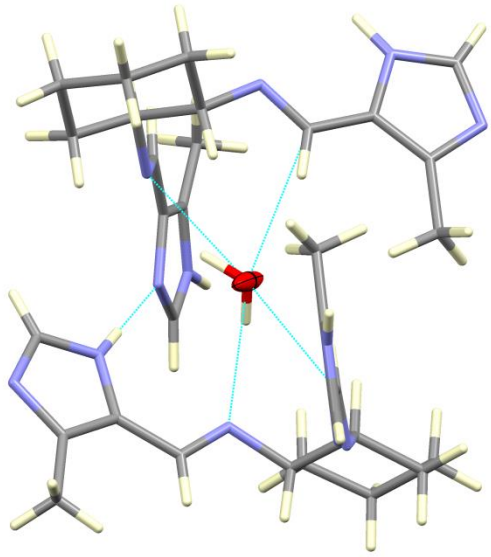

Figure 5.3.2: Solid state structure of H_2L6 illustrating the hydrogen-bonded dimer bridged by a water molecule. The dimers are linked by additional hydrogen bonding to form a three-dimensional supramolecular structure.

Table 5.3.2: Hydrogen bond lengths (Å) and bond angles (°) of H_2L6.

D-H···*A*	**D-H**	**H···*A***	**D···*A***	**D-H···*A***
O1W-H1W···N3	0.96(9)	2.04(8)	2.945(6)	155(7)
O1W-H1W···N9A	0.87(9)	2.11(9)	2.941(6)	160(9)
N7A-H7A···N1	0.84(5)	2.08(5)	2.921(6)	175(5)
N2-H2···N8A	0.96(7)	2.25(7)	2.854(6)	120(5)
N6-H6···N11A	0.98(7)	1.92(7)	2.891(5)	168(6)
N5···H12-N12A	0.83(5)	2.04(5)	2.855(5)	171(5)

In addition to bridging dimers within a column, the bridging ligand molecules cross-link the one dimensional columns of dimers leading to a two-dimensional hydrogen-bonded sheet. A single imidazole ring of the bridging molecule crosslinks dimers within the same column, stabilising the one-dimensional structure. The imidazole NH hydrogen bonds to the imidazole N atom of a single molecule in the dimer. The N-atom of the same bridging imidazole ring acts as an H-bond acceptor for the imidazole NH of an adjacent dimer. The second imidazole ring of the bridging

unit is H-bonded through the imidazole NH to the imidazole N atom of adjacent column. This stabilises the two-dimensional sheet.

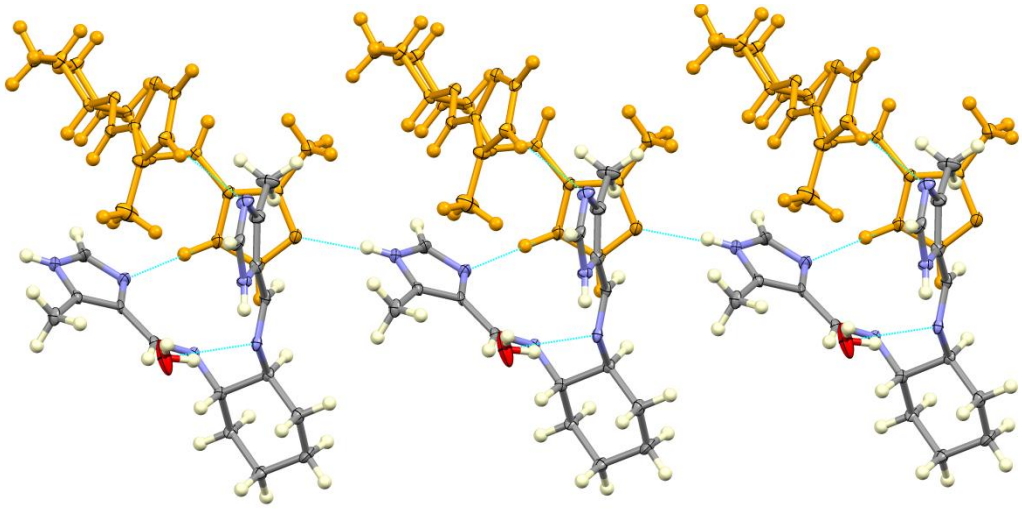

Figure 5.3.3: Cross-linking of adjacent dimers through hydrogen bonding between the imidazole NH and imidazole N atoms. The dimers (as illustrated in Figure 5.3.2) are shown in yellow.

The combination of the extended hydrogen bonding in H_2L6 in combination with the four fold symmetry of the tetragonal crystal system leads to very interesting columnar supramolecular structure. These columnar structures are highly cross-linked by intermolecular interactions. The structures are shown in Figure 5.3.4.

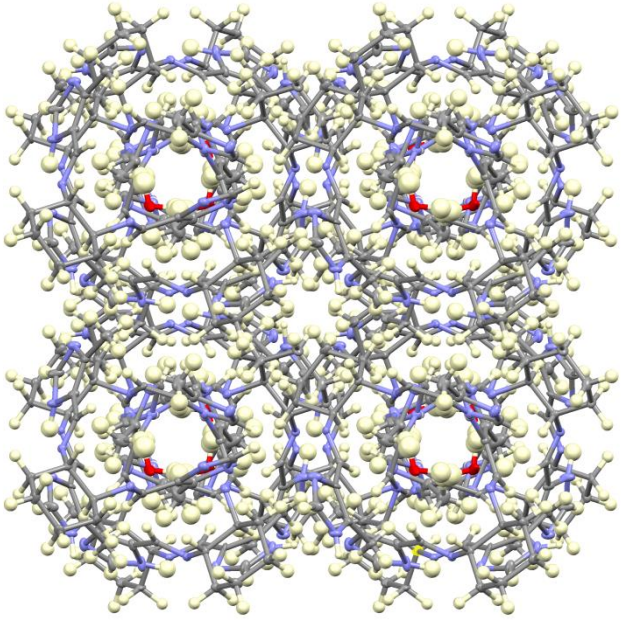

Figure 5.3.4: Cross-linked columnar structure of H_2L6 the result of a combination of hydrogen bonding and four-fold lattice symmetry. The structure is viewed down the *c*-axis.

The water molecules are found in the centre of the hydrogn-bonded columns and form hydrogen bonds with surrrounding molecules. The anti-configuration is needed for formation of the polymers. There hydrogen bonds from N1a to N2c extend the polymer down the *c*-axis and also form the circular shapes. The three dimensional polymer is a result of a repeating one dimension pattern along the *a*-axis.

5.3.2 X-Ray structural analysis of H_2L7

Ligand H_2L7 crystallised in the tetragonal space group *P4₁* with the asymmetric unit containing two independent molecules (Z = 8). The two independent ligand molecules in the asymmetric unit are similar in geometry as indicated by an RMSD of 0.2128 Å. A single molecule from the asymmetric unit is shown below in Figure 5.3.5.

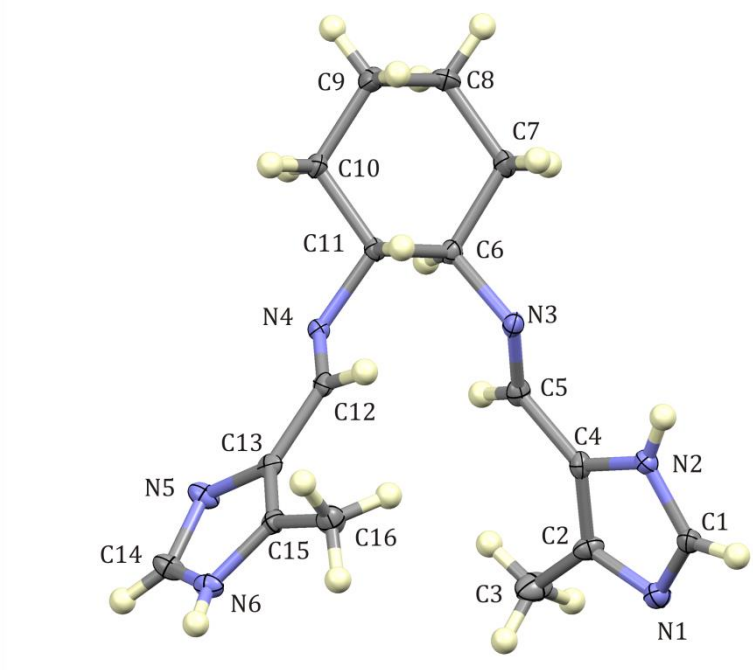

Figure 5.3.5: A thermal displacement plot of H_2L7 shown at 50% probability level. All hydrogen atoms are represented as spheres of arbitrary radius.

Bond lengths and bond angles describing the imidazole ring and imine moieties are summarised in Table 5.3.3. It is interesting to note that in both H_2L6 and H_2L7 the geometry about the imine bond is exclusively trans. This is ubiquitous in bis(pyrridyl-imine) and bis(pyrrolide-imine) Schiff base chelates. The cis configuration would lead to a greater level of non-bonded repulsion and destabilise the structures.

Table 5.3.3: Bond lengths and bond angles describing the imidazole ring and imine moieties of H_2L7.

Bond	Length (Å)	Bond	Angle (°)
N1-C1	1.319(4)	N1-C1-N2	112.7(3)
N1-C4	1.391(4)	N1-C4-C5	125.8(3)
N2-C1	1.352(4)	N2-C2-C4	105.9(3)
N2-C2	1.367(4)	C4-N1-C1	104.5(3)
C4-C5	1.458(4)	N3-C5-C4	125.5(3)
C2-C4	1.378(4)	C1-N2-C2	107.1(3)
N3-C5	1.271(4)	C6-N3-C5	115.4(2)
N3-C6	1.469(4)		

The data in the above table clearly shows that the imine bond is once again significantly shorter than the remaining bonds. This is indicative of the double bond character.

When comparing bond lengths of H_2L7 with similar bond lengths, bond angles and torsion angles in the related compounds EFAROU, NANTUS and XUVQAG and XUVQAG it is noted that there is a particularly good correlation with NANTUS.

The two ligand molecules in the asymmetric unit are similar in structure as illustrated by a root-mean-square deviation (least squares fit) of the two molecules, RMSD = 0.1103 Å. The key difference between the two molecules is the rotation of the imidazole-imine moieties relative to the six atom mean plane defined by the cyclohexyl rings. The angles between the 6-atom mean plane defined by the cyclohexyl ring and the two 8-atom mean planes defined by the methylimidazole and imine atoms measure 72.27 and 80.58 ° (mean = 76.42°). The equivalent angles for molecule B measure 71.51 and 84.25 ° (mean = 77.88 °).

The ligand H_2L7 exhibits a complex hydrogen-bonded network that stabilises a three-dimensional supramolecular structure. The three-dimensional network is stabilised by five unique hydrogen bonds. The water molecule bridges two molecules (A and B) in the lattice to form a dimer. The water molecule acts as the hydrogen bond donor and the imine nitrogen atoms of molecules A and B as the hydrogen bond acceptors. This dimer is then further

stabilised by a hydrogen bond between the imidazole NH (H-bond donor) of molecule A and the imidazole N atom (H-bond acceptor) of molecule B as shown in Figure 1 below.

The hydrogen bond lengths and angles have been measured and reported below in Table 5.3.3 and the resulting supramolecular structure illustrated in Figure 5.3.6.

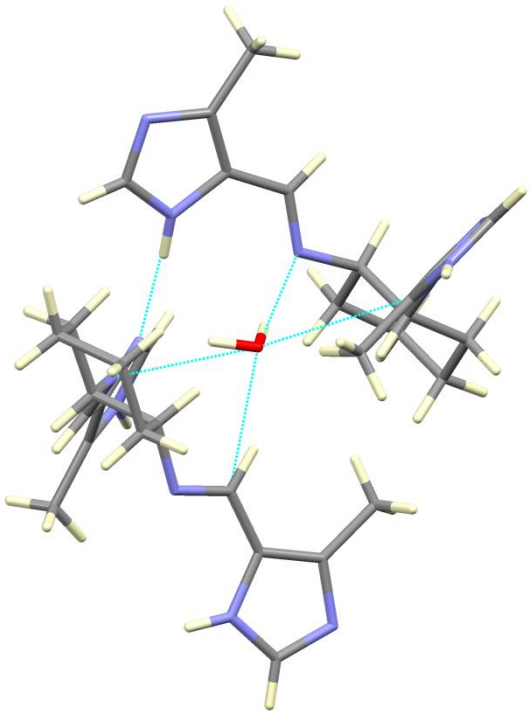

Figure 5.3.6: Solid state structure of H_2L7 displaying dimeric structure stabilised by hydrogen bonds.

Table 5.3.4: Hydrogen bond lengths (Å) and bond angles (˚) of H_2L7.

D-H···*A*	**D-H**	**H···*A***	**D···*A***	**D-H···*A***
O1W-H1W···N6	0.80(5)	2.16(5)	2.929(4)	163(5)
O1W-H1W···N12A	0.90(6)	2.11(6)	2.939(4)	153(3)
N8-H8···N1	0.86(4)	2.05(4)	2.885(4)	162(4)
N9-H9···N3	0.91(4)	2.16(4)	2.858(4)	132(4)
N2-H2···N7	0.83(3)	2.03(3)	2.851(4)	171(3)
N10···H4-N4	0.86(4)	2.06(4)	2.918(4)	174(3)

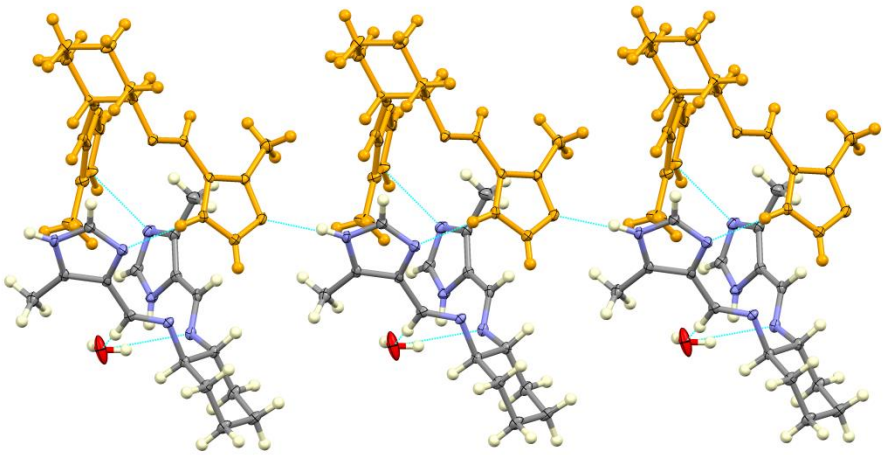

Figure 5.3.7: Cross-linking of adjacent dimers through hydrogen between the imidazole NH and imidazole N atoms. The dimers (as illustrated in Figure 5.3.6) are shown in yellow. This hydrogn bonding motif leads to one dimensional columns.

In addition to bridging dimers within a column, the bridging ligand molecule cross-links the one dimensional columns of dimers leading to a two-dimensional hydrogen-bonded sheet. A single imidazole ring of the bridging molecule crosslinks dimers within the same column, stabilising the one-dimensional structure. The imidazole NH hydrogen bonds to the imidazole N atom of a single molecule in the dimer. The N-atom of the same bridging imidazole ring acts as an H-bond acceptor for the imidazole NH of an adjacent dimer. The second imidazole ring of the bridging unit is H-bonded through the imidazole NH to the imidazole N atom of and adjacent column. This stabilises the two-dimensional sheet.

As with H_2L6, the combination of four-fold lattice symmetry associated with the tetragonal crystal system in conjunction with the extended hydrogen bonding leads to a highly symmetrical columnar supramolecular structure as shown in Figure 5.3.8.

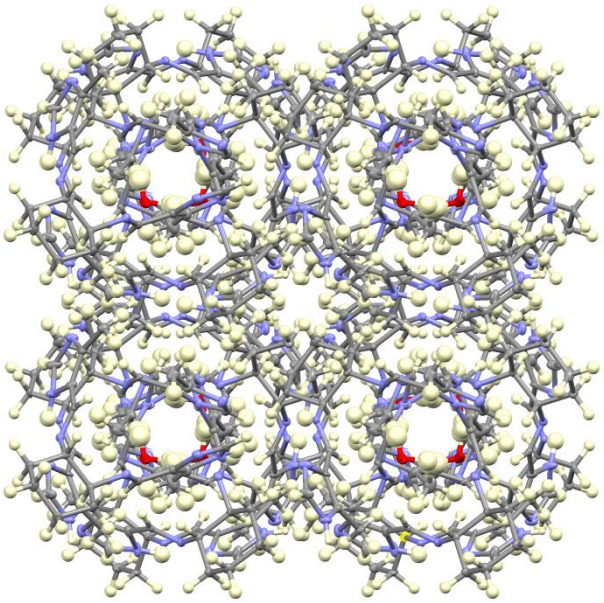

Figure 5.3.8: Columnar structure of H_2L7 viewed down the *c*-axis. The structure is stabilised by extensive hydrogen bonding.

The water molecules are found in the centre of the columns (Figure 5.3.8) and form hydrogen bonds with surrrounding molecules. The anti-configuration is needed for formation of the polymers. The hydrogen bonds from N1a to N2c extend the polymer down the *c* axis and also form the columnar structures. The three dimensional polymer is a result of a repeating one-dimension pattern along the *a*-axis.

5.4 X-Ray Crystallography of Complexes

5.4.1 X-Ray structural analysis of [Au(L1)][PF_6]

Ligand [Au(L1)][PF_6] crystallised in the monoclinic, *Cc* space group with the asymmetric unit containing one molecule (Z=4). The single molecule in the asymmetric unit is seen below in Figure 5.4.1.

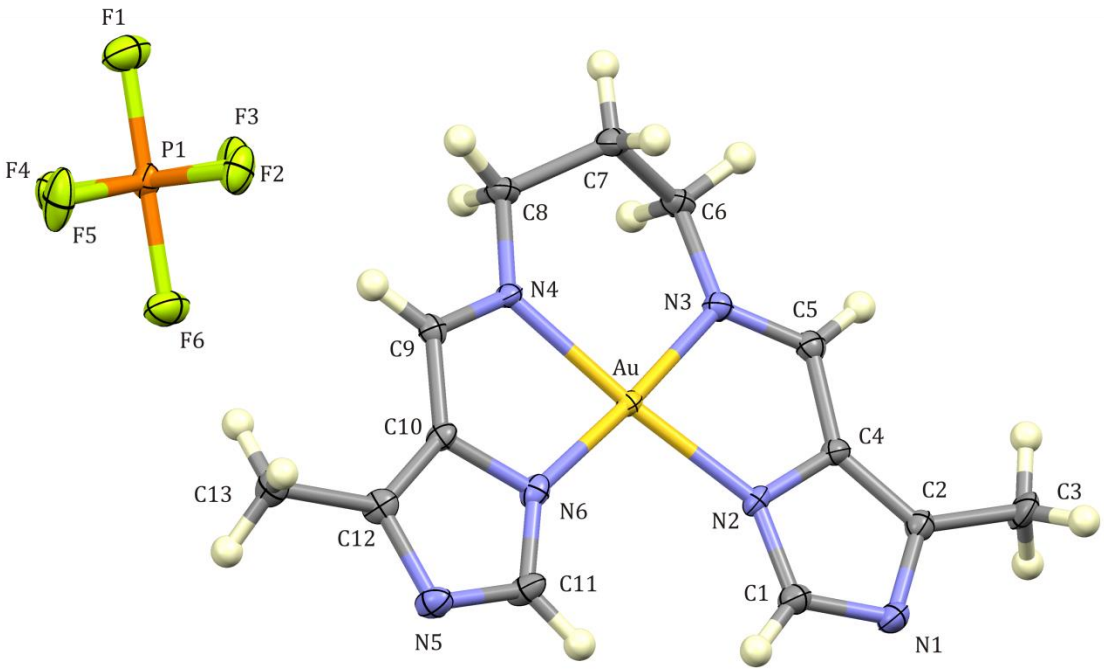

Figure 5.4.1: A labelled thermal displacement plot of [Au(L1)][PF_6], shown at 50% probability level. All hydrogen atoms are represented as spheres of arbitrary radius.

Chelate [Au(L1)][PF_6] exhibits a square planar coordination geometry, coordinated by the four nitrogen atoms, two imine nitrogen atoms and two imidazole nitrogen atoms. Metal ion chelation has occurred with concomitant deprotonation of the imidazole NH groups yielding a dianionic ligand and monocationic chelate isolated as the hexafluorophosphate(V) salt. This is an interesting result as all previous examples of related ligands coordinated to divalent 3d transition metals show metal chelation without NH deprotonation. This illustrates the electron deficient nature of the gold(III) ion and the necessity of strong anionic sigma-donor atoms to stabilise the metal centre.

The bond lengths and bond angles describing the coordination sphere are summarised below in Table 5.4.1.

Table 5.4.1: Bond lengths and bond angles describing the coordination sphere of [Au(L1)][PF_6].

Bond	Length(Å)	Bond	Angle (°)
N2-Au	2.005(3)	N2-Au-N3	80.6(1)
N3-Au	2.013(3)	N2-Au-N6	103.0(1)
N4-Au	2.022(3)	N4-Au-N3	95.7(1)
N6-Au	1.995(4)	N4-Au-N6	80.7(1)

The average Au-N_{imine} (N3 and N4) bond length measures 2.0175(4) Å which is consistent with the imine bond lengths reported in RIZHAL, RIZHEP and RIZHIT. The average Au-$N_{imidazole}$ (N2 and N6) bond length measures 2.000 (4) Å which is consistent with the imine bond lengths reported in RIZHAL, RIZHEP and RIZHIT. The shorter bond length reported for the latter could be attributed to a stronger interaction between the gold(III) ion and the negatively charged imidazole N atom. The mean N_{imine}-Au-N_{imine}, mean N_{imine}-Au-$N_{imidazole}$ and $N_{imidazole}$-Au-$N_{imidazole}$ bond angels measure 95.7(1)°, 80.65(1)° and 103.0(1)°, respectively. These bond angles have an excellent correlation with the bond angles reported in RIZHAL, RIZHEP and RIZHIT. The bridging unit shows the characteristic out-of-plane distortion required to accommodate the sp^3 hybridised carbon atoms. The variation in the bond angles describing the coordination sphere is due to the differing bite of the tetradentate ligand. The bond angle associated with the five-membered chelate rings is more acute than that of the six-membered ring. The $N_{imidazole}$-Au-$N_{imidazole}$ bond angle is the most obtuse as the imidazole rings are free to move apart, which would reduce no-bonded repulsion between the imidazole CH atoms.

The solid state structure of [Au(L1)][PF_6] also exhibits interactions between the electron deficient gold(III) ion and the imidazole N-atom of an adjacent molecule as shown in Figure 5.4.2. This interaction would serve to further stabilise the gold(III) ion in its high oxidation state. The distance of this interaction is 2.811(3) Å between the imidazole ring nitrogen atom and gold(III) ion of the adjacent complex. This interaction is significantly shorter than the sum of the van der Waals radii of the interacting atoms (by 0.399 Å) this suggests that the interaction is significant. This interaction is due to the electron deficient gold(III) ion which accepts electron density from adjacent aromatic systems which can be defined as Lewis acid/base interaction. Closely related Au-π interactions are known to stabilise DNA/chelate conjugates in the DNA intercalation process.

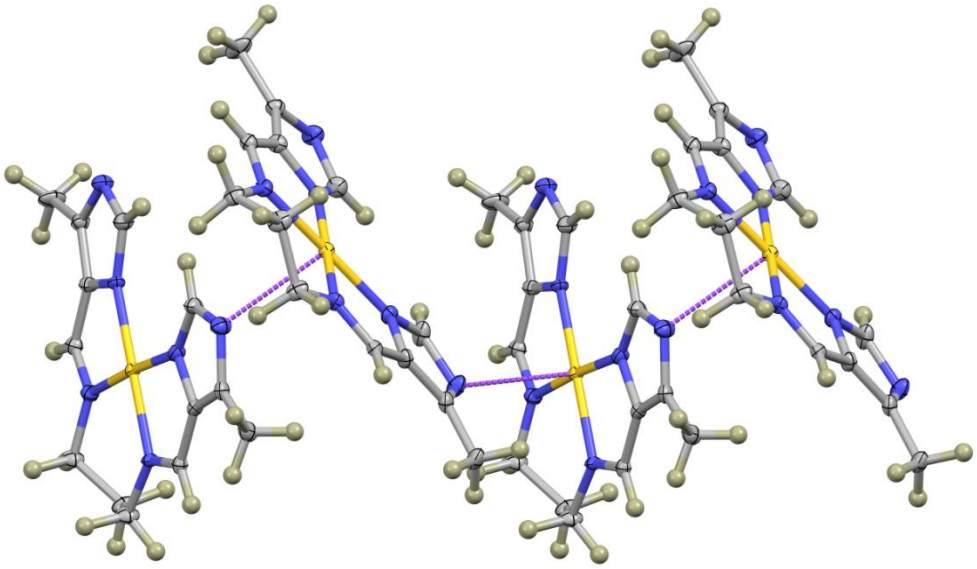

Figure 5.4.2: Au···N interactions of [Au(L1)](PF_6) measuring 2.811(3) Å link adjacent molecules to form a one-dimensional chain co-linear with the *c*-axis.

5.3.2 X-Ray structural analysis of [Au(L2)][PF_6]

The complex [Au(L2)][PF_6] crystallised in the monoclinic, $P2_1/c$ space group with the asymmetric unit containing one molecule (Z=4). The single molecule in the asymmetric unit is shown below in Figure 5.4.3.

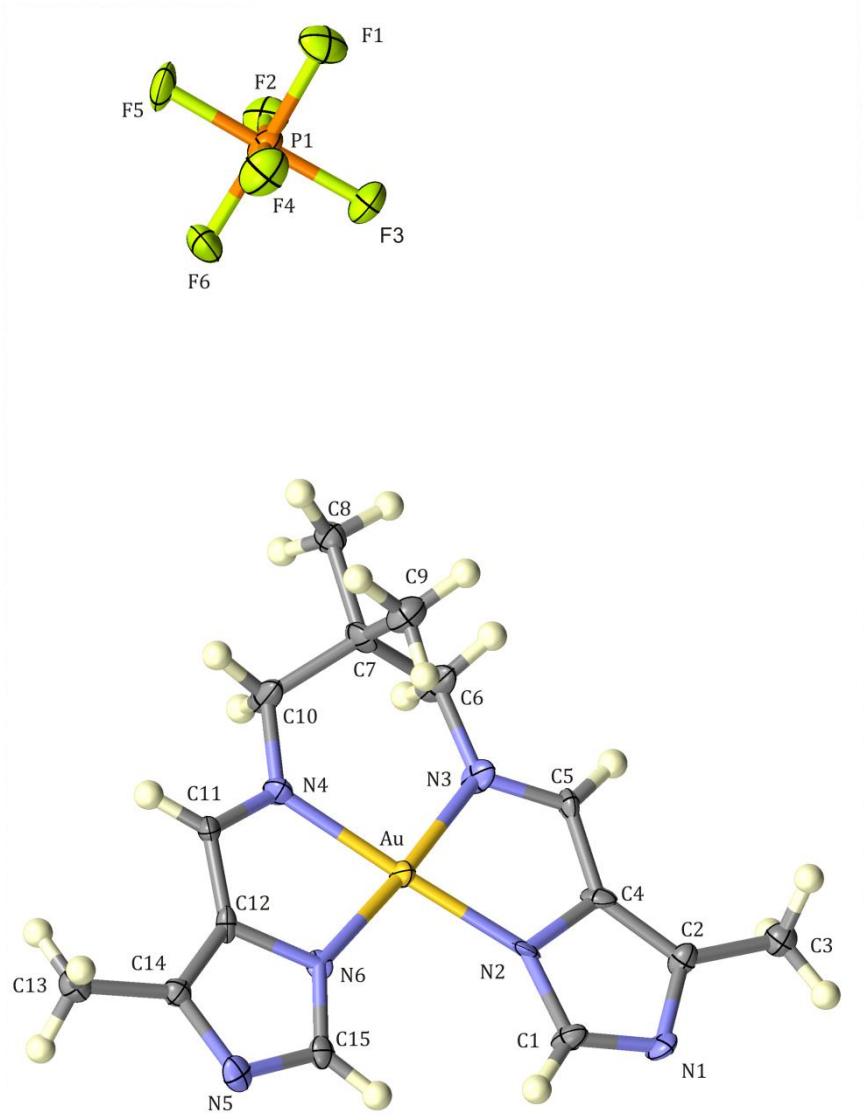

Figure 5.4.3: A thermal ellipsoid plot of [Au(L2)][PF_6]. It has been rendered at the 50% probability level. All hydrogen atoms are represented as spheres with indiscriminate radii.

Chelate [Au(L2)][PF_6] exhibits a square planar geometry and is chelated *via* the four nitrogen atoms, two imine nitrogen atoms and two imidazole nitrogen atoms. The bond lengths and bond angles describing the coordination sphere of the gold(III) ion with the nitrogen atoms are summarised below in Table 5.4.2.

Table 5.4.2: Bond lengths and bond angles describing the coordination sphere of [Au(L2)][PF_6].

Bond	Length(Å)	Bond	Angle (°)
N2-Au	2.009(7)	N2-Au-N3	80.5(3)
N3-Au	2.019(7)	N2-Au-N6	102.4(4)
N4-Au	2.003(7)	N4-Au-N3	95.5(3)
N6-Au	1.966(7)	N4-Au-N6	81.6(3)

The average Au-N_{imine} (N3 and N4) bond length measures 2.000(10) Å which is consistent with the equivalent bond lengths reported in RIZHAL, RIZHEP and RIZHIT and [Au(L1)]PF_6. The average Au-$N_{imidazole}$ (N2 and N6) bond length measures 1.984(10) Å which is consistent with the imine bond lengths reported in RIZHAL, RIZHEP and RIZHIT. The shorter bond length reported for the latter could be attributed to a stronger interaction between the gold(III) ion and the negatively charged imidazole N atom. The bond angles for N_{imine}-Au-N_{imine}, average N_{imine}-Au-$N_{imidazole}$ and $N_{imidazole}$-Au-$N_{imidazole}$ measures 95.5(3)°, 81.08(4)° and 102.4(4)°, respectively. These bond angles have an excellent correlation with the bond angles reported in RIZHAL, RIZHEP and RIZHIT and [Au(L1)]PF_6. The bridging unit again shows the same out-of-plane distortion, consistent with RIZHAL and RIZHEP. The structure shows an Au···π interaction between the gold(III) ion and the imidazole ring of an adjacent molecule.The distance of the Au···π interaction is 3.210(1). Interactions of this nature are common in gold(III) chelates and provide insight into why gold(III) complexes typically interact strongly with the highly aromatic DNA base pairs *in vivo*.

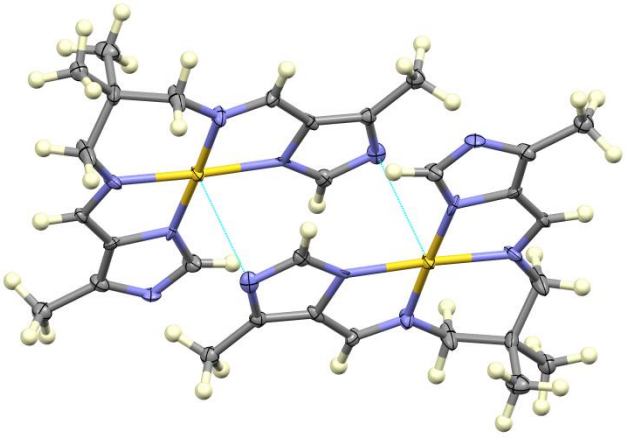

Figure 5.4.4: Au···N interactions of [Au(L2)](PF_6) with an interaction distance measuring 3.21(1) Å.

5.3.3 X-Ray structural analysis of [Au(L4)][PF_6]

Ligand [Au(L4)][PF_6] crystallised in the monoclinic, *C2/c* space group with the asymmetric unit containing half a molecule (*Z*=4). The single molecule is shown below in Figure 5.4.5. For clarity, only one C7 and hydroxyl group is shown. Bond lengths and bond angles describing the coordination sphere are shown in Table 5.4.3.

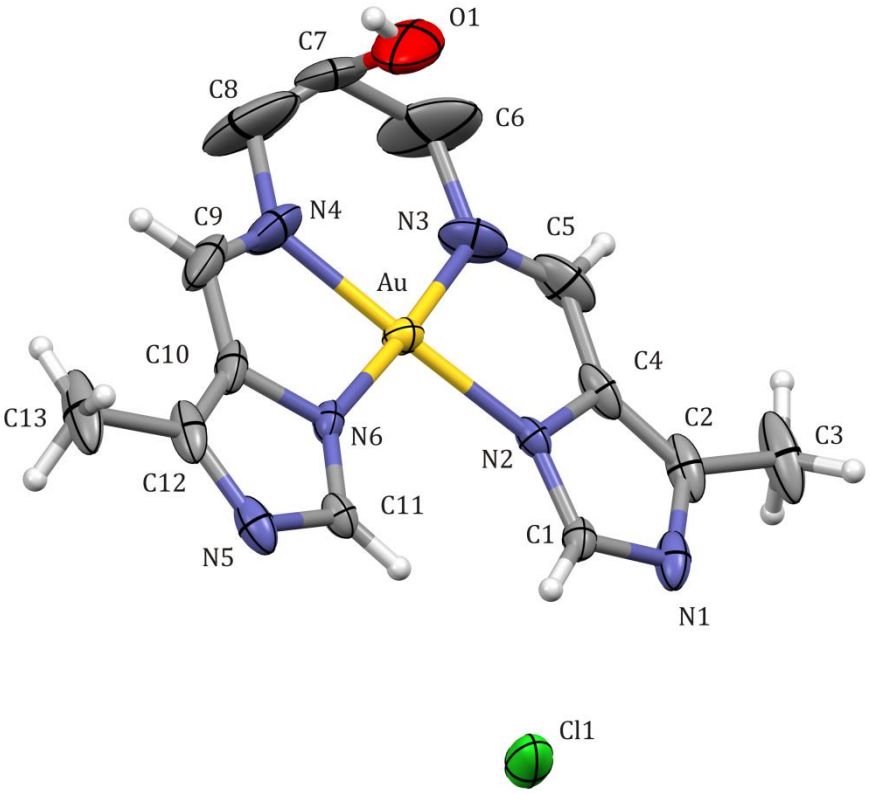

Figure 5.3.5: A thermal ellipsoid plot of [Au(L4)]Cl shown at 50% probability level. All hydrogen atoms are represented as spheres with indiscriminate radius.

Chelate [Au(L4)]Cl exhibits a square planar geometry and is chelated *via* the four nitrogen atoms, two imine nitrogen atoms and two imidazole nitrogen atoms. This geometry is consistent with other gold(III) chelates and is a result of the d8 electronic configuration and the associated vacant dx^2-y^2 orbitals.

Table 5.4.3: Bond lengths and angles for [Au(L4)][PF_6].

Bond	Length(Å)	Bond	Angle (°)
N2-Au	1.996(3)	N2-Au-N3	80.86(17)
N3-Au	2.003(4)	N2-Au-N6	102.84(17)
N4-Au	2.003(4)	N4-Au-N3	95.49(3)
N6-Au	1.996(3)	N4-Au-N6	80.86(17)

The average Au-N_{imine} (N3 and N4) bond length is 2.003(6) Å which is consistent with the equivalent bond lengths reported in RIZHAL, RIZHEP and RIZHIT. The average Au-$N_{imidazole}$ (N2 and N6) bond length measures 1.996(4) Å which is consistent with the equivalent bond lengths reported in RIZHAL, RIZHEP and RIZHIT. The bond angles for N_{imine}-Au-N_{imine} , N_{imine}-Au-$N_{imidazole}$ and $N_{imidazole}$-Au-$N_{imidazole}$ measures 95.49(3)°, 80.86(24)° and 102.84(17)°, respectively. The variation in the bond angles is, as before, attributed to the varying bite of the ligand and the resulting five- and six- membered chelate rings. The free $N_{imidazol}$-Au-$N_{imidazole}$ bond length is not resticted by the ligand structure and is therefore significantly more obtuse than the other bond angles.

5.4 Conclusions

Two ligands and three gold(III) chelates were studied by single crystal X-ray diffraction. The two ligands crystallised as the hemihydrate (i.e. a single water molecule associated with the two independent ligand molecules in the asymmetric unit. This allowed for hydrogen bonding. The D···A distances range from 2.921 to 2.945 Å and the D-H···A bond angles range from 155.27 to 174.94°. The hydrogen bonding allowed for formation of very interesting columnar structures.

The three gold(III) chelates all had a square planar coordination geometry. Metalation required depronation of the imidazole NH resulting in a dianionic tetradentate N_4-donor ligand and a cationic chelate. The imine nitrogen donor was found to have a longer bond to the gold(III) ion than the anionic imidazole nitrogen. The mean Au-N_{imine} and Au-$N_{imidazole}$ bond lengths measure 2.007 Å and 1.993 Å, respectively. Au···π interactions are present in two chelates which serves as an indication that potential chelate/DNA interactions are favourable.

5.5 References

(1) Cambridge Crystallographic Data Centre 12 Union Rd, Cambridge CB21EZ, UK 2010.

(2) van den Ancker, T.; Cave, G.; Raston, C. Benign Approaches For The Synthesis Of Bis-Imine Schiff Bases. *ChemInform* **2006**, 37.

(3) Bacchi, A.; Carcelli, M.; Gabba, L.; Ianelli, S.; Pelagatti, P.; Pelizzi, G.; Rogolino, D. Syntheses, Characterization And X-Ray Structure Of Palladium(II) And Nickel(II) Complexes Of Tetradentate Pyrrole Containing Ligands. *Inorg. Chim.* Acta., **2003**, 342, 229-235.

(4) Akerman, K. (1 R* ,2 S *)- *N* , *N'*-Bis[(*E*)-1 *H* -Pyrrol-2-ylmethylidene] Cyclohexane-1,2-Diamine Monohydrate. *Acta Cryst. E.,* **2012**, 68, o3354-o3355.

(5) Yathirajan, H.; Raju, C.; Rai, K.; Jailakshmi, K.; Nagaraja, P.; Palani, K.; Ponnuswamy, M.; Nethaji, M. Crystal Structure Of Bis(2-Butyl-4-Chloro-Imidazole)5-Iminoethane. J. Chem. Crystallogr., **2005**, 35, 211-215.

(6) Akerman, K.; Fagenson, A.; Cyril, V.; Taylor, M.; Muller, M.; Akerman, M.; Munro, O. Gold(III) Macrocycles: Nucleotide-Specific Unconventional Catalytic Inhibitors Of Human Topoisomerase I. *J. Am. Chem. Soc*., **2014**, 136, 5670-5682.

(7) Rossignoli, M.; Bernhardt, P.; Lawrance, G.; Maeder, M. Gold(III) Template Synthesis Of A Pendant-Arm Macrocycle*. J. Chem. Soc., Dalton Trans*. **1997**, 323-328.

(8) Afanas'eva, V.; Glinskaya, L.; Klevtsova, R.; Mironov, I.; Sheludyakova, L.; Tkachev, S. *J. Struct. Chem.,* **2003**, 44, 68-73.

(9) Domínguez-Vera, J.; Rodríguez, A.; Cuesta, R.; Kivekäs, R.; Colacio, E*. J. Chem. Soc., Dalton Trans.* **2002**, 561-565.

(10) Hou, Y.; Li, S.; Sun, R.; Liu, X.; Weng Ng, S.; Li, D. *Dalton Trans*. **2015**, 44, 17360-17365.

(11) Mimura, M.; Matsuo, T.; Nakashima, T.; Matsumoto, N. *Inorg. Chem.,* **1998**, 37, 3553-3560.

Chapter 6| Computational Studies

6.1.1 Introduction

Wavefunctions can generally be used to generate data in electronic structure simulations. A wavefunction is a mathematical expression describing the probability of finding an electron in a certain location as the exact position cannot be precisely known [1]. Solving a wavefunction is only possible for single electron atoms such as hydrogen, an alternative method for more chemically relevant systems is therefore required. Density Functional Theory (DFT) is an indirect way of calculating the wavefunction of an atom or molecule. It relies on the ground state electronic function of a molecule which can be determined, the wavefunction can then be approximately solved based on the calculated electron distribution of a molecule [2,3]. Physical characteristics such as optimised geometries, vibrational frequencies, electronic transitions and NMR data can be calculated once the wavefunction is determined.

DFT simulations require the application of both a basis set and density functional. The basis set is the set of atomic functions that describes the number and type of atomic orbitals used and the region in space to which the electron is restricted [2,3]. The larger the basis set, i.e. the fewer restrictions that are placed on an electrons, the more computationally expensive. However, larger basis sets tend to give more reliable results. The density functional used for all complexes is PBE1PBE [4,5] which is a gradient corrected functional, meaning it uses electron spin densities and their gradients [1]. A functional is a mathematical entity which produces an instruction from a set of coordinates or variables; it is in essence a function of a function. The basis set LanL2DZ (Los Alamos National Laboratory 2-double-zeta) was used for all complexes because it can be used for atoms in the range of H, Li-Ba, La-Bi. LanL2DZ makes use of effective core potentials. Since second and third row elements of the Periodic Table have very large numbers of electrons it can become computationally too demanding to explicitly include these electrons in the simulations. When an effective core potential is applied, it is assumed that the core electrons do not play a significant role in the bonding and physico-chemical properties of molecules and they are therefore replaced with a single electronic potential. The valence electrons are still included [1, 6, 7, 8, 9].

Ligand calculations made use of B3LYP (Beck, 3-parameter, Lee-Yang-Parr) density functional. This method considers proton affinities, total energies and ionization potentials. The basis set

used for ligand calculations as 6-311G which applies to atoms from H to Kr and implicitly includes all electrons [10, 11].

6.1.2 Previous computational studies on related compounds

The following contains basic details of select molecular simulation studies on compounds related to the bis(imidazole-imine) compounds in this work. The survey was primarily used to gauge the most appropriate basis sets and functionals to apply in the present study. Previous DFT studies have been carried out on bidentate pyrrolide-imine compounds related to the bis(imidazole-imine) ligands synthesised in this study [19]. The previous studies were undertaken to determine the geometric optimisations, vibrational frequency and electronic transitions. The calculations were performed at the B3LYP/6-311G(d,p) level of theory [19]. The general structure of the ligands is shown below in Figure 6.1.1.

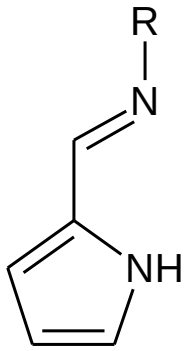

Figure 6.1.1: The general structure of the pyrrolide-imine Schiff base ligands previously studied by DFT methods.

The results of these molecular simulations were in excellent agreement with the experimental data and allowed for a deeper understanding of the experimental results. Of particular interest, the relative energies of the optimised structures and solid state structures were probed. This gave insight into the effects of the solid-state interactions on the geometries of the free ligands. The electronic spectra and the orbitals involved in the electronic transitions were also simulated. These data were accurately simulated and highlight the suitability of the chosen level of theory for the present study.

The following contains basic details of previously reported molecular simulation studies on compounds related to the gold(III) chelates in this work. The survey was primarily used to

gauge the most appropriate basis sets and functionals to apply in the present study as well as to determine the diversity of previous studies. Previous DFT studies have been carried out on bidentate pyridylamido gold(III) chelates [20,21]. In general either the LanL2DZ basis set or the split basis set which applies LanL2DZ to the gold(III) ion and 6-311G to all other atoms are used[20,21]. Similar to the above, geometry optimisations were performed as well as electronic transitions to help deconvolute the experimental data.

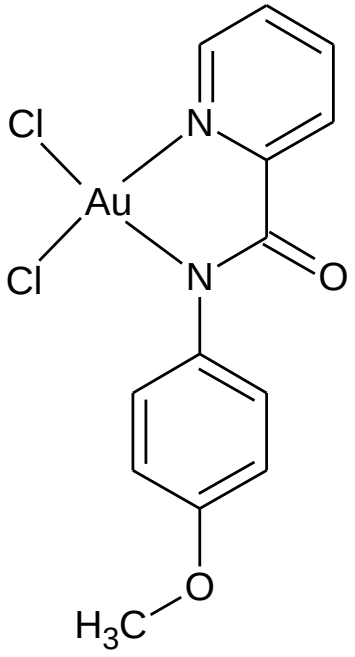

Figure 6.1.2.2: The structure of the pyridylamido gold(III) chelate previously studied by DFT methods.

As well as the DFT studies mentioned above, previous work has also made use of molecular mechanics simulations to probe the interactions of gold(III) chelates with DNA. [21] This enabled Akerman et al. to determine base pair specificity for the binding site of the gold(III) chelate. Molecular mechanics is suited for this type of research as it is more computationally economical than DFT and allows for the stimulation of biomolecules such as DNA. This will be a future avenue of research for the present project.

6.2 Computational method

All DFT calculations were performed with Gaussian 09W [22]. X-ray coordinates were used as input structures where possible and the input files were created using GuassView 5.0 [23]. For all calculations, there were no symmetry constraints imposed. All ligand simulations were performed at the B3LYP/6-311G(d,p) level of theory. For added accuracy single first polarization functions (d,p) were added. The basis set LanL2DZ (Los Alamos National Laboratory 2-double-zeta) and PBE1PBE was used for all complexes. For electronic transition energies the TD-DFT method was used [12, 13, 14, 15, 16, 17, 18].

6.3 Results and discussion

6.3.1 Gold(III) chelates

Geometry Optimisation Results

The geometry-optimised structure i.e., the lowest energy structure was calculated for all gold(III) chelates using the PBE1PBE/LanL2DZ level of theory. The DFT-calculated structures were then compared to the experimentally determined X-ray structures where possible to determine accuracy of the molecular simulations. The calculations were conducted in the gas phase with no intermolecular interactions considered. The X-ray structure will have a slightly more distorted square planar geometry due to π-π interactions between adjacent molecules, the DFT calculated structure will not experience the same π-π interactions meaning there will be no distortions from the lowest energy geometry. A summary of the bond lengths and bond angles for the experimental and calculated structures is shown in Table 6.3.1.

Figure 6.3.1 shows the is the least-squares fit for the calculated and experimentally X-ray structures of $[Au(L1)]^+$, $[Au(L2)]^+$ and $[Au(L4)]^+$. The overlays of the structures are almost identical as indicated by the small value of the root-mean-square deviations (RMSDS) of 0.1518, 0.0791 and 0.3149 Å, respectively. The blue structure represents the X-ray structure and the yellow represents the DFT-calculated structure.

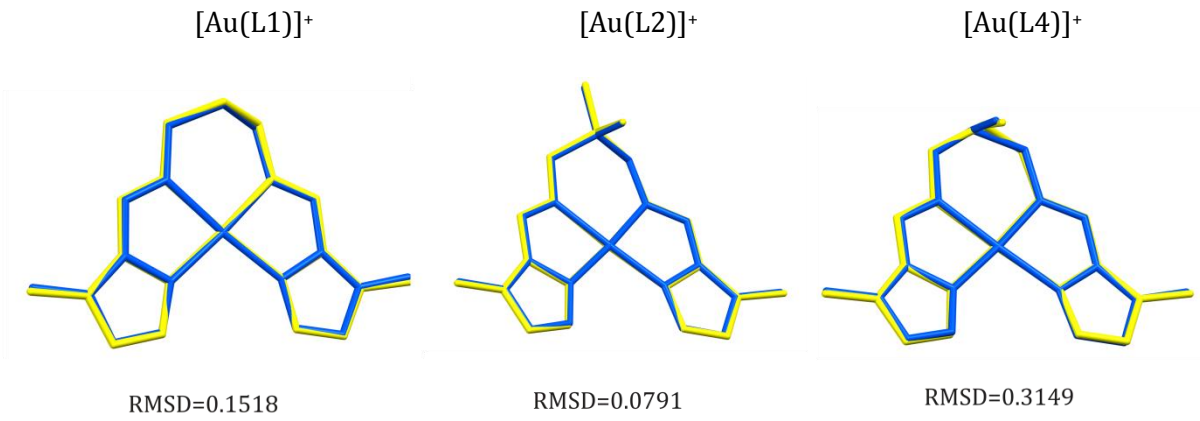

Figure 6.3.1: Least-squares fit for the DFT calculated and X-ray structures for $[Au(L1)]^+$, $[Au(L2)]^+$ and $[Au(L4)]^+$. The RMSDs are indicated for each molecule on the diagram (measured in Å).

The low RMSDs indicated above show that the calculated structures are in good agreement to the experimental structures determined by single crystal X-ray diffraction. This suggests that the level of theory used is appropriate and that the calculated structures of $[Au(L9)]^+$ and $[Au(L10)]^+$ are likely to be accurate representations of the experimental structures. The calculated structures of $[Au(L9)]^+$ and $[Au(L10)]^+$ are shown below in Figure 6.3.2.

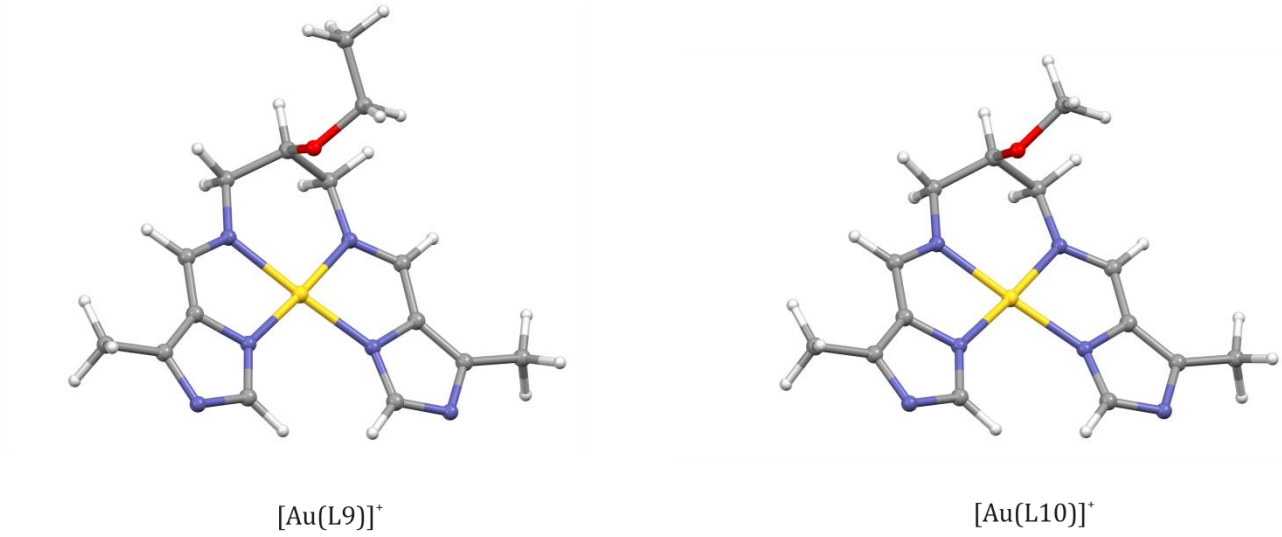

Figure 6.3.2: DFT calculated structures for $[Au(L9)]^+$, $[Au(L10)]^+$.

The DFT-simulated structures in Figure 6.3.2 show the same square planar coordination geometry as exhibited by the experimental X-ray structures. The bridging unit also shows the same characteristic out-of-plane distortion to accommodate the sp^3 hybridised carbon atoms.

Table 6.3.1: Summary of DFT-calculated and experimental bond lengths, bond angles and torsion angles of $[Au(L1)]^+$, $[Au(L2)]^+$ and $[Au(L4)]^+$.

	Structural Feature	Calculated	Experimental	% Difference
$[Au(L1)]^+$	*Bond Lengths/Å*			
	$Au\text{-}N_{imdazole}$	2.038	2.000	1.90
	$Au\text{-}N_{imine}$	2.070	2.018	2.60
	Bond Angles/ °			
	$N_{imdazole}\text{-}Au\text{-}N_{imdazole}$	102.72	103.00	0.27
	$N_{imdazole}\text{-}Au\text{-}N_{imine}$	96.52	95.70	0.86
	$N_{imine}\text{-}Au\ N_{imine}$	80.37	80.70	0.41
$[Au(L2)]^+$	*Bond Lengths/Å*			
	$Au\text{-}N_{imdazole}$	2.039	1.984	2.77
	$Au\text{-}N_{imine}$	2.068	2.000	3.40
	Bond Angles/ °			
	$N_{imdazole}\text{-}Au\text{-}N_{imdazole}$	102.99	102.37	0.02
	$N_{imdazole}\text{-}Au\text{-}N_{imine}$	95.99	95.54	0.47
	$N_{imine}\text{-}Au\ N_{imine}$	80.49	81.59	1.35
$[Au(L4)]^+$	*Bond Lengths/Å*			
	$Au\text{-}N_{imdazole}$	2.037	1.996	2.05
	$Au\text{-}N_{imine}$	2.067	2.003	3.20
	Bond Angles/ °			
	$N_{imdazole}\text{-}Au\text{-}N_{imdazole}$	102.61	102.84	0.22
	$N_{imdazole}\text{-}Au\text{-}N_{imine}$	96.61	95.49	1.17
	$N_{imine}\text{-}Au\ N_{imine}$	80.39	80.86	0.58

*Percentage difference $= \frac{|calc-Exp|}{Exp}\ x\ 100$

The calculated and experimental data show very good correlation. The percentage difference is relatively low with the highest being 3.40%. This suggests that the level of theory used is appropriate and the calculated data is reliable. In general, the bond angles of the coordination sphere are particularly well estimated. This is likely because the reduced degrees of freedom afforded by the ligand through metal ion chelation allows for simpler calculation of the bond angles.

Vibrational Frequency Data

The vibrational frequencies for the gold(III) complexes were calculated from the geometry optimized structures at the PBEPBE/LanL2DZ level of theory. It could be concluded that all structures were optimized to an energy minimum as no negative Eigen values were obtained. As a representative example, the experimental results obtained for complex [Au(L2)](PF_6) will be compared to those simulated for $[Au(L2)]^+$. The remaining chelates show a similar trend and have been omitted to avoid repetition. The calculated IR plot is compared to the experimental IR plot for $[Au(L2)]^+$ is shown below in figure 6.3.3.

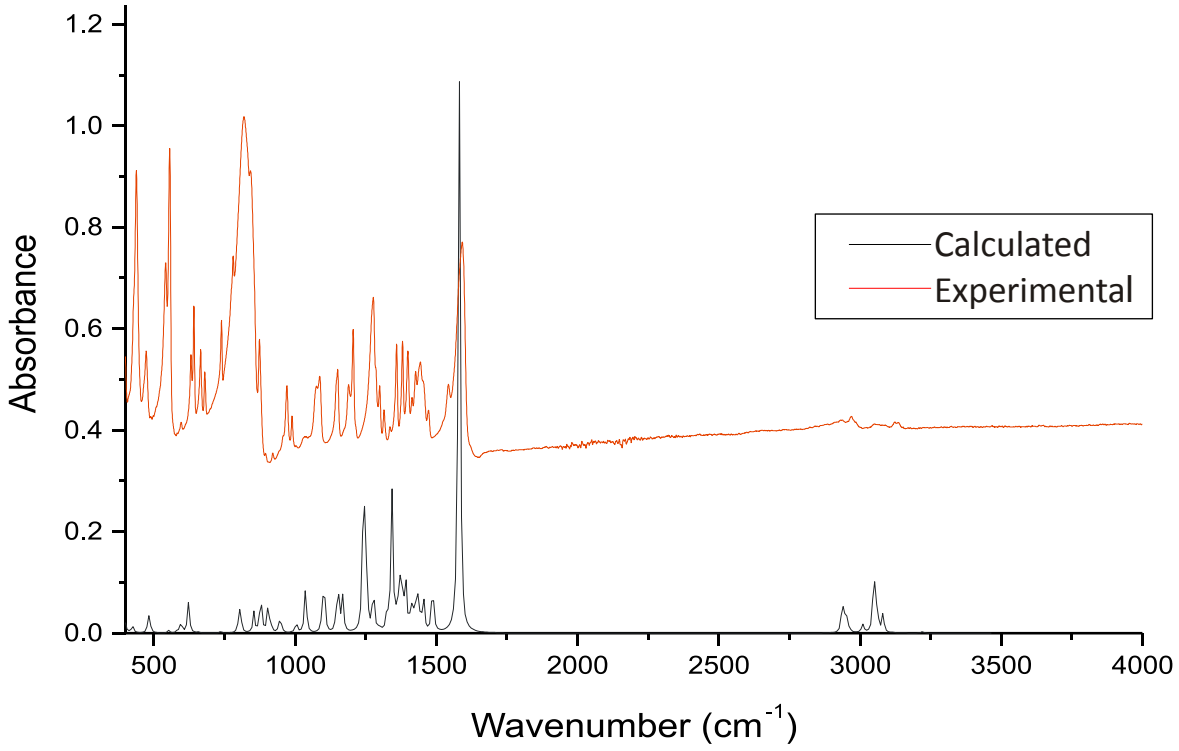

Figure 6.3.3: Overlay of the experimental and DFT-calculated frequency data of [Au(L2)][PF_6] and [Au(L2)]+. The experimental data has been offset by 0.3 absorbance units.

The overlay of the experimental and calculated IR spectra of [Au(L2)][PF_6] clearly shows a good correlation of the data. The PBE1PBE/LanL2DZ level of theory estimated the vibrational frequencies well. The percentage difference calculated is less than 1.2% which further proves that the estimation of the I.R. spectrum is accurate. The most notable difference between the experimental and DFT-calculated spectra is it ca. 800 cm^{-1}. This corresponds to the hexafluorophosphate(V) anion in the experimental structure, which was not included in the simulations.

The slope of a plot of experimental versus calculated frequencies for [Au(L2)](PF_6) provides a scaling factor which indicates that the experimental frequencies are smaller on average by a factor of 0.998 compared to the calculated data, Figure 6.3.4.

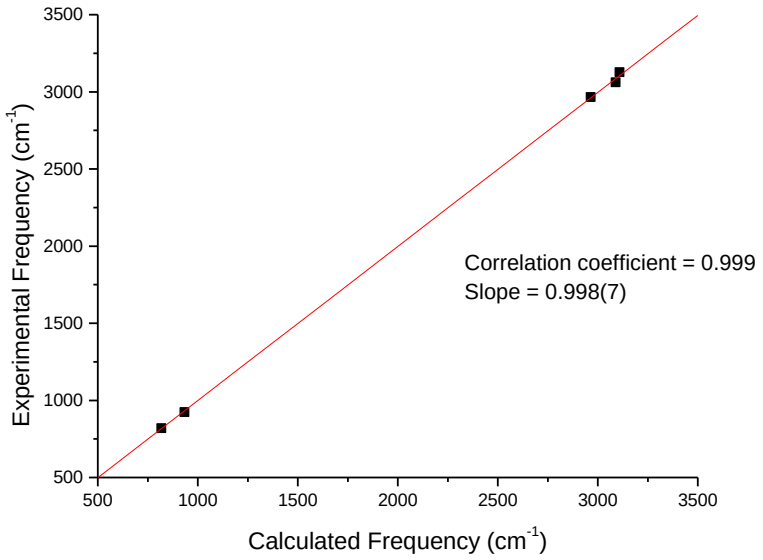

Figure 6.3.4: Plot of vibrational frequencies of [Au(L2)][PF6] versus [Au(L2)]+.

The scaling factor (slope of a plot of experimental versus calculated data) can be directly determined as the plot passes through the origin. The scaling factor shows that on average the experimental frequencies are smaller by a factor 0.998(7) than the calculated frequencies. There is a very good correlation between the experimental and calculated data. Table 6.3.2 is a summary of the data used in the scaling factor plot and shows the percentage difference between the values.

Table 6.3.2: Summary of calculated and experimental frequencies for $[Au(L2)]^+$.

Vibrational mode	**Experimental**	**Calculated**	**Difference (%)***
CH_3	3127	3109	0.58
C-H (imine)	923	934	1.19
C-H ($CH_2CH_2CH_2$)	3061	3089	0.91
C-H ($CH_2CH_2CH_2$)	2966	2965	0.03
C-H imidazole wag	819	818	0.12

*Percentage difference $= \frac{|calc - Exp|}{Exp}\ x\ 100$

NMR spectral Data

The two NMR spectra, i.e. ^{1}H and ^{13}C were calculated using the GIAO method with the PBE1PBE hybrid functional coupled with the LANL2DZ basis set. The solvent model used was dimethyl sulfoxide for the calculation. A CPM solvent model was applied this method places the molecule in a field with a dielelectric constant equal to that of the solvent in question. This method is more computationally economical than implicitly including all solvent molecules surrounding the molecule. As a representative example, the experimental results obtained for complex [Au(L2)](PF_6) will be compared to those simulated for $[Au(L2)]^+$. The remaining chelates show a similar trend. The calculated chemical shifts are in relatively poor agreement and were overestimated in all cases. Figure 6.3.5 shows the structure of $[Au(L2)]^+$ and the atom labelling scheme used in the NMR assignments.

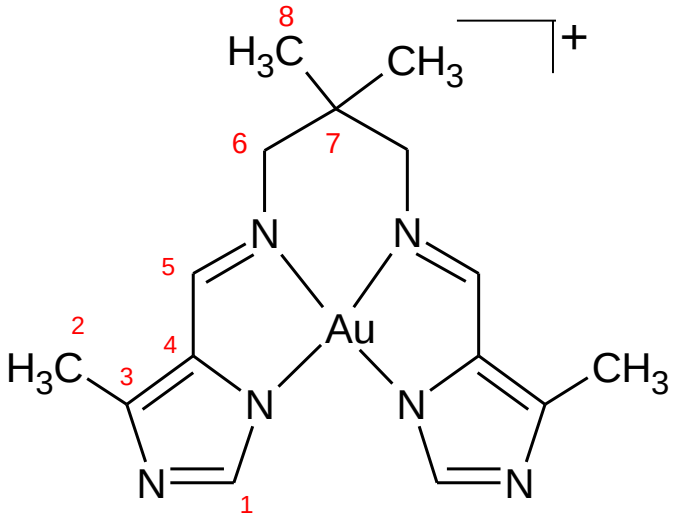

Figure 6.3.5: Structure and atom labelling scheme of $[Au(L2)]^+$.

The comparison between the calculated and experimental chemical shifts is summarised in table 6.3.3.

Table 6.3.3: Summary of the calculated and experimental ^{1}H NMR chemical shifts of $[Au(L2)]^{+}$.

Proton	Calculated (ppm)	Experimental (ppm)	Difference (%)*
2	2.8627	2.53	13.2
6	4.3089	3.47	24.2
1	8.3680	8.46	1.09
5	8.8219	8.81	0.14
8	1.6509	1.08	52.9

*Percentage difference $= \frac{|calc-Exp|}{Exp}\ x\ 100$

Table 6.3.4: Summary of the calculated ad experimental ^{13}C NMR chemical shifts of $[Au(L2)]^{+}$.

Carbon	Calculated (ppm)	Experimental (ppm)	Difference (%)*
2	11.5052	13.93	17.4
8	19.74595	14.68	34.5
6	63.8702	61.62	3.7
4	123.193	153.20	19.6
1	139.948	134.66	3.9
5	146.134	162.98	10.3
3	150.209	147.97	1.5
7	43.4037	23.30	86.3

*Percentage difference $= \frac{|calc-Exp|}{Exp}\ x\ 100$

The calculated and experimental data show a poor correlation. All peaks were overestimated i.e., were estimated to be further downfield than was experimentally observed. The percentage difference is high in most cases. A plot of the experimental and calculated data to try and estimate a scaling factor did not yield a straight line, indicating a random error, which could not be easily accounted for. Interestingly, the simulations were more accurate for aromatic than alkyl protons (percentage errors <2%). This may be because the aromatic protons have fewer degrees of freedom and the static gas phase structure is therefore a more realistic representation of the experimental structure in solution. In contrast, the alkyl groups will be dynamic in solution during NMR data collection and could therefore be more difficult to accurately simulate.

Electronic Transition Results

The electronic transitions for the gold(III) chelates were calculated using the level of theory described above, however, the TD-DFT method was used so as to calculate the excited states involved in electronic transitions. A dimethyl sulfoxide solvent continuum was used in the calculations to account for any solvent effects. As a representative example, the experimental results obtained for complex [Au(L2)](PF_6) will be compared to those simulated for [Au(L2)]$^+$. As shown experimentally, the structure of the di(azomethine) unit does not have a significant impact on the electronic spectra. The same was observed for the simulated data. The results are therefore comparable to that presented for [Au(L2)](PF_6). To avoid repetition the bulk of the data will not be shown, but is available in the Appendix C.

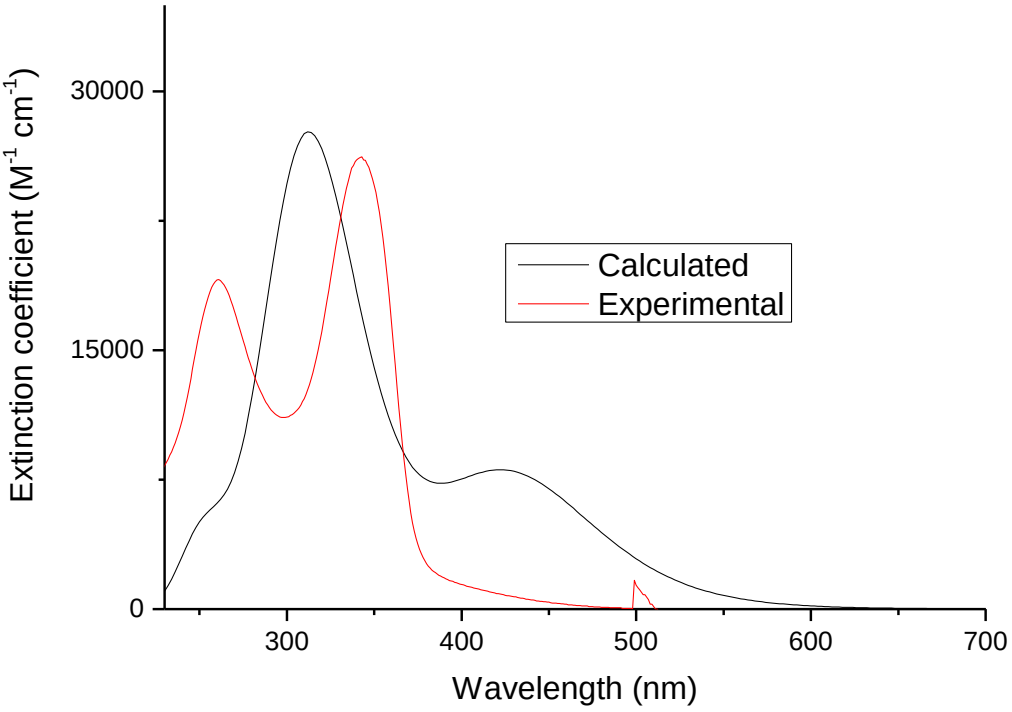

Figure 6.3.6: Superposition of the calculated and experimental UV/visible spectra for [Au(L2)]$^+$. The calculated spectra have been scaled.

Figure 6.3.6 shows a moderate to poor correlation between the two spectra. The extinction coefficient hasn't been correctly calculated. The intensities of the transitions have been underestimated. The calculated spectra also show a blue shift relative to the calculated spectra. The most significant difference in the data lies in the position of the LMCT band. This is

predicted to be a significant band at approximately 430 nm in the DFT-simulated spectrum. In the experimental spectrum it is less intense and significantly blue-shifted.

The orbitals involved in key transitions are shown below in Figure 6.3.6. The remaining UV/visible superposition data can be found in Appendix C.

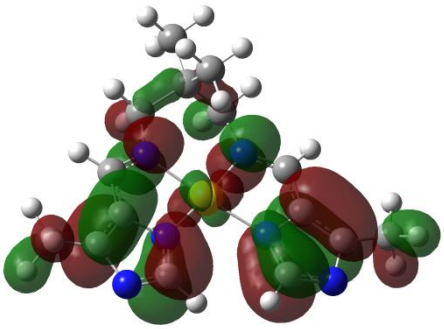

HOMO: 85

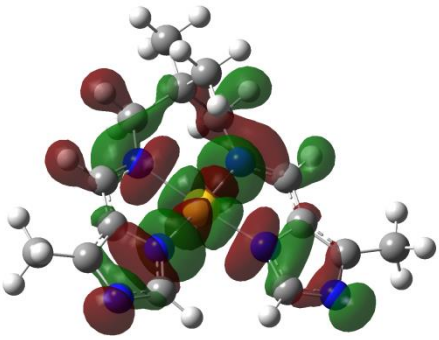

LUMO: 86

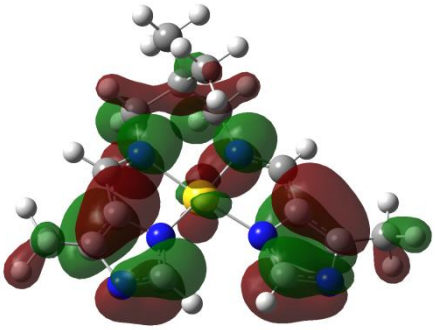

HOMO-1: 84

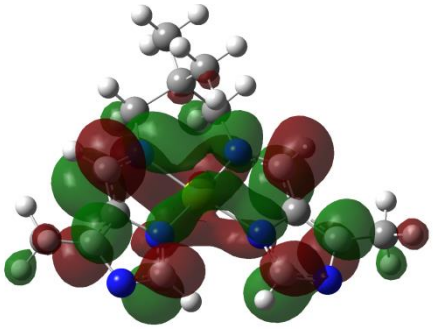

LUMO+1: 87

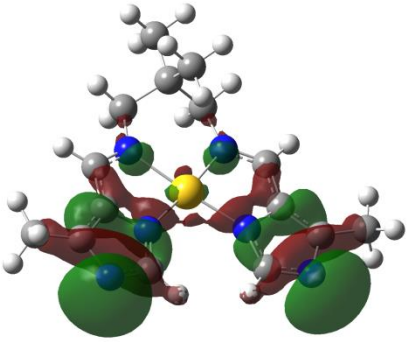

HOMO-2: 83

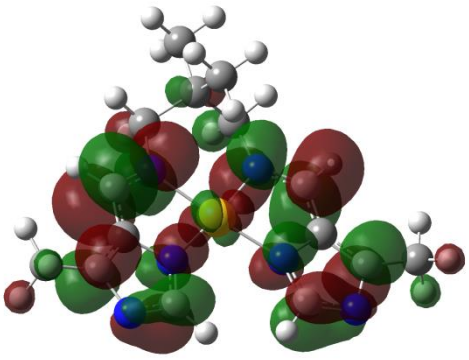

LUMO+2: 88

Figure 6.3.7: The electronic orbitals of $[Au(L2)]^+$ involved in the most significant transitions.

In Figure 6.3.7 it is noted that the HOMO orbital is of π-symmetry with the orbital residing over the imidazole rings and imine bonds. The d_{xy} orbitals of the gold(III) ion is also evident in the HOMO plot. The LUMO is seen to have a σ-symmetry with the dx^2-y^2 orbitals of the gold(III) mixing with the σ orbitals of the ligand. The orbitals involving most transitions are summarized in Table 6.3.1.5 below.

Table 6.3.5: Summary of the DFT calculated electronic transitions for $[Au(L2)]^+$.

Exp. (nm)	**Calculated (nm)**	**Molecular Orbitals**	**Type**	**Oscillator Strength**
261	309	82 → 86; 81 → 87; 84 → 87	π → σ*, π → π*, π → π*	0.2883
	315	78 → 86; 80 → 87; 85 → 87	π → σ*, π → π*, π → π*	0.2059
342	422	83 → 86; 85 → 87	π → σ*, π → π*	0.1322
	453	83 → 86; 85 → 87	π → σ*, π → π*	0.0432

The relatively poor correlation between the experimental and calculated spectra is attributed to the level of theory used in the calculations; PBE1PBE/LanL2DZ. This basis set makes use of effective core potentials and only makes use of valence electrons in the calculations, which may compromise the reliability of the results. In comparison the ligand spectra were estimated significantly more accurately, this is due to the application of the larger 6-311G(dp) basis set. The results for the metal chelate simulations may therefore potentially be improved by the use of a split basis set, applying the LanL2DZ basis set to the metal ion only and the larger, more reliable 6-311G(dp) basis set to the remaining atoms.

6.3.2 Ligands

Geometry Optimisation Results

The geometry-optimised structure was calculated for the ligands using PBE1PBE/6-311G(d,p) level of theory. The DFT-calculated structures were then compared to the experimental X-ray structures for two ligands to determine the accuracy of the selected method. The calculations were conducted *in vacuo*, therefore no intermolecular interactions were considered. A summary of the comparisons of bond lengths and bond angles is shown in Table 6.3.6. Shown in Figure 6.3.8 is the least-squares fit for the DFT-simulated and X-ray structures of H_2L6 and H_2L7. The two structures are almost indistinguishable an RMSD of 0.0791 Å.

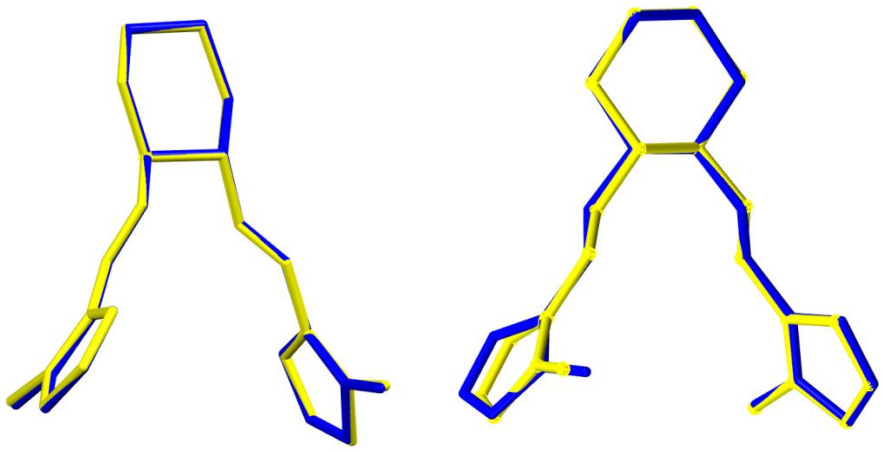

(a) H_2L6(0.0791 Å) (b) H_2L7(0.0791 Å)

Figure 6.3.8: Least-squares fit for the DFT calculated and X-ray structures for (a) H_2L6 and (b) H_2L7. The blue structure represents the X-ray structure and the yellow represents the DFT calculated structure.

Table 6.3.6: Summary of the DFT-calculated and experimental bond lengths, angles and torsion angles of H_2L6 and H_2L7.

Ligand	**Torsion angel* (˚)**		**% diff.**	**C=N-C angel (˚)**		**% diff.e**	**C=N length (Å)**		**% diff.**
	Calc	Exp		Calc	Exp		Calc	Exp	
H_2L6	177.3(5)	179.4	1.2	121.6(4)	120.9	0.6	1.269(6)	1.277	0.6
H_2L7	179.9(3)	179.9	0.0	125.5(3)	123.8	1.4	1.271(4)	1.277	0.5

* Torsion angle between imidazole ring and aromatic moiety

The calculated and experimental data show excellent correlation which suggests that the level of theory used is appropriate and the calculated data is reliable. An interesting point is that although the geometry of the molecules were simulated as monomers in the gas phase, there is still excellent agreement with the experimental geometrical conformation. This suggests that although the solid-state structure is involved in extensive hydrogen bonding, the molecule has had to undergo very minimal deviation from the lowest energy conformation to allow for optimal hydrogen bonding. This would suggest that the solid state structure with its low energy molecular conformation coupled with the stabilising effects of the hydrogen bonding would yield a very stable crystal lattice.

Vibrational Frequency Data

The vibrational frequencies were calculated for comparison with the experimental IR data as well as to confirm the optimised structure was the lowest energy conformation on the global potential energy surface. As a representative example, the experimental results obtained for ligand H_2L6 will be compared to those simulated for H_2L6. The remaining ligands show a similar trend and have been omitted to avoid repetition. The calculated IR plot is compared to the experimental IR plot below in Figure 6.3.9 The slope of the plot, of the calculated versus the experimental IR stretching and bending frequencies Figure 6.3.10, would give a scaling factor and will remove systematic errors in the calculated values.

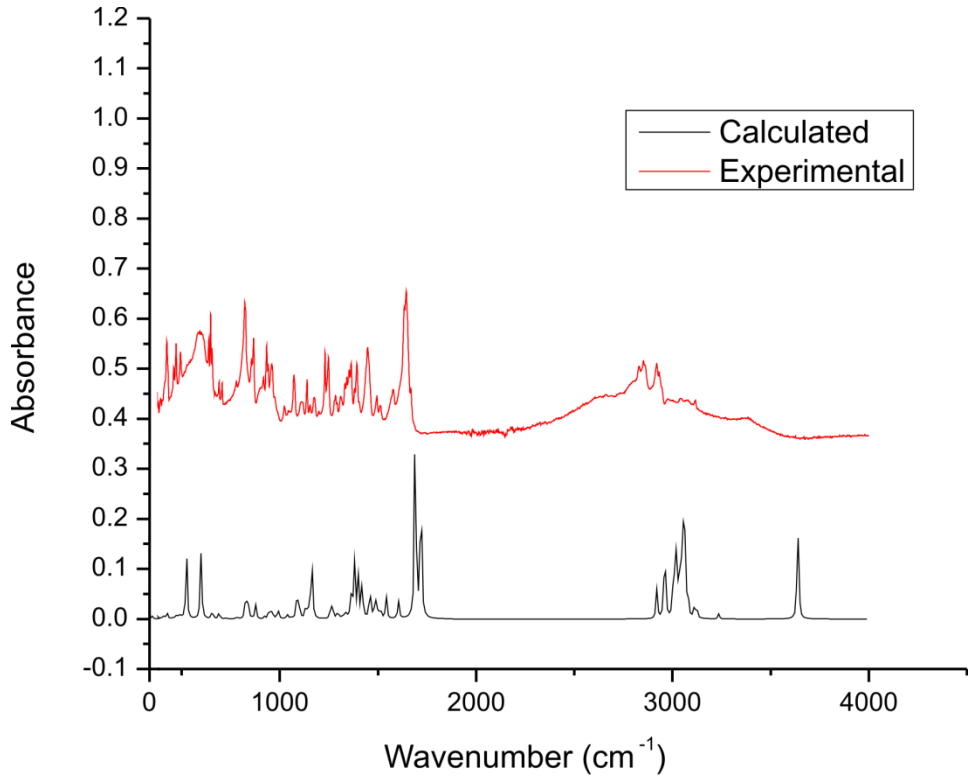

Figure 6.3.9: Overlay of the experimental and calculated IR spectrum of H_2L6.

The overlay of the experimental and calculated IR spectrum of H_2L6 shows a moderate correlation of the two spectra. The B3LYP/6-311G level of theory overestimated the vibrational frequencies to a small extent. This is indicated by the plot of experimental versus calculated frequencies having a slope of less than one (Figure 6.3.10).

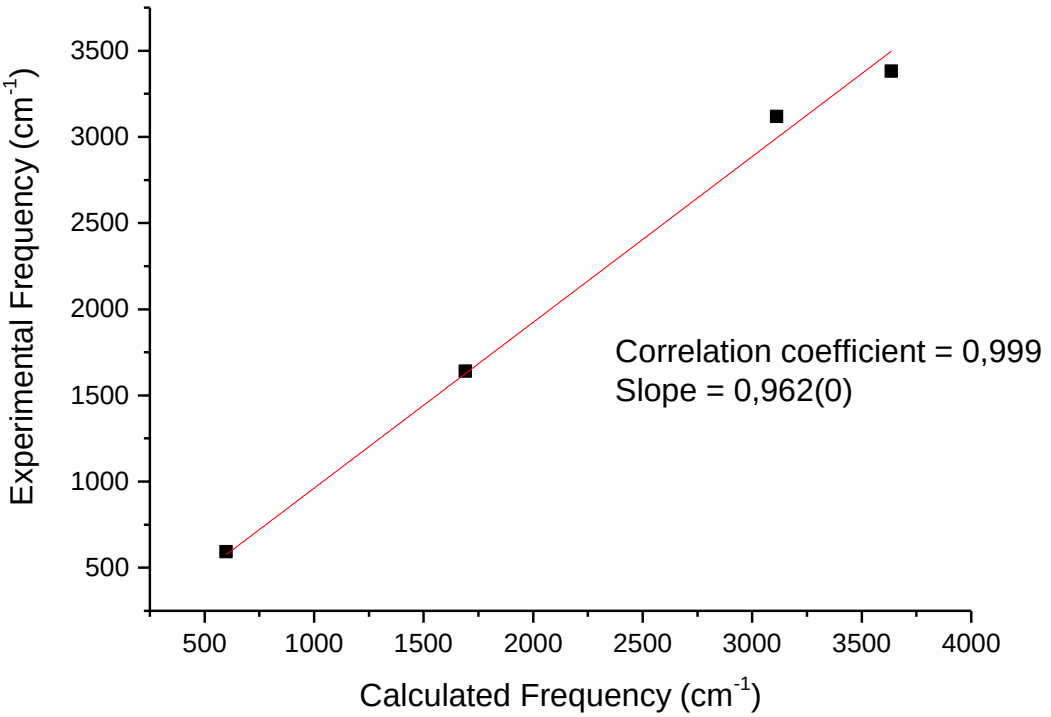

Figure 6.3.10: Plot of calculated versus experimental frequencies for H_2L6.

The plot in Figure 6.3.10 gives a scaling factor which could be applied to the simulated data to increase the accuracy. Notably, the correlation for the free ligand is slightly less convincing than that of the gold(III) chelates. This is unexpected since the former makes use of a larger basis set in the simulations which implicitly includes all electrons in the calculation. The likely reasons for the deviation is that the solid state structure is heavily involved in hydrogen bonding, which can influence the stretching frequency by altering the position of electrons in the molecule and therefore bond order. If these effects were included in the simulations then it is likely that the correlation between experimental and simulated data could be improved.

NMR spectral data

The two NMR spectra, ^{1}H and ^{13}C were calculated using the GIAO method with the B3LYP hybrid density functional and the 6-311G(dp) basis set. The solvent model used was methanol for the NMR simulation. The calculated ^{1}H NMR chemical shifts are in poor agreement with the experimental data in all cases. The comparison between the calculated and experimental chemical shifts is summarised in Table 6.3.7. Table 6.3.8 summarises the equivalent data for the ^{13}C NMR spectra. . Figure 6.3.11 shows the structure of H_2L6 and the atom labelling scheme used in the NMR assignments.

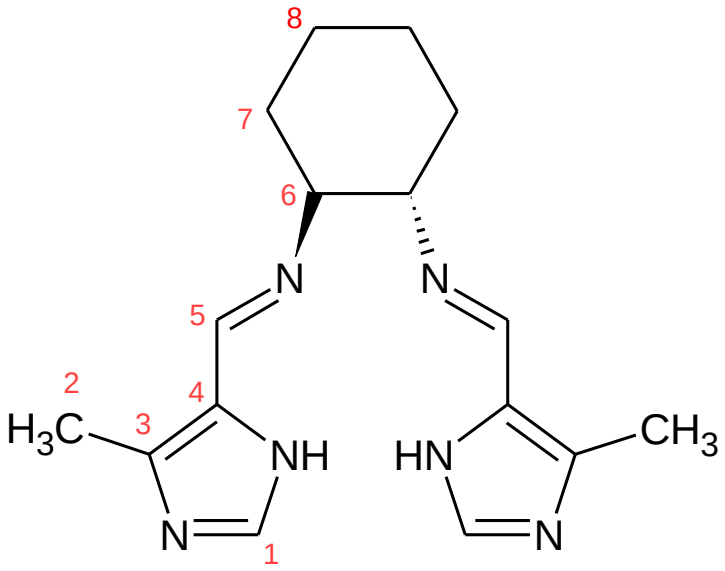

Figure 6.3.11: Structure and atom numbering scheme used for H_2L6.

Table 6.3.7: Summary of the DFT-calculated and experimental chemical shifts of the ^{1}H NMR spectrum for H_2L6.

Proton	**Calculated (ppm)**	**Experimental (ppm)**	**Difference (%)***
2	2.85	2.29	24.5
6	3.86	3.21	20.2
1	8.04	7.44	8.1
5	8.96	8.06	11.2
NH	9.47	12.00	21.1

Table 6.3.8: Summary of the DFT-calculated and experimental chemical shifts for the ^{13}C NMR spectra of H_2L6.

Carbon	Calculated (ppm)	Experimental (ppm)	Difference (%)*
2	10.20	11.88	14.1
7	36.09	33.57	7.5
6	79.35	74.20	6.9
4	133.69	141.62	5.6
1	137.97	125.96	8.7
5	153.52	150.09	2.3
3	142.24	136.67	4.1
8	26.85	24.65	8.9

*Percentage difference $= \frac{|calc-Exp|}{Exp}\ x\ 100$

The calculated and experimental data has a moderate correlation, significantly more satisfactory than that for the ^{1}H NMR data. All peaks were overestimated as was the case with the gold(III) chelates. The percentage difference is relatively high with the highest being 14.1%. No scaling factor could be determined to increase the accuracy for results as the error seemed to be random.

Electronic Transition Results

The superposition of the DFT-calculated and experimental UV/visible spectra for H_2L6 shows an accurate correlation, with only a slight blue shift in the simulated data. The orbitals involving the key transitions are shown below in Figure 6.3.13. The remaining UV/visible superposition data is available in Appendix C.

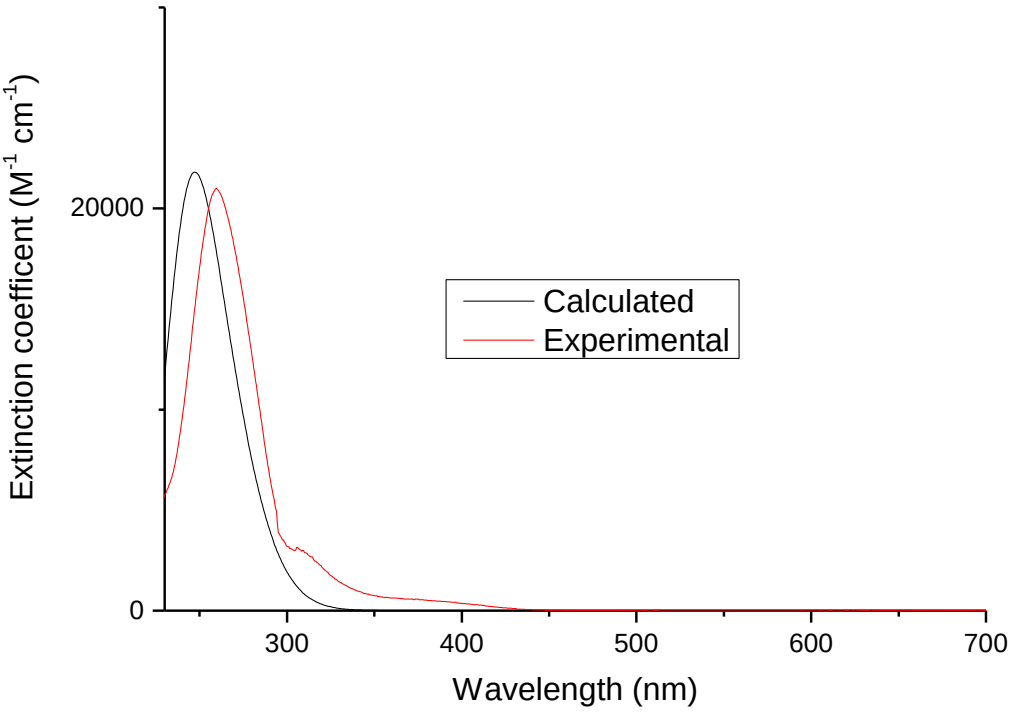

Figure 6.3.12: Superposition of DFT-calculated and experimental UV/visible spectra for H_2L6. The calculated spectra have been scaled.

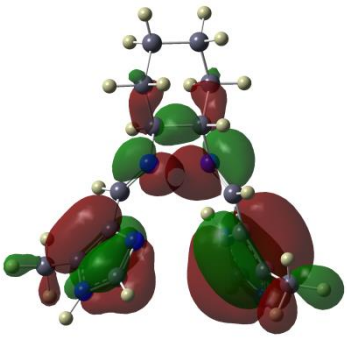

HOMO: 80

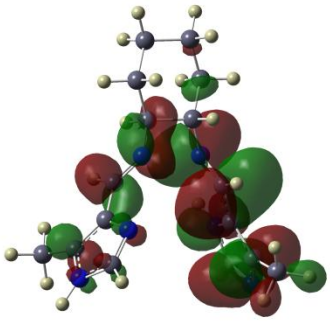

LUMO: 81

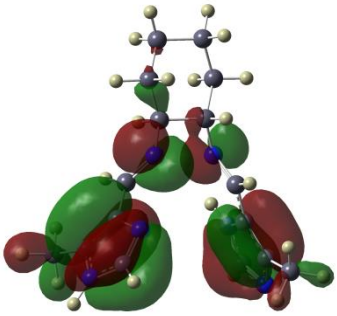

HOMO-1: 79

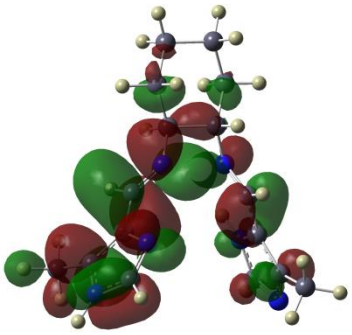

LUMO+1: 82

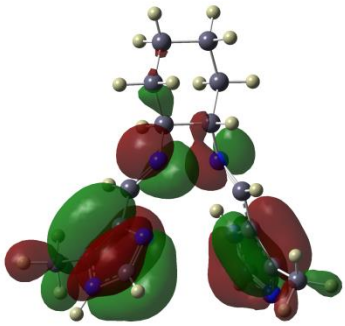

HOMO-2: 78

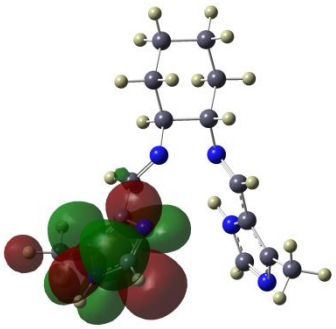

LUMO+2: 83

Figure 6.3.13: Figure 6.3.13 shows that all the molecular orbitals involved in the transitions of H_2L6 were of π-symmetry. The assignment of the primary absorption band as π-π* is therefore appropriate.

Table 6.3.8: Summary of the DFT-calculated electronic transitions for H_2L6.

Exp. (nm)	Calculated (nm)	Molecular Orbitals	Type	Oscillator Strength
260	196	72 → 81; 75 → 81;76→ 82	π → π *, π → π*, π → π*	0..1347
	242	77 → 81; 78 → 81; 78 → 82	π → π *, π → π*, π → π*	0.5616
	254	79 → 81; 79 → 82; 80→81	π → π *, π → π*, π → π*	0.2377

6.4 Conclusion

Density functional theory simulations were performed for the free ligands H_2L6 and H_2L7, as well as the gold(III) chelates. The resulting simulations were compared to the experimental data to determine the accuracy of the simulations and to deconvolute the experimental data.

The least-squares fits of the experimental (X-ray) and DFT-simulated data were in good agreement for both the free ligands and gold(III) chelates. This suggests the the level of theory used for the simulations (B3LYP/6-311G(d,p)) and PBE1PBE/LanL2DZ, respectively) were appropriate.

The vibrational frequency data correlated very well with the experimental data. There was a slight overestimation of vibrational frequencies for the ligands whereas the vibrational data for the chelates were excellent agreement with the experimental data. The difference is attributed to to the extensive hydrogen bonding of the free ligands in the solid state.

^{1}H and ^{13}C NMR calculations were performed for all ligands and chelates. The simulations had poor to moderate results. Some peaks had moderate percentage differences while others were overestimated. No scaling factor could be determined to increase the accuracy of the results. In general, the aromatic protons were estimated more accurately than the alkyl protons.

The electronic transition data for the chelates were relatively poor, particularly for the prediction of the position of the LMCT bans. The electronic transition data for the ligands had a good correlation with a very slight blue shift in the simulated data.

The overall results for the DFT simulations were generally fairly accurate. The ligand calculations were more accurate than the chelate simulations which is expected as the basis set used for ligands (6-311G) is much larger than the basis set used for the gold(III) chelates (LanL2DZ).

6.5 References

1. A. Hinchliffe, *Modeling Molecular Structuers*, 2nd edition (2000), John Wiley and Sons
2. F. Jensen, *Introduction to Computational Chemistry*, John Wiley and Sons New York (1999)
3. D. Young, *Computational Chemistry : A practical guide for applying techniques to real world problems*, Wiley-Interscience, New York (2001)
4. Perdew, J.; Burke, K.; Ernzerhof, M. *Phy. Rev. Lett.* 1996, *77*, 1365-1368.
5. Perdew, J.; Burke, K.; Ernzerhof, M. *Phy. Rev. Lett.* 1997, *78*, 1396-1396.
6. T.H. Dunning Jr., P.J. Hay, in: Modern Theoretical Chemistry, in: H.F. Schaefer III (Ed.), vol. 3, Plenum, New York, 1976, pp. 1–28.
7. Hay, P.Wadt, W. *J. Chem. Phys.,* 1985, *82*, 270-283.
8. Hay, P.Wadt, W. *J. Chem. Phys.,* 1985, *82*, 299-310.
9. Wadt, W.Hay, P. *J. Chem. Phys.,* 1985, *82*, 284.
10. McLean, A.Chandler, G. *J. Chem. Phys.,* 1980, *72*, 5639.
11. Krishnan, R.; Binkley, J.; Seeger, R.; Pople, J. *J. Chem. Phys.,* 1980, *72*, 650.
12. Bauernschmitt, R.Ahlrichs, R. *Chem. Phys. Lett.,* 1996, *256*, 454-464.
13. Casida, M.; Jamorski, C.; Casida, K.; Salahub, D. *J. Chem. Phys.,* 1998, *108*, 4439.
14. Stratmann, R.; Scuseria, G.; Frisch, M. *J. Chem. Phys.,* 1998, *109*, 8218.
15. Van Caillie, C.Amos, R. *Chem. Phys. Lett.,* 1999, *308*, 249-255.
16. Van Caillie, C.Amos, R. *Chem. Phys. Lett.,* 2000, *317*, 159-164.
17. (15) Furche, F.Ahlrichs, R. *J. Chem. Phys.,* 2002, *117*, 7433.
18. Scalmani, G.; Frisch, M.; Mennucci, B.; Tomasi, J.; Cammi, R.; Barone, V. *J. Chem. Phys.,* 2006, *124*, 094107.
19. Akerman, M.Chiazzari, V. *J. Mol. Struct.,* 2014, *1058*, 22-30.
20. Wilson, C.; Fagenson, A.; Ruangpradit, W.; Muller, M.; Munro, O. *Inorg. Chem.,*2013, *52*, 7889-7906.
21. Akerman, K.; Fagenson, A.; Cyril, V.; Taylor, M.; Muller, M.; Akerman, M.; Munro, O. *J. Am. Chem. Soc.* 2014, *136*, 5670-5682.
22. Gaussian 09, Revision D.01, M.J. Frisch, G.W. Trucks, H.B. Schlegel, G.E. Scuseria, M.A. Robb, J.R. Cheeseman, G. Scalmani, V. Barone, B. Mennucci, G.A. Petersson, H. Nakatsuji, M. Caricato, X. Li, H.P. Hratchian, A.F. Izmaylov, J. Bloino, G. Zheng, J.L. Sonnenberg, M. Hada, M. Ehara, K. Toyota, R. Fukuda, J. Hasegawa, M. Ishida, T. Nakajima, Y. Honda, O. Kitao, H. Nakai, T. Vreven, J.A. Montgomery, Jr., J.E. Peralta, F. Ogliaro, M. Bearpark, J.J. Heyd, E. Brothers, K.N. Kudin, V.N. Staroverov, R. Kobayashi, J. Normand, K. Raghavachari, A. Rendell, J.C. Burant, S.S. Iyengar, J. Tomasi, M. Cossi, N. Rega, J.M. Millam, M. Klene, J.E. Knox, J.B. Cross, V. Bakken, C. Adamo, J. Jaramillo, R. Gomperts, R.E. Stratmann, O. Yazyev, A.J. Austin, R. Cammi, C. Pomelli, J.W. Ochterski, R.L. Martin, K. Morokuma, V.G. Zakrzewski, G.A. Voth, P. Salvador, J.J. Dannenberg, S. Dapprich, A.D. Daniels, Ö. Farkas, J.B. Foresman, J.V. Ortiz, J. Cioslowski, D.J. Fox, Gaussian Inc., Wallingford, CT, 2009.
23. GaussView, Version 5, Roy Dennington, Todd Keith and John Millam, Semichem Inc., Shawnee Mission KS, 2009.

Chapter 7| Conclusions and Future Work

7.1 Conclusion

Seven novel bis(imidazole-imine) Schiff base ligands were successfully synthesized. The ligands consist two methyl-imidazole rings joined *via* a di(azomethine) bridging unit. The ligands differed by the structure of the di(azomethine) linkage except for H_2L3 which differs by the absence of a methyl group on the imidazole ring. The ligands were designed to chelate gold(III) *via* strong σ-donor nitrogen atoms. For metal ion chelation, deprotonation of the imidazole NH is required. This yields a tetradentate, dianionic ligand. Chelation of the tetradentate *N*-donor ligands results in cationic gold(III) chelates with a square planar coordination geometry. These were isolated as either the hexafluorophosphate(V) or chloride complex salts. The source of the gold(III) ion was $[Bu_4N][AuCl_4]$ with a two-fold excess of ligand used in the chelation reactions. This metal salt was chosen as it does not hinder the deprotonation of the ligands; as required for chelation. The structures of the five novel gold(III) chelates are shown below in Figure 7.1.1.

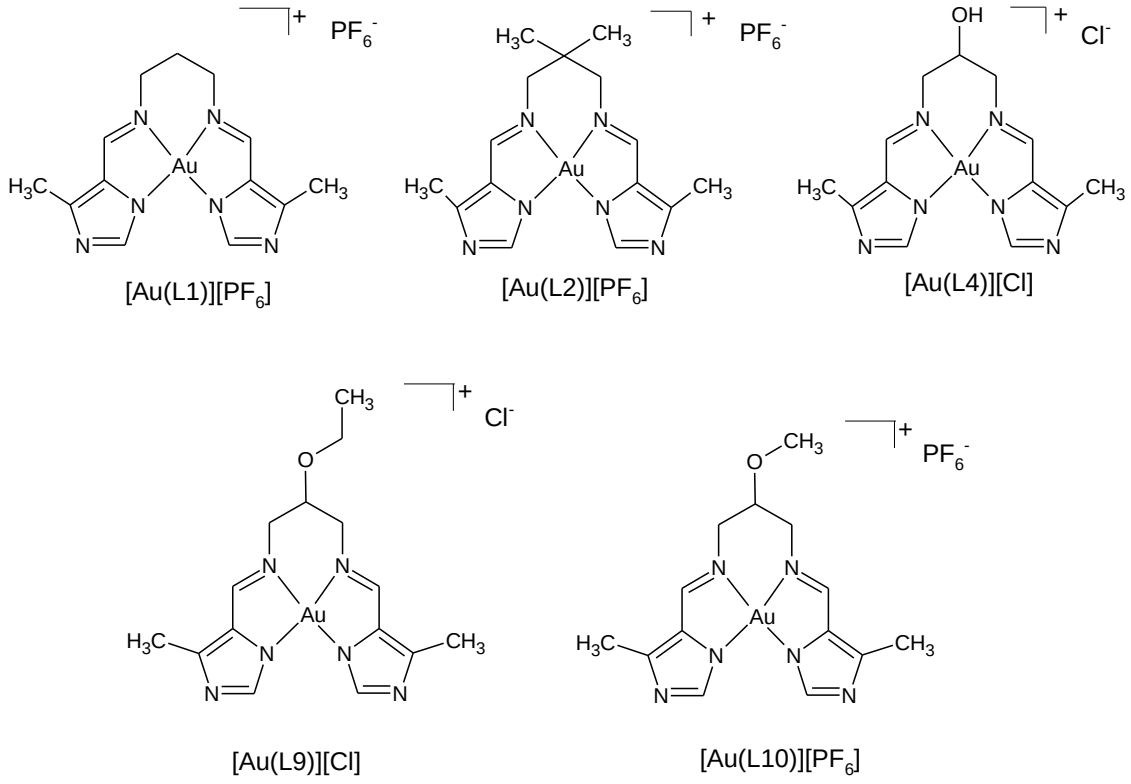

Figure 7.1.1: Structures and abbreviated names of the gold(III) chelates synthesized in this work.

Using various spectroscopic techniques such as NMR (^{1}H, ^{13}C, cosy, hsqc, ^{19}F and ^{31}P), FTIR and UV-visible spectroscopy as well as mass spectrometry, all ligands and metal chelates were fully characterized. Both the ^{1}H, ^{13}C NMR showed a downfield shift of the peaks when comparing the free ligands to the respective chelates. This was due to the deshielding effect of the gold(III) ion and confirmed metal ion chelation. UV-visible spectroscopy showed one band for the free ligand which was π-π* transition and two bands for the gold(III) chelate which were assigned as π-π* transition at higher energy and an LMCT band at longer wavelengths.

X-Ray crystallography was used to determine the solid state structures of two ligands and three gold(III) chelates. The ligands crystallized as the hemihydrate with one water molecule associated with the two interdependent ligand molecules in the asymmetric unit. The ligands were found to form stable hydrogen-bonded networks with the water molecule. The water molecules are found in the centre of hydrogn-bonded columns forming hydrogen bonds with the surrounding ligand molecules. The anti-configuration of the ligands is required for formation of the polymers. The hydrogen -bonded columns are co-linear with the *c*-axis. The three-dimensional structure is a result of a cross-linking the columns through additional hydrogen bonds.

X-ray diffraction data showed the gold(III) chelates all had a square planar coordination geometry. This geometry is ubiquitous for d^8 metal ions with the associated vacant dx^2-y^2 orbitals. The deprotonation of the imidazole NH groups resulted in a dianionic tetradentate *N*-donor ligand. The average N_{imine} bond length measures 2.007 Å and the average $N_{imidazole}$ bond length measures 1.993 Å. The gold(III) chelates, square planar geometry deviated slightly from the ideal square planar geometry with an acute bond angle of 80.73˚ (N_{imine}-Au-$N_{imidazole}$). This bond angle is constrained by the bite angle of the free ligands and associated five-membered chelate ring.

Density Functional Theory (DFT) was used to determine various properties of the ligands and gold(III) chelates. The DFT-calculated data were compared to the experimental data to determine the efficiency of the chosen basis set and hybrid functional applied. DFT was also used to gain a deeper understanding of the experimental data. The level of theory used for ligands was B3LYP/6-311G (d,p) and for the gold(III) chelates PBE1PBE/LanL2DZ. DFT was used to calculate the optimized geometry, NMR and electronic spectra. The vibrational frequencies for both ligands and chelates showed no negative Eigen values which implies that the optimized geometry is indeed the true minimum on the global potential energy surface.

The geometry-optimized structures had a very good correlation with the X-ray structures. The percentage difference in bond lengths for Au-N_{imine} is 3.25% and for Au-$N_{imidazole}$ is 3.71%. The percentage difference in bond angles for $N_{imdazole}$-Au-$N_{imdazole}$, $N_{imdazole}$-Au- N_{imine} and N_{imine}-Au-N_{imine} were 0.02, 0.47 and 1.35%, respectively.

The electronic spectra showed reasonable correlation with experimental data, particularly in the case of the ligands, but the NMR spectra were poorly calculated in some cases. There was in general good correlation between the calculated properties and experimental data, suggesting the level of theory used was appropriate.

The chelates were designed to exploit the square planar nature of the gold(III) ion to produce metal aromatic metal chelates suitable for DNA intercalation to control the proliferation of tumour cells. Both direct DNA binding titrations and competitive DNA binding studies did not show any significant affinity towards DNA. The likely reason for this is that the methyl groups on the imidazole rings, which are required to stabilise the metal ion through their inductive effect, prevent the intercalation process. This class of compounds therefore needs further development to achieve the final goal of chemotherapeutic agent. The future avenues of research are described below.

7.2 Future Work

The main aim of this study was to synthesize and fully characterize a range of seven novel imidazole-imine Schiff base ligands and their respective gold(III) chelates. The gold(III) chelates have been designed to intercalate DNA and the next step is to determine the chemotherapeutic properties of the chelates. The chelates could interact with DNA in one of two ways: intercalation or groove binding. These binding modes have been explained in Chapters 1 and 5.

DNA titrations and competitive DNA binding assays have been done on the synthesised complexes, but the results show limited intercalation. This is likely due to the bulky methyl groups found on the imidazole ring which cause steric hinderence when attempting to intercalate
between the aromatic DNA base pairs. The methyl groups cannot be removed entirely as their inductive effect is needed to stabilise the gold(III) ion. An alternative solution is to move the position of the methyl groups next to the imine bond (refer to Figure 4.4.3).

By using 1-(1*H*-imidazol-5-yl)ethanone instead of 4-methyl-1*H*-imidazole-5-carbaldehyde, it will create a larger planar aromatic region for intercalation while still retaining the inductive effect of the methyl groups needed to stabilse the gold(III) ion. This is an exciting new prospect which could maintain stability, while increasing the potential for DNA intercalation.

Although the chelates were not shown to be intercalators the second binding option is groove binding. Molecules that bind in either the major or minor groove of DNA do not necessarily need to be planar. It is therefore possible that the current gold(III) chelates could act as groove binding agents and could still be therapeutics. This avenue needs to be further explored. To determine DNA groove binding, the method of choice employs emission spectroscopy. Nucleic acid dyes such as 40,6-diamidino-2-phenylindole (DAPI) are used to bind to DNA base pairs, which leads to an increase in fluorescence emissions. A second DNA groove binder (complex) is now introduced which ideally has a higher binding affinity than DAPI. The second groove binder displaces DAPI which leads to a decrease in emission. Since DAPI is a known groove binder, the decrease in emission would indicate that the complex has associated with the DNA *via* groove binding [1].

Another important objective for future work is tumour cell screening. This will determine the cytotoxicity of the chelates towards human tumor cell lines. Since there are many types of cancers, each chelate will likely have varying cytotoxicity towards each cell line. The variation of the bridging unit allows for the physico-chemical properties of the chelates to be tuned. This is an important aspect in the development of chemotherpeutics as it has been shown that small structural changes can have a marked effect on the lipophilicity of a compound. This can influence the efficiency with which a drug can cross the phospholipid bilayer of the cell wall and reach its cellular target. This will impact cytotoxicity. To this end, measuring the lipophilicity of the chelates by determining the octanol/water partition coefficient can give insight into potential cytotoxicity. It has also been shown that lipophilicity can influence DNA binding as the chelates must be stable in the hydrophobic core of the DNA helix [4], tuning this aspect could therefore improve the DNA binding affinity.

One of the most important aspects in developing new chemotherapeutics is to increase the uptake of the compounds in neoplastic versus healthy tissue. This would likely reduce the side effects associated with current chemotherapies. This could be achieved by variations of the bridging unit to include biotin. Biotin is also known as vitamin H and is an important nutrient for living organisms due to its role as a cofactor for enzymes involved in carboxylation and decarboxylation [2]. There are many biotin receptors found in cancer tissues, therefore by

attaching biotin, the gold(III) chelate could show enhanced uptake in neoplastic tissue. The proposed structure of the chelate with biotin attached is illustrated below in Figure 7.2.2.

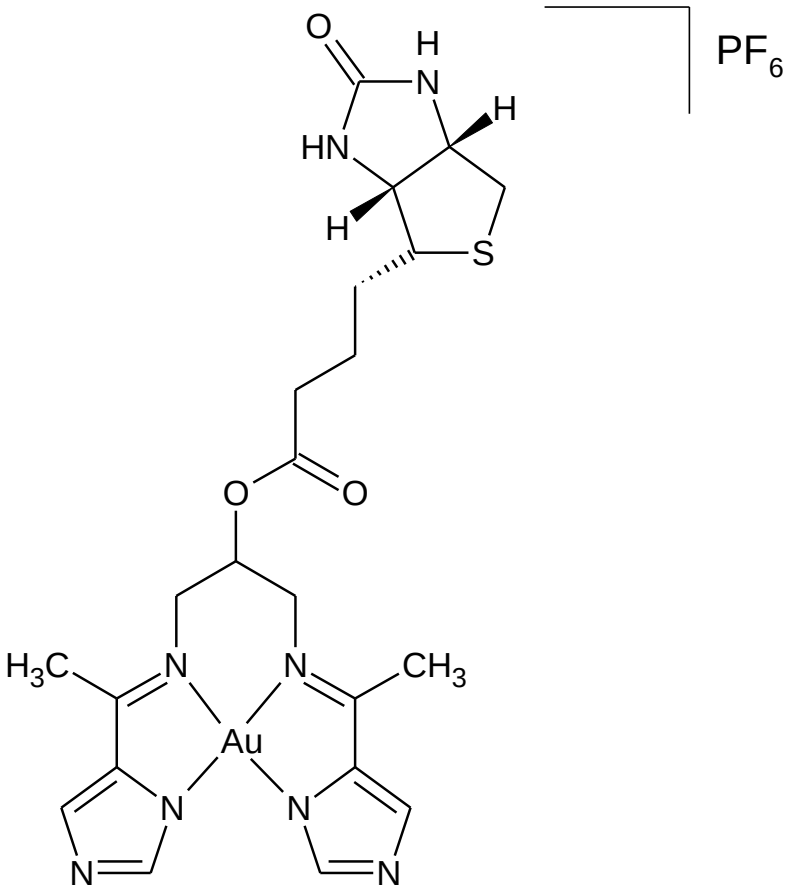

Figure 7.2.2: Proposed structure of the chelate with biotin attached.

If the aspects proposed above for future research are successful then an important parameter to determine for any new drug is biodistribution. This is an experimental method of tracking the movements of a compound in an organism. One of the best methods for doing this is using a radioactive tracer. In this case ^{198}Au will be synthesized and chelated to the most promising ligand. The chelate will then be administrated to rats. After selected periods of time the rats will be terminated using an isoflurane overdose. Vital organs, selected limbs and blood can then be counted for radiation to measure the uptake of the compound in specific organs. This method can also give an indication of the stability of the chelate *in vivo* as metal-based drugs are known to bind to serum proteins leading to large metal-serum protein adducts which are not easily excreted and may be toxic. The ^{198}Au ion has several desirable characteristics which make it suitable for such biodistribution studies. The ^{198}Au isotope with $t_{½}$ = 2.7 days, E_{β} = 0.97 MeV and E_{γ} = 411 keV was chosen for chelation by the Schiff base ligand as the high-energy γ photons are suitable for external detection by the single-photon imaging instrumentation used in nuclear medicine departments [3].

7.3 References

1. Williams, A.; Dasilva, S.; Bhatta, A.; Rawal, B.; Liu, M.; Korobkova, E. *Anal. Biochem.*, **2012**, 422, 66-73.
2. A. Leon-Del-Rio, J. *Nutrit. Biochem*., **2005**, 16,432.
3. Akerman, M.; Munro, O.; Mongane, M.; van Staden, J.; Rae, W.; Bester, C.; Marjanovic-Painter, B.; Szucs, Z.; Zeevaart, J. *J. Label Compd. Radiopharm*., **2013**, 56, 530-535.
4. Akerman, K.; Fagenson, A.; Cyril, V.; Taylor, M.; Muller, M.; Akerman, M.; Munro, O. *J. Am. Chem. Soc.* 2014, *136*, 5670-5682.